

THÈSE de DOCTORAT

Opérée au sein de :

Sorbonne Université

Ecole Doctorale ED391

Sciences mécaniques, acoustique, électronique et robotique de Paris

Spécialité de doctorat : Mécanique des fluides

Soutenue publiquement le 29/11/2024, par :

Artur Gesla

**Numerical investigation of the dynamics of an
axisymmetric rotor-stator flow**

Devant le jury composé de :

Marc Avila Canyellas

Full professor, Universität Bremen

Rapporteur

Denis Sipp

Directeur de recherche, Office national d'études et de recherches aérospatiales

Rapporteur

Ivan Delbende

Maître de conférences, Institut Jean le Rond d'Alembert, Sorbonne Université

Examinateur

Laurette Tuckerman

Directrice de recherche émérite, PMMH-CNRS, Sorbonne Université

Examinateuse

Laurent Martin Witkowski

Professeur des universités, Université Claude Bernard Lyon 1

Directeur de thèse

Yohann Duguet

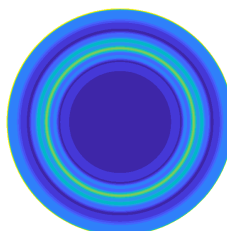
Chargé de recherche, LISN-CNRS, Université Paris-Saclay

Co-Directeur de thèse

Patrick Le Quéré

Directeur de recherche émérite, LISN-CNRS, Université Paris-Saclay

Co-Encadrant de thèse



Picture at the bottom
of the front page:
Isocontour of the azimuthal velocity
of the optimal response at $Re = 225$.

Acknowledgements

This thesis would never take the present shape without all the support and kindness that I received during my three years stay in LISN laboratory.

Firstly, I would like to thank my supervisors: Laurent Martin Witkowski, Yohann Duguet and Patrick Le Quéré. I value very highly all the time we have spent on discussions and ideas' exchanges. I would also like to thank Marc Avila and Denis Sipp for accepting to be the reporters of the work. I also thank Laurette Tuckerman and Ivan Delbende for accepting to be in my doctoral committee and accompanying me in my doctoral journey through the comité de suivi individuel de thèse. Secondly, I would like to thank Diana-Georgiana Baltean-Carles, Catherine Weisman, Anca Belme, Fatiha Bouchelaghem and Cédric Croizet for the opportunity of teaching activity at the Sorbonne University. I really enjoyed working with students and look forward to continue the teaching responsibilities in the future. I also want to thank Anne Sergent and Nicolas Grenier for the organisation of *Journées Écoulements & Fluides - Saclay*, where I had the pleasure to present my work multiple times.

I would like to thank all of the other doctoral candidates and interns present in the lab. I thank in particular the ones that shared the office with me: Antoine Faugaret, Sabrina Bénard, Gen Wu and Nathan Carbonneau. Your support and positive attitude made my doctoral studies a memorable and enjoyable journey. Lastly, I thank all of my family and friends. Whether you stay in Poland, in Germany or in France I could not have completed this thesis without your support.

Preface

In this thesis the axisymmetric rotor-stator flow is studied. Despite the apparent simplicity of the axisymmetric setup, the flow exhibits a rich variety of phenomena. The main motivation for this work is the experimental observation of circular axisymmetric rolls. This work aims at providing the scenario in which the rolls are the result of the external forcing of the flow. Apart from that, the thesis treats the questions of the linear stability of the flow and the existence of finite amplitude self-sustained solutions. Many numerical methods used to track the self-sustained solutions and find the optimally forced structures, are also described in this manuscript. Especially, a new method of the determination of a periodic orbit and studying its stability based on a expression in Chebyshev polynomials is proposed.

The results of this work are under review (Gesla et al., 2023, 2024a,b). The content of the thesis is that of the papers enhanced with more elaborate discussions and additional figures. In particular the spatial discretisation and the time integration scheme are detailed. The functionalities of the code developed during the thesis are also listed. The manuscript closes with a summary presenting the results and outlooks for further studies.

Contents

Acknowledgements	3
Preface	5
1 Introduction	9
2 Governing equations and numerical methods	15
2.1 Flow configuration	15
2.2 Governing equations	16
2.3 Spatial discretisation	16
2.3.1 Mesh resolution	17
2.4 Determination of the steady state solution using the Newton method	18
2.4.1 Linear stability analysis of the steady state solution	19
2.5 Temporal integration of the governing equations	20
2.5.1 Prediction step	20
2.5.2 Projection step	21
2.6 Codes developed in the scope of the project	21
3 Base state and its stability	23
3.1 Base flow	23
3.2 Comparison against the self-similar profile	23
3.3 Linear stability analysis	26
3.4 Threshold sensitivity to the numerical resolution	26
3.5 Non-normality of the linearised dynamics	27
4 Subcritical axisymmetric solutions	31
4.1 Periodic solutions	31
4.1.1 Self-Consistent Method (SCM)	32
4.1.2 Harmonic Balance Method (HBM)	32
4.1.3 Hopf branch	33
4.1.4 Periodic-subcritical branch	35
4.2 Edge states	37
4.2.1 Notion of edge state	37
4.2.2 Bisection algorithm	38
4.2.3 Edge branch	38
4.2.4 Frequency analysis	39
4.2.5 Quasiperiodicity of the edge state	41
4.2.6 Connection between the edge state and the chaotic rolls	44
4.2.7 Saddle-node bifurcation and mesh dependence	44
5 Noise sustained states and the response to the forcing	47
5.1 Linear response to forcing	47
5.1.1 Optimal response : theory	47
5.1.2 Optimal response : results	48
5.1.3 Boundary forcing	52

5.1.4	Computation of the pseudospectrum	54
5.2	Experimental comparison	55
5.3	Nonlinear receptivity	57
5.3.1	Effect of the nonlinearity	59
5.3.2	Leaky chaotic attractors and finite lifetime dynamics	61
6	Stability analysis using Chebyshev polynomial expansion	65
6.1	Introduction	65
6.2	Description of a periodic orbit	66
6.2.1	General concepts	66
6.2.2	Finite differences	67
6.2.3	Harmonic balance method	69
6.2.4	Chebyshev polynomial expansion	69
6.3	Examples	71
6.3.1	Lorenz system	72
6.3.2	Langford system	74
6.4	Differentially Heated Cavity	76
6.4.1	Governing equations and numerical methods	77
6.4.2	Stability of the supercritical Hopf branch	77
6.5	Summary	78
7	Summary	81

Chapter 1

Introduction

Flows in closed cylindrical containers rotating around the cylinder axis have motivated many hydrodynamic stability studies due their simplicity, their relevance to various industrial configurations and the dramatic patterns observed (Moisy et al., 2003; Launder et al., 2010). The flow is characterised by two independent parameters : a Reynolds number $Re = \Omega H^2 / \nu$ and a geometrical aspect ratio $\Gamma = R/H$ where H and R are the respective height and radius of the cylinder, Ω is the rotor's angular velocity and ν is the kinematic viscosity of the fluid. Depending on the aspect ratio Γ various flow structures can be observed. These are shown in figure 1.1 and 1.2. Tall cavities ($\Gamma < 1$) were historically studied because of the fundamental interest in vortex breakdown. Thin cavities ($\Gamma > 5$) on the other hand were historically studied because the geometry resembles the geometry between the discs inside a turbine.

The base flow for the configuration of interest here, where $\Gamma \geq 5$ (thin cavities), is axisymmetric. It has a dominantly azimuthal flow with strong shear at the walls, as well as a meridional recirculation, associated, for high enough Re , with two separated boundary layers, one along the stator (labelled Bödewadt boundary layer) and the other along the rotor (labelled Ekman boundary layer).

Early investigations of the laminar flow regime in the flow between two infinite discs, one of which rotating, questioned the structure of the laminar velocity field. Many co-existing steady solutions with a self-similar spatial structure were reported (Holodniok et al., 1977; Zandbergen and Dijkstra, 1987), among them the well-known solutions by Batchelor (1951) and Stewartson (1953). In the presence of a radial shroud, the system is thought to admit only one steady solution existing for all rotation rates, which will be considered as the *base flow*. It features a closed meridional recirculation of the Batchelor type including a boundary layer on the stator and another one on the rotor. This base flow solution departs increasingly from the self-similar solutions as the distance from the axis and the rotation rate increase (Brady and Durlofsky, 1987).

This work address the mechanisms through which rotor-stator flows transition towards unsteady regimes interpreted as precursors of turbulent flow. Global linear stability analysis of the base flow (Gelfgat, 2015) predicts, for large enough aspect ratios, the linear instability of non-axisymmetric spiral modes, usually in quantitative agreement with concurrent experimental observations (Gauthier, 1998; Schouveiler et al., 2001) and later numerical simulations (Serre et al., 2001, 2004). The azimuthal wavenumber m of these spirals is typically large and comparable to the radius-over-gap ratio Γ . The spiral modes and their onset were reported as experimentally robust, independent of the noise level (Gauthier, 1998). The nonlinear saturation of these spiral modes follows a simple supercritical scenario followed by turbulent transition (Launder et al., 2010).

The spiral arms are however not the coherent structures appearing at the lowest rotation rates. Concentric rolls of finite-amplitude have been frequently reported as the earliest manifestation of unsteadiness in moderate-to-large aspect ratios. This phenomenon was first reported in spin-down experiments (Savas, 1983) and then in most experimental studies (Gauthier et al., 1999; Schouveiler et al., 2001), but have been overlooked by most computational stability analyses. An overview of

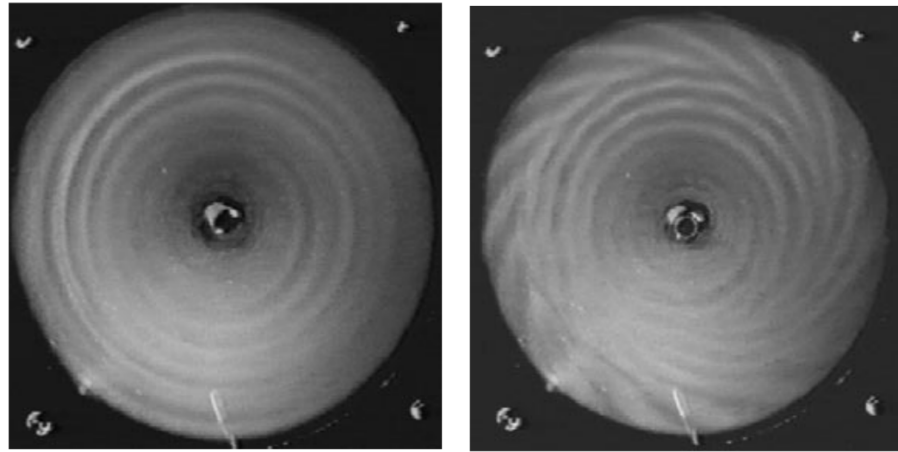


Figure 1.1: Top view of a thin cavity $\Gamma = 8.75$ (Schouveiler et al., 2001). Left: circular rolls $Re_H = 224$. Right: circular rolls superimposed with spirals $Re_H = 273$. Bottom disc is rotating clockwise.

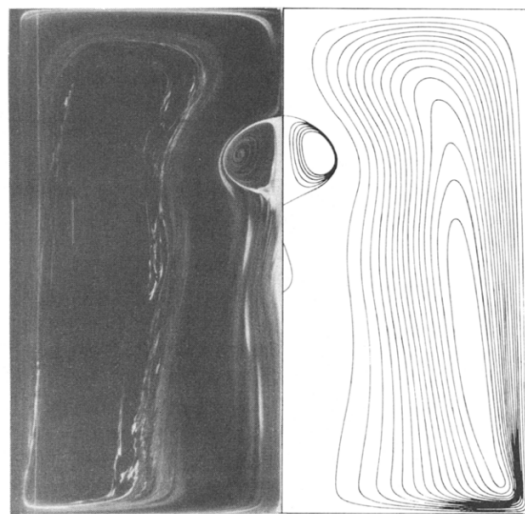


Figure 1.2: Side view of a tall $\Gamma = 0.5$ cavity for $Re_H = 463$. Observed flow pattern (left) compared with computed streamlines (right) (Escudier, 1988).

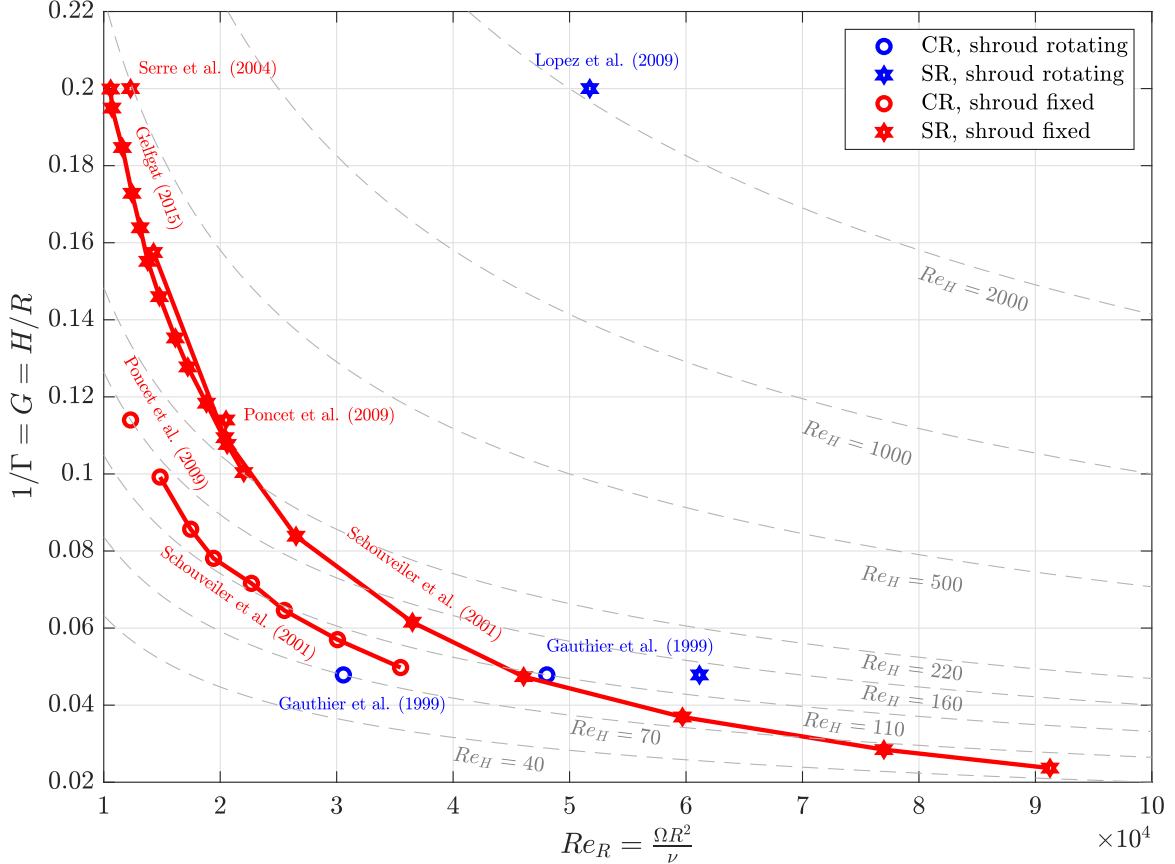


Figure 1.3: Literature review concerning the Re at which either circular rolls (CR) or spiral rolls (SR) could be observed. Lines of constant Re_H are traced for convenience.

the critical Re at which either the circular or spiral rolls were observed is presented in figure 1.3. $Re_R = \Omega R^2 / \nu$ based on the radius and $Re_H = Re$ based on the interdisc spacing are marked for easy comparison of the results. Both experimental numerical results are presented in a single graph. System configurations with rotating or fixed shroud are marked in blue and red respectively. The critical Re corresponding to the circular rolls and spiral rolls is marked with a circle and a star symbol respectively. It is noted that the critical Re corresponding to the circular rolls is quite consistent $Re_H \approx 70 - 160$ irrespectively of the study.

Viewed in a meridional plane the circular rolls correspond to wavepackets of vortices located near the stator (Gauthier et al., 1999). At low enough Re close to their experimental onset they are simply convected inwards and disappear as they pass near the axis before they reach the rotor Gauthier et al. (1999). At higher Re the rolls described in Schouveiler et al. (2001) form a steady front with complex internal dynamics. Adopting a local-like description, these rings are usually described as emerging from a convective instability of the Bödewadt layer, developing from the corner, and propagating inwards along the stator until the axis region where they are damped (Poncet et al., 2009). The presence of these additional flow structures can potentially undermine all predictions from linear stability analysis. The concentric rolls were reproduced in direct numerical simulations but were reported as short transients rather than sustained coherent structures (Lopez et al., 2009). As shown by Daube and Le Quéré (2002) in a strictly axisymmetric context, the base flow is linearly unstable to the axisymmetric mode for much higher Reynolds number Re than suggested from experimental observation. Such an observation is consistent with the outcomes of previous linear stability studies that spirals as the first mode of linear instability. Chaotic subcritical solutions were actually identified by Daube and Le Quéré (2002). Their study describes: i) a linear instability respecting the axisymmetry of the flow was identified using eigenvalue, at a value of Re

above that where rings can be observed, ii) quantitatively huge levels of transient growth before iii) the ring patterns saturate in amplitude, iv) the existence of a subcritical large amplitude chaotic solution branch. These new features, especially i) and ii) are familiar to the subcritical shear flow community working on plane Poiseuille and boundary layer flows (Manneville, 2016; Eckhardt, 2018).

Several questions can be asked at this point : is the critical point of Daube and Le Quéré confirmed and how robust is it? Does a branch of axisymmetric nonlinear states bifurcate subcritically from this point? Is it physically consistent with the convective instability put forward by experimentalists? The lack of radial propagation of the associated envelope, attested from experimental space-time diagram, suggests that nonlinearity can enter the picture. Adopting such a point of view, the quasi-steady envelopes of rings could be interpreted as genuinely nonlinear states, with a complex time dependency but a coherent spatial structure. This should be contrasted with the concept of noise-sustained coherent structure (Tobias et al., 1998; Poncet et al., 2009). The subcriticality of the ring regime and the presence of an axisymmetric instability threshold, both reported by Daube and Le Quéré (2002), would make the nonlinear branch emerging from the critical point, if it is confirmed to also bifurcate subcritically, the ideal candidate to explain experimental observations. Subcriticality would also imply that, for $Re < Re_c$, only finite-amplitude perturbations above a certain threshold can excite this non-trivial regime.

In order to shed a light on the interrogations above, chapters 3 and 4 aim at better characterising the stability threshold and its numerical robustness, at identifying for the first time nonlinear branches of solutions possibly connected to the critical point, and at debating whether the corresponding nonlinear states bear any relation with the patterns observed experimentally and numerically. Among all possible nonlinear states that can exist beyond the laminar base flow, many nonlinear solutions of the subcritical regime are unstable. Some of them possess the property of lying on the laminar-turbulent boundary, the so-called *edge* manifold in the associated state space. Numerical simulations constrained to lie in that manifold converge asymptotically to specific equilibrium regimes called *edge states*. Their determination is specifically interesting for subcritical transition since their instability captures the mechanisms leading from finite-amplitude initial perturbations of the base flow towards the turbulent state. Many traditional numerical algorithms turn out to be technically too limited for the search of nonlinear states. This represents an opportunity to improve them or to use recent methods whose relevance will be also discussed. The resulting observation is that the continuation of the branch of self-sustained states towards lower Re fails to reach the low values relevant for circular rolls in experiments.

A hint pointing at the origin of the circular rolls comes from the experimental study of Gauthier et al. (1999). They observed that a change of motor in their experimental set-up lowers the threshold of appearance of rolls by roughly half. This pointed in turn to a high sensitivity of the rolls to external disturbances. Following these observations, numerical computations were performed where the system was continuously forced with a sinusoidal libration of the rotor (Lopez et al., 2009; Do et al., 2010). This forcing also proved to sustain a roll-like response although the exact temporal dynamics would remain to be compared to its experimental counterpart. In particular, Do et al. (2010) demonstrated that nonlinear effects contributed to the global dynamics of the rolls. It is shown in chapter 4, at least for the case $\Gamma = 10$, that the axisymmetric system features, independently of any external forcing, a self-sustained nonlinear regime coexisting with the base flow below the critical threshold. The existence of this subcritical regime is reminiscent of other subcritical shear flows such as Poiseuille flows and plane Couette flow (Eckhardt, 2018; Avila et al., 2023). This leads to the dilemma whether the circular rolls observed in experiments should be interpreted as a response to external forcing, in other words a noise-sustained state, or as the footprint of a self-sustained coherent state of nonlinear origin. Even in the case where the flow is externally forced, is the response linear or are nonlinear interactions important? Does the flow follow a resonance scenario or does it display its own preferred response at a given frequency, and if yes through which selection mechanism?

The chapter 5 aims at answering these questions by means of resolvent analysis and numerical simulations. Although the circular rolls were reported experimentally only at low values of Re where the flow stays axisymmetric, we propose to consider Re as the main governing parameter for

the purely axisymmetric rotor-stator configuration, regardless of whether the experimental dynamics would stay axisymmetric or not, and to investigate the effect of varying Re on both the linear receptivity scenario and the fully nonlinear one. Our receptivity approach to external forcing follows several complementary approaches. Classical optimal linear response theory, through resolvent analysis, directly yields the optimal forcing eliciting the strongest response of the flow. By design however, this forcing is applied within the bulk of the flow, away from the solid walls. Parasite vibrations of the set-up are rather expected to act at the fluid-solid interface and, thus, bulk-based optimisation might not capture them especially when the forcing is modelled as an additive force. For this reason, as well as for the freedom of incorporating nonlinear fluid interactions, direct numerical simulation of fluid flow in the presence of well controlled boundary oscillations is also considered without any optimisation. As we shall see, the scenario most consistent with experimental observations is the boundary forcing. For higher Re , we demonstrate numerically how circular rolls of finite amplitude can be elicited and sustained by nonlinear forcing, whereas depending on the value of Re they correspond either to super-transients or to an attracting dynamics, should the forcing be turned off. Beyond the immediate analogy with subcritical shear flows, it is also of strong general interest as it generalises the phenomenon of linear receptivity to the nonlinear framework.

The last chapter forms a stand alone part, separate from but related to the main topic of the thesis. It presents a method of describing the periodic orbit of a dynamical system using either Fourier or Chebyshev temporal basis functions. To keep the introduction focused on the rotor-stator cavity flow, the literature review concerning the periodic orbits' description is moved to the beginning of the chapter 6. For the sake of completeness, it is only mentioned here that the chapter 6 presents a method to extract the stability of the periodic orbit stable or unstable to either simple or complex Floquet multipliers. The presented examples include the Lorenz system, the Langford system as an example of a Neimark-Sacker bifurcation and the two dimensional square differentially heated cavity flow as an example of application of the proposed method to a system of large number of degrees of freedom.

The rest of the manuscript is organised as follows. Chapter 2 introduces the numerical methods for finding the base flow solution of the governing equations in a two dimensional setting and time integration of the governing equations. Chapter 3 describes the base flow in a rotor-stator cavity and documents its linear stability analysis. Chapter 4 documents the self-sustained solutions found in the flow and the methodology to determine them. In particular, the biperiodic edge state is described. Chapter 5 presents the results of the response of the flow to forcing and characterises the optimal response of the flow. Chapter 6 describes in detail an approach to compute a periodic dynamics of a system using Fourier or Chebyshev basis functions. It also presents the stability of solutions found using the respective bases. Finally, chapter 7 summarises the work and gives an outlook to future investigations.

Chapter 2

Governing equations and numerical methods

In this chapter the flow set-up and the governing Navier-Stokes equations in a cylindrical coordinate system will be introduced. Staggered grid arrangement is explained in detail. The two main numerical tools are then described: the Newton method and its application to find the laminar steady state solution of the governing equations and the time integration procedures. Since those two methods are used throughout the thesis they are introduced here, in the introductory chapter. Many more algorithms and modifications of the standard methods were used in the study but those will be described in the subsequent chapters as they apply only to specific problems.

2.1 Flow configuration

The system consists of two coaxial disks of radius R , separated by a gap H . One of the disks, the rotor, rotates at the dimensional angular velocity $\Omega = \Omega_0$, while the stator is at rest. The two discs are shrouded by a wall rotating at the angular velocity of the rotor. The set-up can be seen in figure 2.1. We chose to non-dimensionalise all lengths by the gap H and time using $(\Omega_0)^{-1}$. Assuming a constant kinematic viscosity ν for the fluid, two non-dimensional parameters characterise this system, namely the geometric aspect ratio $\Gamma = R/H$ and the (gap-based) Reynolds number $Re = \Omega H^2/\nu$.

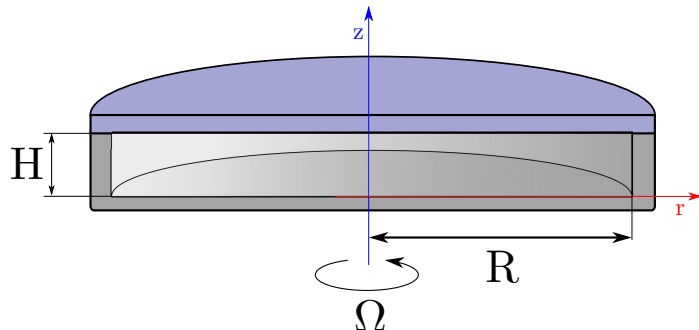


Figure 2.1: Rotor-stator geometry with rotating shroud. The set-up is characterised by the Reynolds number $Re = \Omega H^2/\nu$ and an aspect ratio $\Gamma = R/H$.

2.2 Governing equations

The non-dimensional velocity $\mathbf{u} = (u_r, u_\theta, u_z)$ and the non-dimensional pressure p obey the incompressible Navier-Stokes equations (2.1 – 2.4). Throughout the whole manuscript we assume that the flow is strictly axisymmetric. We consider the cylindrical coordinate system $(\mathbf{e}_r, \mathbf{e}_\theta, \mathbf{e}_z)$ in which the Navier-Stokes equations read :

$$\frac{\partial u_r}{\partial t} + \frac{1}{r} \frac{\partial r u_r u_r}{\partial r} + \frac{\partial u_z u_r}{\partial z} - \frac{u_\theta^2}{r} = - \frac{\partial p}{\partial r} + \frac{1}{Re} \left(\frac{1}{r} \frac{\partial}{\partial r} \left(r \frac{\partial u_r}{\partial r} \right) - \frac{u_\theta}{r^2} + \frac{\partial^2 u_r}{\partial z^2} \right) + f_r \quad (2.1)$$

$$\frac{\partial u_\theta}{\partial t} + \frac{1}{r} \frac{\partial r u_r u_\theta}{\partial r} + \frac{\partial u_z u_\theta}{\partial z} + \frac{u_r u_\theta}{r} = + \frac{1}{Re} \left(\frac{1}{r} \frac{\partial}{\partial r} \left(r \frac{\partial u_\theta}{\partial r} \right) - \frac{u_\theta}{r^2} + \frac{\partial^2 u_\theta}{\partial z^2} \right) + f_\theta \quad (2.2)$$

$$\frac{\partial u_z}{\partial t} + \frac{1}{r} \frac{\partial r u_r u_z}{\partial r} + \frac{\partial u_z u_z}{\partial z} = - \frac{\partial p}{\partial z} + \frac{1}{Re} \left(\frac{1}{r} \frac{\partial}{\partial r} \left(r \frac{\partial u_z}{\partial r} \right) + \frac{\partial^2 u_z}{\partial z^2} \right) + f_z \quad (2.3)$$

$$\frac{1}{r} \frac{\partial r u_r}{\partial r} + \frac{\partial u_z}{\partial z} = 0 \quad (2.4)$$

in which the vector $\mathbf{f} = (f_r, f_\theta, f_z)$ stands for a given forcing field cast in an additive form. The unforced case corresponds to $\mathbf{f} = \mathbf{0}$. The convective term is specified in the conservative form as this is the form in which it is implemented in the numerical code.

The coupled system of partial differential equations is complemented with the no-slip boundary conditions expressed as (2.5) :

$$\begin{cases} \mathbf{u} = r \mathbf{e}_\theta, & \text{at the rotor } (z = 0) \\ \mathbf{u} = \Gamma \mathbf{e}_\theta, & \text{at the shroud } (r = \Gamma) \\ \mathbf{u} = \mathbf{0}, & \text{on the stator } (z = 1). \end{cases} \quad (2.5)$$

2.3 Spatial discretisation

The continuous problem is discretised using a second order Finite Volume method on a staggered grid. Details on the staggered grid formulation can be found in (Hirsch, 2007, chap. 12). Staggered grid arrangement is presented in figure 2.2. As the geometry of the rotor-stator cavity flow is a rectangle, staggered mesh arrangement can be effectively used. The main motivation behind storing the velocity and pressure field values at different spatial locations is that the discretisation of the first derivatives with centred finite difference schemes (as used in this work) will inevitably lead to pressure oscillations when the variables are collocated (stored at the same position). Various methods to avoid this pressure oscillations, also known as checkerboard pressure distribution, are known, among them a Rhie-Chow interpolation (Rhie and Chow, 1983), used with the unstructured mesh arrangements. Whenever the geometry is simple enough the staggered mesh arrangement is known to lead to robust and reliable numerical schemes and will therefore be preferred in the current work.

In the staggered grid arrangement in the axisymmetric polar coordinate system configuration three different meshes are used: a mesh of pressure cells (also used to store the azimuthal velocity field), a mesh of radial and a mesh of axial velocity. The meshes of radial and axial velocity are translated in the respective coordinate direction. The walls of the finite volumes of the pressure mesh are exactly coinciding with the walls of the physical domain. The radial and axial meshes are shifted so that the radial (respectively axial) cell center coincides with the center of the right (respectively top) wall of the pressure cell. Such an arrangement suppresses the pressure oscillation modes caused by the finite difference schemes and greatly simplifies the implementation of the boundary conditions. Since the boundary conditions for the velocity are mostly of Dirichlet type they can be readily applied to the velocity variables lying on the domain walls. Staggered grid arrangement also does not require imposing any boundary condition of the pressure since the pressure cells from outside of the physical domain will never be referenced in the solution process. For the application of the

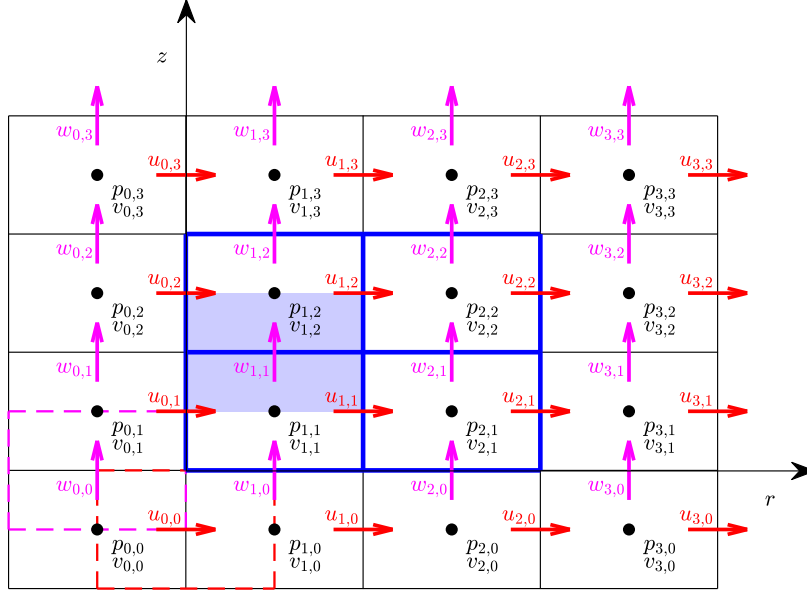


Figure 2.2: Staggered mesh arrangement with an example of 2 by 2 interior cells grid. Interior pressure cells are marked with bold blue line, ghost cells with black line. Axial velocity cell (1,1) is marked with light blue. Symbols u, v, w are used for the velocity components u_r, u_θ, u_z for readability purposes.

Dirichlet or Neumann boundary conditions for the velocity variables that do not lie on the domain walls an additional layer of ghost cells in introduced to the discretisation.

The staggered grid arrangement is presented in detail in figure 2.2 on a example of $N_r \times N_z = 2 \times 2$ mesh for simplicity. The mesh is kept uniform but the discretisation allows of course for nonuniform mesh cell size. To illustrate the discretisation process, one nonlinear term of the equation (2.3), namely $\frac{1}{r} \frac{\partial r u_r u_z}{\partial r}$, will be discretised in the interior cell (1,1) (marked with light blue in the figure). Its discretisation reads:

$$\frac{1}{r} \frac{\partial r u_r u_z}{\partial r} = \frac{1}{r_{1c}} \frac{r_e u_e w_e - r_w u_w w_w}{dr_1} \quad (2.6)$$

where r_{1c} is the radial position of the center of the pressure cell, r_e position of the east wall, r_w position of the west wall, dr_1 is the radial extent of the cell and u_e, u_w, w_e, w_w are the velocities interpolated to the east or west cell wall as:

$$u_w = \frac{u_{1,2}(z_{1n} - z_{1c}) + u_{1,1}(z_{2c} - z_{1n})}{z_{2c} - z_{1c}} \quad (2.7)$$

$$u_e = \frac{u_{0,2}(z_{1n} - z_{1c}) + u_{0,1}(z_{2c} - z_{1n})}{z_{2c} - z_{1c}} \quad (2.8)$$

$$w_w = \frac{w_{1,1} + w_{2,1}}{2} \quad (2.9)$$

$$w_e = \frac{w_{1,0} + w_{1,1}}{2} \quad (2.10)$$

All of the other terms in the continuous equations are discretised in the same manner. The above discretisation will be used throughout the manuscript to generate a set of nonlinear equations to be solved with various methods.

2.3.1 Mesh resolution

Two types of mesh are used in the study: uniform and non-uniform mesh. The non-uniform mesh is refined in the regions near discs and shroud. Table 2.1 present the size of each mesh used in the study. Refinement is the vicinity of the shroud and the discs follows the formulae:

resolution	N_r	N_z	type	DOF
D0	300	80	uniform	99 k
R0	600	160	uniform	390 k
R1	683	128	non-uniform	356 k
R2	1024	192	non-uniform	796 k
R3	1536	288	non-uniform	1.8 m
R4	2304	432	non-uniform	4 m
R5	3456	648	non-uniform	9 m

Table 2.1: Mesh resolutions used in the study. N_r is the number of interior pressure cells in r direction, N_z in z direction. Column DOF specifies the number of degrees of freedom of the system equal $4(N_r + 2)(N_z + 2)$

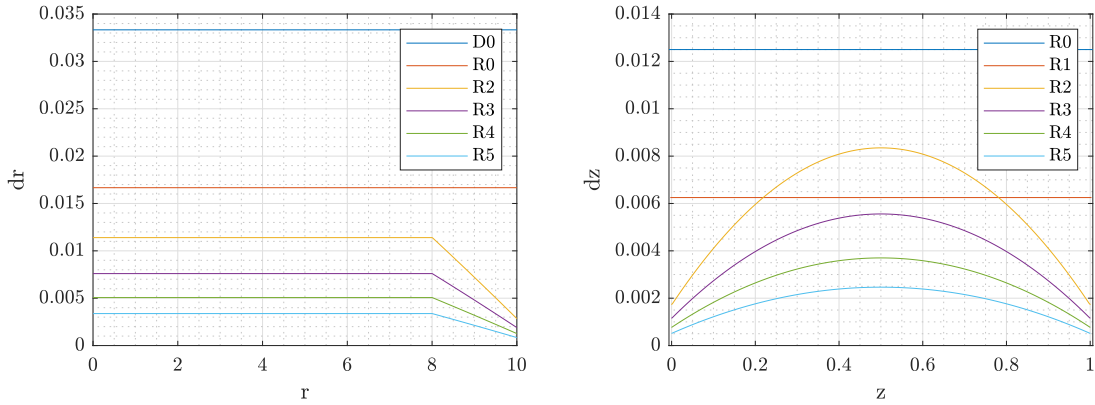


Figure 2.3: Pressure cell size in r (left) and z (right) direction for each mesh listed in table 2.1.

$$b_i = \frac{1}{2} \left(1 + \frac{\tanh(\delta(x_i - \frac{1}{2}))}{\tanh(\delta/2)} \right) \quad (2.11a)$$

$$r_i = 8 + 2 \cdot \frac{b_i}{(a + (1 - a)b_i)} \quad (2.11b)$$

with $\delta = 0.7258$ and $a = 0.4989$, where $x_i \in (0, 1)$ is the uniform mesh. 70% of total number of N_r grid points are used in the uniform region $r \in (0, 8)$ and the remaining 30% are used in the non-uniform region $r \in (8, 10)$. The non-uniform mesh in the axial direction follows the formula

$$z_i = \frac{1}{2} \left(1 + \frac{\tanh(\delta(\frac{i}{N_z} - \frac{1}{2}))}{\tanh(\delta/2)} \right) \quad (2.12a)$$

with $\delta = 2.8587$.

In figure 2.3 the size of a pressure cell corresponding to each mesh resolution is plotted. It can be seen that the non-uniform mesh in r direction is refined only near the shroud and is uniform for most of the domain. Additionally in figure 2.4 the mesh for the resolution R2 is visualised by plotting each eighth cell wall. Again the refinement near walls can be observed.

2.4 Determination of the steady state solution using the Newton method

Upon discretisation the equations (2.1–2.4) yield a system of nonlinear algebraic equations that can be solved using Newton algorithm. Unknown values of velocity and pressure fields discretised on the

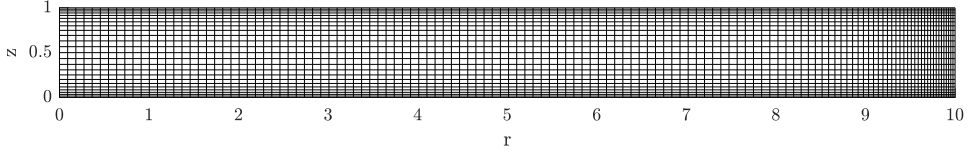


Figure 2.4: Mesh visualisation for the resolution R2. Each eighth cell wall is plotted for better clarity.

staggered mesh are stored in a solution vector:

$$\mathbf{q} = [p_{0,0}, u_{0,0}, v_{0,0}, w_{0,0}, p_{0,1}, u_{0,1}, v_{0,1}, w_{0,1}, \dots]^T \quad (2.13)$$

Size of \mathbf{q} is $4(N_r + 2)(N_z + 2)$. Discretised governing equations and the boundary conditions are stored in the same \mathbf{g} . To find the solution of the system:

$$\mathbf{g} = 0 \quad (2.14)$$

Newton algorithm in the form:

$$\mathbf{q}^{n+1} = \mathbf{q}^n - (\nabla \mathbf{g})^{-1} \mathbf{g}(\mathbf{q}^n) \quad (2.15)$$

is applied in the iterative manner until convergence. Matrix $\nabla \mathbf{g} = \frac{\partial g_i}{\partial q_j}$ is the Jacobian of the system linearised around the current solution vector \mathbf{q} . Upon correct discretisation on the staggered grid the only non-null vector in the kernel of the Jacobian is a constant pressure mode. This corresponds to the pressure in the Navier-Stokes equation that is always determined up to an additive constant. To eliminate this mode from the kernel of the Jacobian one of the continuity equations in the discrete system is exchanged with a constraint $p = 0$. Jacobian constructed in this way is then full rank and can be inverted. Solution of the linear system with the Jacobian matrix is done using a sparse direct solver UMFPACK. Convergence is attained if:

$$\sqrt{< \mathbf{g}, \mathbf{g} >} < \varepsilon \quad (2.16)$$

with an arbitrary small value ε taken 10^{-10} .

2.4.1 Linear stability analysis of the steady state solution

The stability of the base flow is studied by introducing infinitesimal perturbation to the velocity and pressure fields in the following form:

$$\mathbf{u} = \mathbf{U}_b + \mathbf{u}' e^{\lambda t} + \mathbf{u}'^* e^{\lambda^* t} \quad p = P_b + p' e^{\lambda t} + p'^* e^{\lambda^* t} \quad (2.17)$$

The asterisk denotes complex conjugate. Plugging this *ansatz* into the Navier-Stokes equations and linearising around (\mathbf{U}_b, P_b) yields the new system

$$\lambda \mathbf{u}' + (\mathbf{u}' \cdot \nabla) \mathbf{U}_b + (\mathbf{U}_b \cdot \nabla) \mathbf{u}' = -\nabla p' + \frac{1}{Re} \nabla^2 \mathbf{u}' \quad (2.18a)$$

$$\nabla \cdot \mathbf{u}' = 0 \quad (2.18b)$$

After spatial discretisation the above system can be re-cast into the generic form

$$\mathbf{J} \mathbf{q}' = \lambda \mathbf{B} \mathbf{q}' \quad (2.19)$$

where $\mathbf{q}' = (u'_r, u'_\theta, u'_z, p')$, \mathbf{J} is the Jacobian evaluated on the base flow (\mathbf{U}_b, P_b) and \mathbf{B} is the identity matrix except for the rows corresponding to the continuity equation and boundary conditions. The

eigenvalues λ ($= \lambda_r + i\lambda_i$) of the generalised eigenproblem (2.19) are found numerically using the ARPACK library in the shift-invert mode. For a generalised eigenvalue problem:

$$\mathbf{A}\mathbf{v} = \lambda\mathbf{B}\mathbf{v} \quad (2.20)$$

a shift-invert method finds a subset of eigenvalues closest to a complex shift σ by repeated Arnoldi iteration:

$$\nu\mathbf{v} = (\mathbf{A} - \sigma\mathbf{B})^{-1}\mathbf{B}\mathbf{v} \quad (2.21)$$

where the original eigenvalues λ can be retrieved with:

$$\nu = \frac{1}{\lambda - \sigma} \quad (2.22)$$

2.5 Temporal integration of the governing equations

Temporal integration of the equations governing a fluid flow has a rich history where many temporal schemes have been proposed depending on the class of the problem. In the current work a prediction-projection algorithm in the rotational pressure correction formulation (Guermond et al., 2006) together with Backwards Differentiation Formula 2 scheme (BDF2) has been adopted.

The algorithm consists of two main parts:

1. prediction of the non-divergence free intermediate velocity field u_i^* (index i stands for the velocity component, $*$ for intermediate field)
2. projection of u_i^* on the space of divergence free velocity fields

Those two steps are executed in each timestep of the time integration code.

2.5.1 Prediction step

Upon introduction of BDF2 scheme into the momentum equations we get:

$$\frac{3u_i^n - 4u_i^{n-1} + u_i^{n-2}}{2dt} + 2C^n - C^{n-1} = -\nabla p^n + \frac{1}{Re}\Delta u_i^* \quad (2.23)$$

where: u_i^n is the velocity at current timestep n , u_i^{n-1} the velocity at the previous timestep, C non-linear convective term evaluated at the corresponding timestep, p^n pressure field at the current timestep. It is noted that the convective term is linearly extrapolated to the next timestep (i.e. it is equal $2C^n - C^{n-1}$), gradient of the pressure field is present in the prediction step (this is not the case in the original Chorin's projection scheme) and the diffusion term is treated implicitly.

Instead of solving (2.23) for u_i^* we introduce the decomposition:

$$u_i^* = u_i^n + \delta u_i^* \quad (2.24)$$

and transform (2.23) into:

$$\left(1 - \frac{2dt}{3Re}\Delta\right)\delta u_i^* = \frac{2dt}{3} \left(\frac{u_i^n - u_i^{n-1}}{2dt} - (2C^n - C^{n-1}) - \nabla p^n + \frac{1}{Re}\Delta u_i^n \right) \quad (2.25)$$

This is called incremental formulation of the prediction step. Equation (2.25) form a Helmholtz problem for each velocity component. Right hand side of (2.25) depends only on the current and past timesteps and can be evaluated at each timestep. Left hand side (LHS) of (2.25) is a differential operator acting on the unknown field δu_i^* . Upon discretisation LHS corresponds to a product of a pentadiagonal matrix and a vector. In order to avoid having to invert the pentadiagonal matrix in the LHS, an alternating-direction implicit (ADI) method is used to solve a collection of tridiagonal problems, each of which is solved directly using a Thomas algorithm (Thomas, 1949) (simplified Gaussian elimination for the tridiagonal systems). When the prediction step is expressed in the incremental form the ADI conserves the second order time accuracy of the BDF2 scheme. Details on the ADI method can be found in (Moin, 2010)

The prediction step results in the intermediate velocity field u_i^* .

2.5.2 Projection step

By subtracting equation (2.23) from:

$$\frac{3u_i^{n+1} - 4u_i^n + u_i^{n-1}}{2dt} + 2C^n - C^{n-1} = -\nabla p^{n+1} + \frac{1}{Re} \Delta u_i^{n+1} \quad (2.26)$$

we get:

$$\frac{3}{2dt} (u_i^{n+1} - u_i^*) = -\nabla \delta p + \frac{1}{Re} \Delta (u_i^{n+1} - u_i^n) \quad (2.27)$$

where $\delta p = p^{n+1} - p^n$. If we assume that the velocity u_i^{n+1} should be divergence free (i.e. $\nabla \cdot \mathbf{u}^{n+1} = 0$), taking the divergence of (2.27) we get:

$$\frac{3}{2dt} \nabla \cdot \mathbf{u}^* = \Delta \left(\delta p + \frac{1}{Re} \nabla \cdot u^* \right) = \Delta \phi \quad (2.28)$$

Solving the Poisson problem (2.28) with the homogeneous Neumann boundary condition for ϕ yields the corrections to the pressure and velocity:

$$p^{n+1} = p^n + \phi - \frac{1}{Re} \nabla \cdot u^* \quad (2.29)$$

and assuming $\nabla \times \nabla \times u_i^{n+1} = \nabla \times \nabla \times u_i^*$

$$u_i^{n+1} = u_i^* - \frac{2dt}{3} (\nabla \phi) \quad (2.30)$$

that guarantee the u_i^{n+1} to be divergence free. p^{n+1} and u^{n+1} are therefore the outcome of one prediction-projection step.

2.6 Codes developed in the scope of the project

In the scope of the project a C++ code was developed. Most of the results presented in the current work are obtained using this code. Main capacities of the code include:

1. finding a steady state solution of the Navier-Stokes equations in polar coordinates for the axisymmetric rotor-stator case or in Cartesian coordinates for the differentially heated cavity problem (described in chapter 6) on a uniform and nonuniform grid
2. linear stability analysis of a base flow
3. temporal integration of the rotor-stator and differentially heated cavity cases. Time integration can be conducted in full field or perturbation field mode which allows for the time integration linearised around a given base flow.
4. application of the first order steady state forcing as required by the Self Consistent Model (described in chapter 4)
5. description of a limit cycle as a sum of Fourier or Chebyshev modes (described in chapter 4 and 6)
6. pseudo arclength continuation of the solutions described as the sum of Fourier modes (described in chapter 4 and 6)

Code uses the libraries: Eigen (for the algebraic operations), UMFPACK (for solution of the sparse linear systems) and ARPACK (for solving the eigenvalue problems). Interfaces to PETSc and SLEPc libraries were also developed. Additionally, for almost all visualisation purposes and for finding the optimal response of the system (as described in chapter 5) MATLAB was extensively used in the project.

Chapter 3

Base state and its stability

In this chapter the main characteristics of the laminar base flow solution are discussed. Firstly, the 2D base flow is compared against its 1D self similar counterpart. It is shown that the assumption of self-similarity holds in the $O(1)$ region near the axis. Then the linear stability of the base flow is discussed. Sensitivity of the Re_c on the spatial discretisation is shown. It is in particular shown that the discontinuous boundary condition in the corner of the domain is not affecting severely the Re_c accuracy. The chapter finishes with the discussion of the high levels of non-normal growth present in the system.

3.1 Base flow

The base flow is the unique steady axisymmetric velocity field \mathbf{U}_b solution to the governing equations (2.1-2.4) compatible with the boundary conditions (2.5). It is found using the Newton algorithm described in section 2.4. The base flow is associated with a pressure field p_b defined up to an additive constant. It consists, for high enough Re , of two boundary layers, one on each disk, and a core region. Fluid is forced into circulation around the cavity by the rotation of the bottom disc. It is advected towards the rotating shroud and returns towards the axis along the stationary disk. In figure 3.1 isocontours of u_θ fields are plotted for increasing Re . The recirculation in the meridional plane is shown using the meridional streamlines in figure 3.1. For high enough Re the core region between the boundary layers appears almost independent of z .

3.2 Comparison against the self-similar profile

The stability of the flow between rotating discs can be analysed by considering a self-similar profile between the discs. This is the approach taken by Serre et al. (2004), where the stability of the profile is analysed with techniques of spatio-temporal analysis, introduced to the rotating disc flows by Lingwood (1997) for the flow over a single rotating disc. While it is true that the velocity profile between the rotating infinite discs is self-similar (depends nontrivially on z only and r dependence is linear) this is not the case when the geometry is shrouded by a wall. To illustrate the r dependence of the velocity profile the azimuthal velocity divided by the radial location is plotted in figure 3.2. Wherever the self-similarity assumption is valid the velocity profiles scaled by the radial position should overlap. This is approximately the case for the whole cavity at $Re = 1$, however only at $r < 1$ for $Re = 70$ or $r < 3$ for $Re \geq 250$. the fact of limited applicability of self-similar profile was also pointed out by Brady and Durlofsky (1987). The validity of the self-similar profile is rather limited and special care should be taken while trying to translate the results obtained with the analysis of infinite geometries to finite geometries. In the current work only the 2D geometry of finite radial extent is analysed.

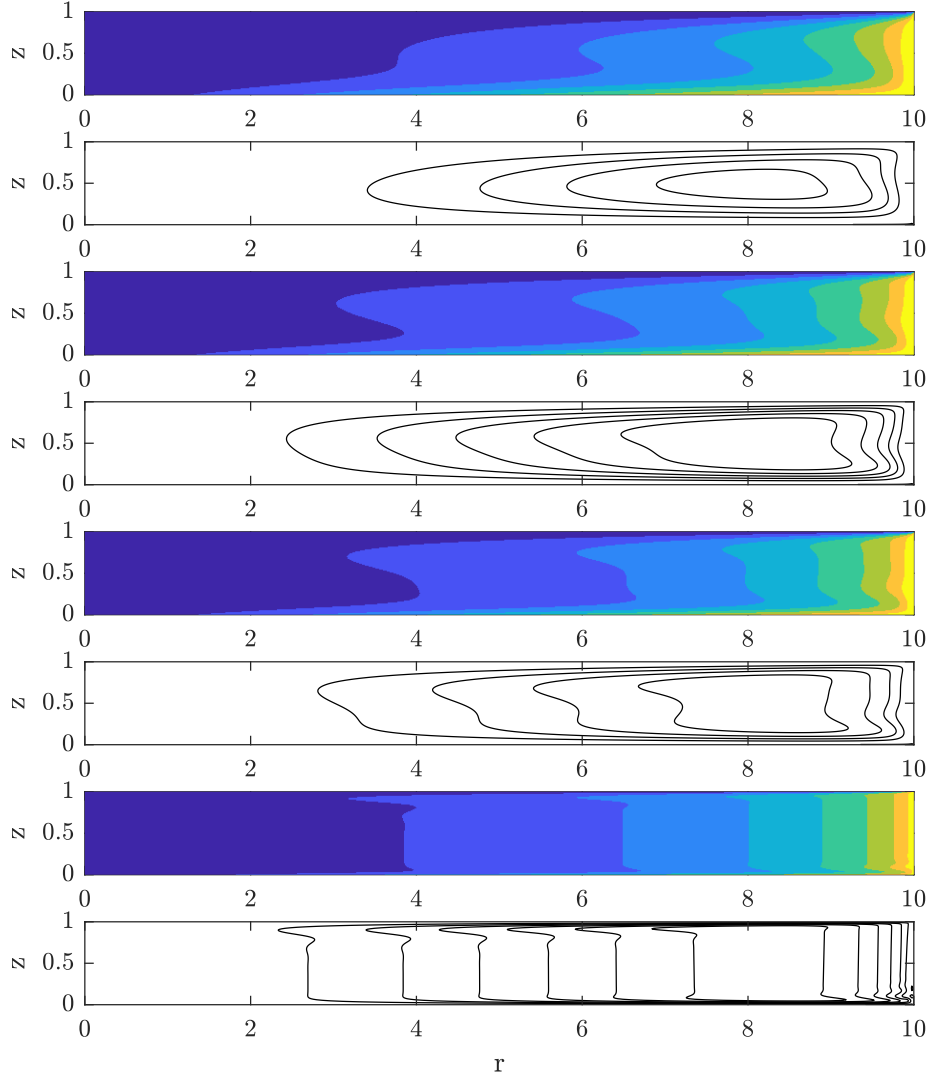


Figure 3.1: Axisymmetric base flow solution for $\Gamma = 10$. Visualisations in a meridian section. From top to bottom : $Re=70, 150, 250, 3000$. Azimuthal velocity $u_\theta(r, z)$ (the colormap divides the interval $(0,10)$ in 8 equal subintervals) and streamfunction $\psi(r, z)$ defined implicitly by $u_r = \frac{1}{r} \frac{\partial \psi}{\partial z}$ and $u_z = -\frac{1}{r} \frac{\partial \psi}{\partial r}$ (plotted values : $\psi_{Re=70} = 1, (1), 4$. $\psi_{Re=150} = 0.5, (0.5), 2.5$. $\psi_{Re=250} = 0.5, (0.5), 2$. $\psi_{Re=3000} = 0.1, (0.1), 0.6$. $\psi = 0$ corresponds to the wall.) Numerical resolution R1.

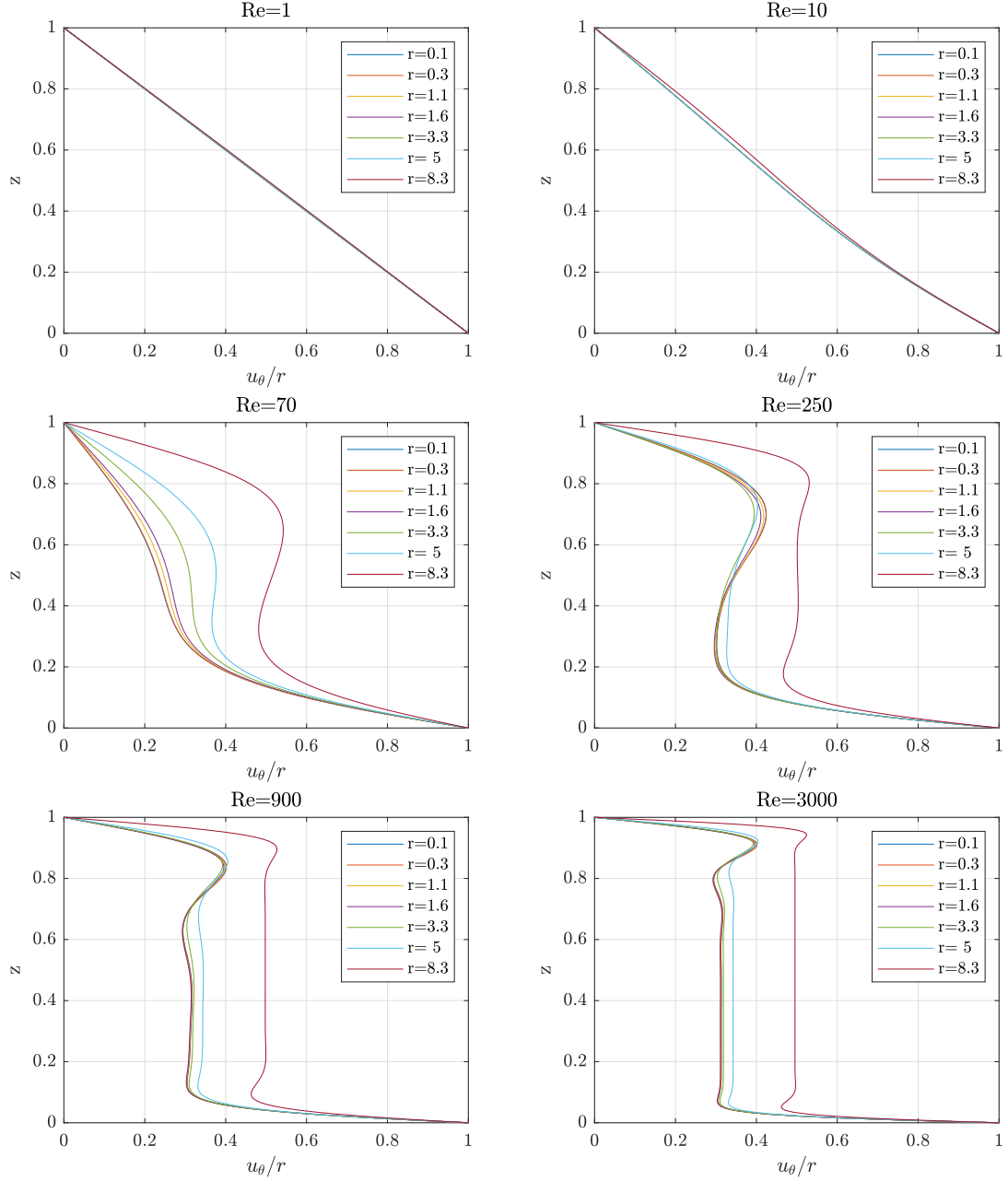


Figure 3.2: Azimuthal velocity of the base flow scaled by the radial position indicating approximately the region of validity of self-similar solution in the shrouded geometry. It can be noted that the angular velocity of the bulk between the discs should be equal 0.313Ω as noted by Launder et al. (2010). This is indeed the case for high $Re = 3000$ and radial positions close to the axis $r < 3$.

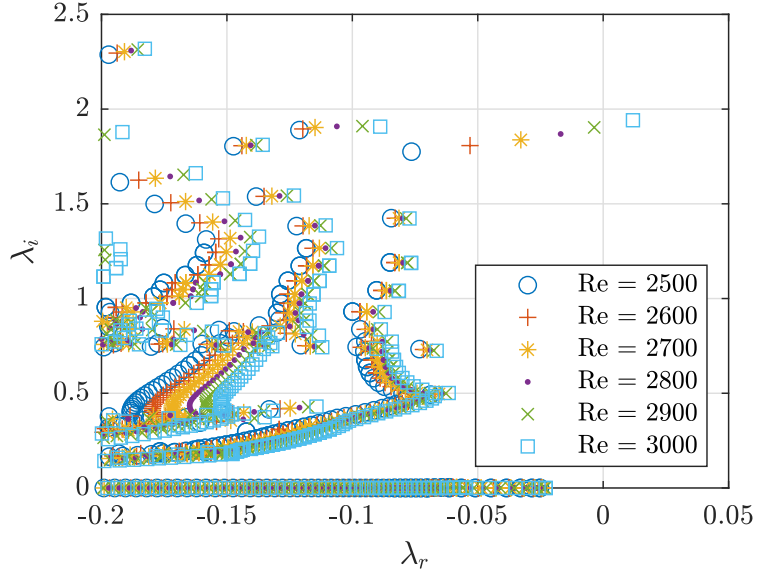


Figure 3.3: Spectrum of the linearised Navier-Stokes operator. Resolution R1.

3.3 Linear stability analysis

The eigenvalues $\lambda (= \lambda_r + i \lambda_i)$ of the generalised eigenproblem (2.19) are found numerically using the ARPACK library in the shift-invert mode. For each shift $\sigma = 0.1 i, 0.5 i, 1.0 i, 2.0 i$, a fixed number of 200 of eigenvalues is found. Part of the resulting spectrum is shown in figure 3.3 for Re below and above the instability threshold. The least stable eigenvector for $Re = 3000$ is visualised in figures 3.4(a-b). This eigenvector consists mainly of a steady wavepacket of counter-rotating rolls localised inside the Bödewadt layer. The largest amplitude of these rolls corresponds to $1 \leq r \leq 2$. Weaker yet larger-scale wave-like structures can also be observed outside the Bödewadt layer, displaying various inclinations depending on the radial position. They are interpreted as eigen-oscillations due to the rotation of the core, like inertial waves (whose wavevector's orientation is directly dependent on the ratio between angular frequency and rotation rate) except that the rotation rate varies spatially, like in other non-confined vortical flows (Fabre et al., 2006). Both the rolls and the wave-like structure make up the oscillatory eigenmode. For clearer evidence about the relevance of inertial oscillations to the eigenmodes, we illustrate in figure 3.4c another eigenmode from the spectrum at $Re = 3000$, with angular frequency $\lambda_i \approx 0.5$ smaller than for the leading eigenmode. This eigenmode does not feature any roll structure inside the Bödewadt layer but features energetic oblique structures with a tighter angle consistently with the expected behaviour for inertial waves. A more detailed investigation of inertial wave contributions to enclosed rotating flows is left for a specific study.

3.4 Threshold sensitivity to the numerical resolution

The sensitivity of the critical Reynolds number is addressed with respect to the numerical mesh and to the way the singular boundary conditions are treated numerically. Since the rotating shroud wall meets the stationary stator disc a discontinuity of the boundary condition for the azimuthal velocity is present in the associated corner. Such discontinuities are known to deteriorate the accuracy of spectral simulations, which has promoted the use of regularisation techniques used in (Lopez et al., 2009; Serre et al., 2004).

The sensitivity of the instability threshold is tested by using a series of meshes summarised in table 3.1 which reports the value of Re_c for each spatial discretisation. The same data is also plotted in figure 3.5. Additionally, the influence of *regularizing* the corner singularity is also considered. This is achieved here by smoothing out the boundary condition at the Bödewadt corner, imposing an exponential velocity profile of the form $v = \Gamma \exp\left(\frac{r-\Gamma}{\varepsilon}\right)$. Two regularisations have been considered

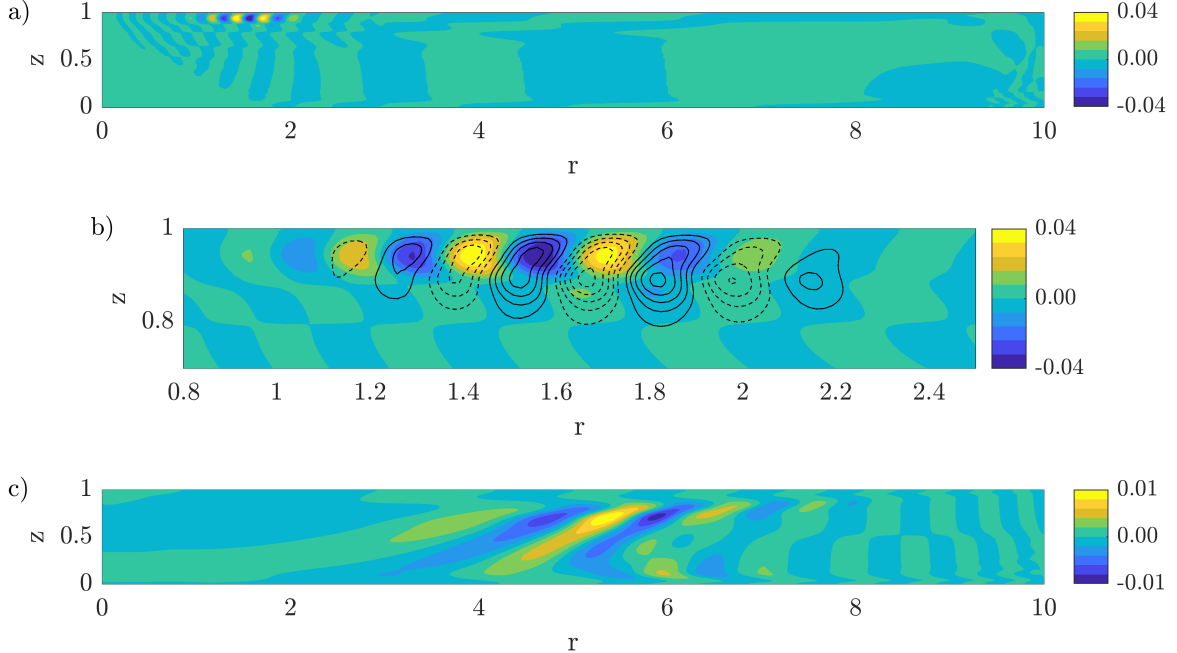


Figure 3.4: a) Azimuthal velocity component of the unstable eigenvector at $Re = 3000$, b) zoom of a) with streamfunction isocontours superimposed for $\psi' = -2.5 \times 10^{-4}$ to 2.5×10^{-4} with increments for isocontours of 5×10^{-5} (negative values are dashed lines), c) Same as a) for another eigenmode for $Re = 3000$ with $\lambda = -0.062 + 0.49i$. Resolution R1 (see Table 2.1).

: $\varepsilon = 0.003$ and $\varepsilon = 0.006$. The case without any regularization ($u_\theta = 0$) is referred to as $\varepsilon = 0$ for ease of notation.

The spatial discretisation of the governing equations and boundary conditions is second order accurate. It can be therefore expected that the value of Re_c also converges with the same order as the mesh is refined. The order of convergence for Re_c is estimated based on three different resolutions R2, R3 and R4 as

$$\text{order} = \log_{1.5} \left(\frac{Re_{c,R3} - Re_{c,R2}}{Re_{c,R4} - Re_{c,R3}} \right) \quad (3.1)$$

The choice of the base 1.5 for the logarithm reflects the ratio between consecutive grids in Table 3.1. As also noted in the table, the order of convergence is close to 2.0, irrespective of the regularisation used. Smoothing out the discontinuous boundary condition, although it affects quantitatively Re_c , does not affect the order of convergence. The dependence of Re_c on the regularisation is due to the modification of the base flow linked to the modified boundary condition on the stator and not to the removal of the singularity. We conclude that using a discontinuous boundary condition does not deteriorate the results of the finite difference approximations used throughout this study. Similar conclusions were drawn for the lid-driven cavity, which also displays corner singularities, see e.g. the recent review Kuhlmann and Romanò (2019). As a compromise the spatial resolution R2 with no corner regularisation will provide meaningful results while requiring a manageable computational effort. As a computationally cheaper compromise spatial resolution R0 will also be extensively used.

3.5 Non-normality of the linearised dynamics

As noted in Daube and Le Quéré (2002), the dynamics linearised around the base flow in the rotor-stator cavity is strongly non-normal. Because the eigenvectors of the linearised operator are not mutually orthogonal a transient growth of the perturbation energy can take place even in the stable setting, as noted in the review article of Chomaz (2005). To assess the strength of the non-normality a linear time integration of the Navier-Stokes equations is performed. A divergence-free, random uniformly distributed perturbation is added at $t = 0$ to the azimuthal component $U_{b\theta}$ of the base

resolution	N_r	N_z	type	DOF	$\varepsilon = 0$	$\varepsilon = 0.003$	$\varepsilon = 0.006$
D0	300	80	uniform	99 k			
R0	600	160	uniform	390 k	2925.47		
R1	683	128	non-uniform	356 k	2963.41	2985.43	3035.61
R2	1024	192	non-uniform	796 k	2773.3	2789.01	2826.55
R3	1536	288	non-uniform	1.7 m	2697.48	2711.71	2746.33
R4	2304	432	non-uniform	4.0 m	2663.96	2677.9	2711.97
R5	3456	648	non-uniform	9.0 m	2648.9	2662.8	2696.8
				extrapolation	2636.61	2650.59	2684.81
				order	2.01	2.04	2.09

Table 3.1: Critical Reynolds number Re_c depending on the spatial discretisation. From R2 to R5 the ratio between two consecutive grid resolutions is 1.5 in each direction. No Re_c could be found for the resolution D0 probably in connection to the mesh being too coarse.

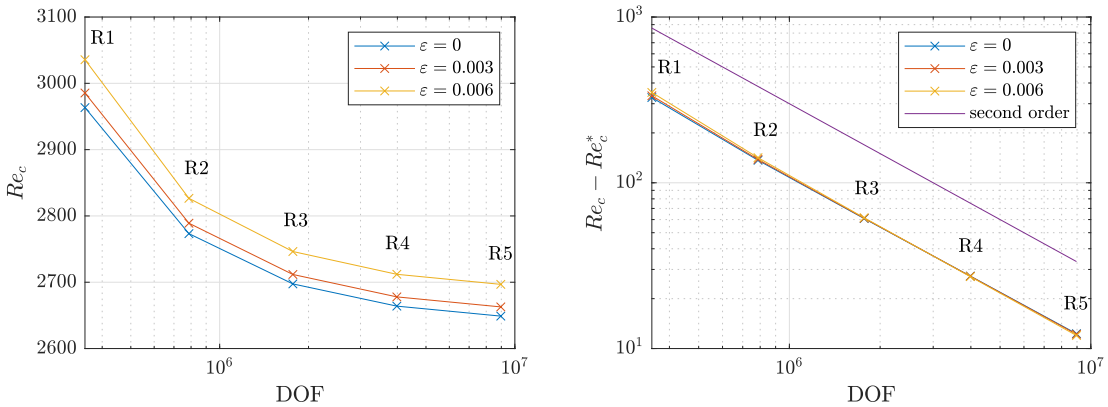


Figure 3.5: Left: critical Reynolds number Re_c depending on the spatial discretisation in the case of regularised and non-regularised corner singularity. Right: absolute error calculated using the Richardson extrapolated value Re_c^* compared with a second order convergence curve.

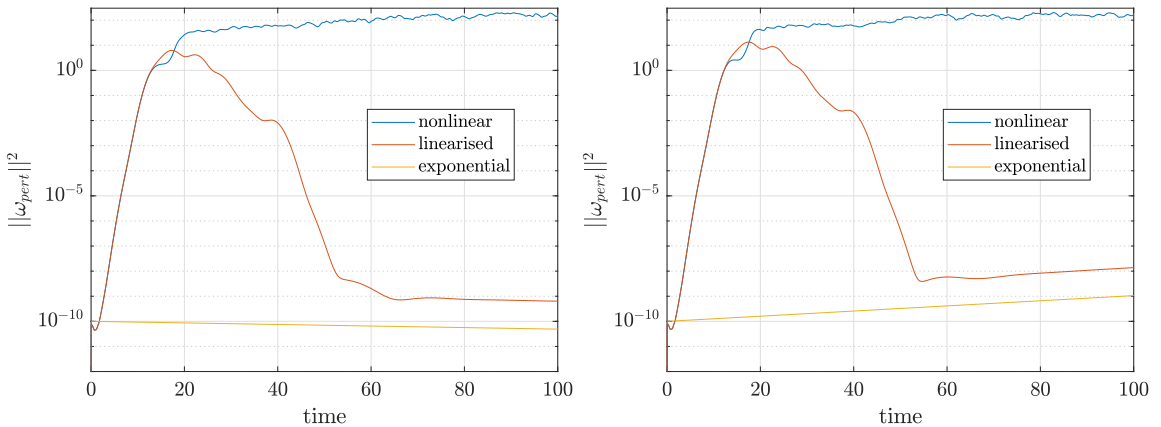


Figure 3.6: Time evolution of the observable $a^2 (= \|\omega_{pert}\|^2)$ in linear and non-linear time integration at $Re = 2900 > Re_c$ (left) and $Re = 3000 > Re_c$ (right). The slope of the late time evolution of the observable in the linear code is compared with the exponential growth $\propto \exp(2\lambda_r t)$ associated with the least stable eigenmode. Spatial resolution R0.

flow. The equations linearised around the base flow are then advanced in time. Rather than focusing on the traditional energy gain as in Ref. Daube and Le Quéré (2002), here we monitor in time the L_2 -norm of the azimuthal vorticity perturbation

$$a(t) = \|\omega_{pert}\| = \sqrt{\int |\omega - \omega_b|^2 r dr dz}, \quad (3.2)$$

(where $\omega = \partial_z u_r - \partial_r u_z$ is the azimuthal vorticity component, ω_b the equivalent quantity for the base flow and ω_{pert} the equivalent quantity for the velocity perturbation) whose square is plotted in Figure 3.6.

The time evolution of $a(t)$ resulting from linearised and non-linear time integrations are compared in Figure 3.6. Initially almost identical, these signals diverge when the nonlinear code starts to approach the large amplitude solution branch. The observable a^2 , initially around 10^{-10} , is amplified by more than twelve orders of magnitude in less than 20 time units, before it starts to decrease. A growth in energy of this order was also reported in Daube and Le Quéré (2002). High levels of non-normal growth are expected to lead to additional difficulties in the present analysis. In particular it makes it impossible to use only a time integrator to capture the base flow and one has to resort to the Newton solver instead. With a time integrator, in the subcritical regime, despite the formal property of linear stability of the base flow, a small perturbation resulting from a very small increment in Re will be strongly amplified and will, *in practice*, lead to the chaotic attractor.

For $Re = 2900$ which is below Re_c , linear stability predicts a negative growth rate. This is visible here in Fig. 3.6 (left) in the asymptotic exponential decay. The quantitative negative growth rate $\lambda = -3.58 \times 10^{-3}$ matches well the final exponential decay (multiplied by two since a^2 is considered rather than a). For $Re = 3000$ which exceeds Re_c , the decrease of a^2 is followed by an exponentially increase. The exponential growth associated with the most unstable eigenvalue $\lambda = 1.18 \times 10^{-2}$, for the corresponding Re , is plotted in Fig. 3.6 (right). The good agreement at late times confirms the prediction from linear stability analysis.

Chapter 4

Subcritical axisymmetric solutions

In this chapter the existence of self-sustained states in the rotor-stator flow is studied. It is first confirmed that there exists a branch emanating at Re_c . This branch of periodic states born in a Hopf bifurcation, identified using a Self-Consistent Method (SCM) and arclength continuation, is found to be supercritical. The associated solutions only exist, however, in a very narrow range of Re . Another subcritical branch of periodic solutions is found using the Harmonic Balance Method with an initial guess obtained by SCM. In addition, the existence of a branch of large amplitude chaotic solutions is confirmed. Edge states separating the steady laminar and chaotic regimes are identified using a bisection algorithm. These edge states are bi-periodic in time for most values of Re . Both subcritical solution branches fold around at approximately the same value of Re , which is lower than Re_c yet still larger than the values reported in experiments. This suggests that, at least in the absence of external forcing, sustained chaotic rolls are not the phenomenon observed in the experiments.

4.1 Periodic solutions

Finding the critical Reynolds number Re_c associated with the first destabilisation of the laminar base flow, as shown in chapter 3, is the starting point in the construction of a bifurcation diagram. The rest of the chapter is devoted to a more complete description of this bifurcation diagram. Since the loss of stability at $Re = Re_c$ is due to a pair of complex conjugate eigenvalues, it corresponds to a Hopf bifurcation, from which a nonlinear branch of oscillatory solutions is expected to arise. If the branch bifurcates towards $Re < Re_c$ and features unstable periodic orbits in the neighbourhood of Re_c , the bifurcation is said to be subcritical. If it bifurcates towards $Re > Re_c$ and features stable limit cycles in the neighbourhood of Re_c , it is said to be supercritical. The periodic solutions can then be continued further in parameter space using arclength continuation.

In order to identify oscillatory solutions near a Hopf bifurcation point, the recent Self-Consistent Method (SCM) (Mantić-Lugo et al., 2014) will be used. It was previously used with success for the supercritical bifurcation of the two-dimensional wake behind a circular cylinder (Mantić-Lugo et al., 2014). A quick summary of the method is presented in Subsection 4.1.1.

An *a priori* reasonable expectation, given the sustained subcritical states observed in Ref. Daube and Le Quéré (2002), is that a Hopf branch of unstable solutions bifurcates subcritically directly from the base flow at $Re = Re_c$. Such a branch could ideally be continued down to low values of Re , before it folds back and bifurcates into new solutions that form the backbone of the chaotic attractor (as in e.g. Ref. Avila et al. (2013)). This expectation will be confronted with the present results in Subsection 4.1.3. In the quest for the Hopf branch using SCM, another branch of periodic solutions was unexpectedly found, which will be reported in Subsection 4.1.4. As will be shown, unlike the Hopf branch which appears in fact supercritical, this new branch is subcritical and does extend to low Re values.

4.1.1 Self-Consistent Method (SCM)

The SCM serves as an algorithmic tool to find the periodic solutions of the system (2.1 – 2.4) near a Hopf bifurcation point. It assumes that the periodic solution can be described as a sum of a steady field \mathbf{U} (the *mean flow*, which is generally distinct from the base flow) and an oscillatory field of complex amplitude \mathbf{u}' together with its complex conjugate \mathbf{u}'^* (the *oscillatory mode*). Denoting \mathbf{U} the mean velocity field and P the mean pressure field, the following ansatz is considered with λ a complex number ($\lambda = \lambda_r + i\lambda_i$) and λ^* its conjugate :

$$\mathbf{u} = \mathbf{U} + A(\mathbf{u}'e^{\lambda t} + \mathbf{u}'^*e^{\lambda^*t}) \quad (4.1a)$$

$$p = P + A(p'e^{\lambda t} + p'^*e^{\lambda^*t}) \quad (4.1b)$$

The additional real parameter A is introduced to cope with the fact that \mathbf{u}' is defined up to a multiplicative constant. The ansatz (4.1) is introduced into the Navier-Stokes equation (2.1 – 2.4). Separating the steady and oscillatory parts, and retaining only the terms oscillating at angular frequency $\pm\lambda_i$, the resulting set of equations is

$$(\mathbf{U} \cdot \nabla)\mathbf{U} + 2A^2(\mathbf{u}'^* \cdot \nabla)\mathbf{u}' = -\nabla P + \frac{1}{Re}\nabla^2\mathbf{U}, \quad \nabla \cdot \mathbf{U} = 0, \quad (4.2a)$$

$$\lambda\mathbf{u}' + (\mathbf{u}' \cdot \nabla)\mathbf{U} + (\mathbf{U} \cdot \nabla)\mathbf{u}' = -\nabla p' + \frac{1}{Re}\nabla^2\mathbf{u}', \quad \nabla \cdot \mathbf{u}' = 0. \quad (4.2b)$$

Equation (4.2a) forms a forced nonlinear steady Navier-Stokes equation for the field \mathbf{U} with a forcing term proportional to $(\mathbf{u}'^* \cdot \nabla)\mathbf{u}'$. Equation (4.2b) results from the formal linearisation of the Navier-Stokes equations around the mean flow \mathbf{U} . This amounts to neglecting all $o(A)$ terms (which is consistent with discarding terms that oscillate at $2\lambda_i$) even if in practice we will consider $A = O(1)$. Equation (4.2b) is an eigenvalue problem of the same form as equation (5.1-5.2) except that \mathbf{U}_b is replaced by \mathbf{U} . The associated eigenvector $\mathbf{q}' = (u'_r, u'_\theta, u'_z, p')$, computed using ARPACK, is normalised to unit amplitude with respect to the \mathbf{B} matrix (2.19) such that $\mathbf{q}'^*\mathbf{B}\mathbf{q}' = 1$. By starting from suitable guesses for \mathbf{U} and \mathbf{u}' for a given parameter A , an iterative method is used to solve the two equations (4.2a) and (4.2b) alternately until convergence. The next value for A is then sought for iteratively using a secant method until the steady state \mathbf{U} becomes neutrally stable, i.e. $\lambda_r = 0$. We emphasize that SCM operates according to two loops, an inner and an outer one. In the inner loop the equations (4.2a)-(4.2b) are solved alternately, for fixed A , with the result of one equation feeding the other one until convergence. In the outer loop the parameter A is changed using a secant method until $\lambda_r = 0$. The whole procedure results in the oscillatory solution described by equations (4.1a) and (4.1b). More details on the method can be found in Ref. Mantić-Lugo et al. (2015).

4.1.2 Harmonic Balance Method (HBM)

The Newton method discussed in section 2.4 was used to identify steady state solutions. It can be generalised for the identification of periodic orbits. While the use of a Newton method for steady states is standard procedure, its generalisation to periodic orbits has only been used recently in fluid dynamics and is thus explained in more detail here. Exactly periodic solutions can be approximated by a finite Fourier expansion of the form

$$\mathbf{u}(\mathbf{x}, t) = \mathbf{U}(\mathbf{x}) + \sum_{k=1}^{nt} \{\mathbf{u}_k(\mathbf{x})e^{ik\omega t} + \mathbf{u}_k^*(\mathbf{x})e^{-ik\omega t}\} \quad (4.3a)$$

$$p(\mathbf{x}, t) = P(\mathbf{x}) + \sum_{k=1}^{nt} \{p_k(\mathbf{x})e^{ik\omega t} + p_k^*(\mathbf{x})e^{-ik\omega t}\} \quad (4.3b)$$

where ω is a (real) angular frequency, nt is a finite positive integer and the asterisk stands again for complex conjugate. The identification of periodic orbits based on this truncated Fourier expansion is sometimes described as the Harmonic Balance Method in the literature, which was recently used in different flow cases (Bengana and Tuckerman, 2021; Sierra-Ausin et al., 2022). The value of nt parametrises the accuracy of the spectral approximation, with convergence guaranteed for increasing

nt provided the time dependence is smooth enough. When the periodic orbit is simple enough, for instance close to a bifurcation point, a small number of harmonics may be enough to describe it accurately, whereas for more complex periodic dynamics more harmonics will be required.

Once the finite Fourier decomposition (4.3) is introduced into the Navier-Stokes equation (2.1 – 2.4) as an ansatz for \mathbf{u} and p , a set of nonlinear equations arises : one equation for each of the steady fields \mathbf{U} , P and the others for each Fourier component \mathbf{u}_k , p_k with $1 \leq k \leq nt$. This set of nonlinear equations can be solved using a Newton method to determine the fields \mathbf{U} , P , \mathbf{u}_k , p_k for all k and the unknown angular frequency ω . A temporal phase condition is added to the list of equations to make the Newton system well-posed. Indeed, the orbit is defined up to a phase shift. Different types of phase conditions can be imposed. For example, a value or a derivative of a variable is fixed at a specific point along the orbit. Imposing a derivative to zero for an arbitrary variable is generally a good choice and avoids requiring the knowledge of a specific value. Other phase conditions, less straightforward to implement, such as an integral phase condition can be imposed and is often favored when solving ordinary differential equations (see chapter 7 in Seydel (2009)). Here, as a phase condition, the time derivative of the radial velocity is fixed to zero at the beginning of the orbit and at one point in the domain. The Newton algorithm is converged to machine precision (i.e. when the Euclidean norm of the residual vector of the Newton method drops to 10^{-11} or less). Importantly, the decomposition (4.3) for $nt = 1$ is the decomposition used in the original SCM in Ref. Mantić-Lugo et al. (2014) at convergence. Thus, SCM and HBM for $nt = 1$ differ only in the iterative process of convergence of the solution. Once one solution of the Navier-Stokes equations is converged using HBM it can be continued in parameter space using standard arclength continuation (Allgower and Georg, 2012).

4.1.3 Hopf branch

The branch of oscillatory solutions bifurcating at Re_c is labelled the Hopf branch. Solutions on this branch are assumed exactly periodic, i.e. of the form (4.3). When using only one oscillatory mode this form reduces to (4.1). The coupled problem (4.2a)-(4.2b) is first solved for $A = 0$ and then for $A = 0.8$ ($Re = 2925.5 > Re_c = 2925.47$). The vector \mathbf{u}' in the forcing terms (4.2a) is selected in both cases as the most unstable eigenvector from Eq. (4.2b). Comparing the converged spectra for $A = 0$ and $A = 0.8$, the most unstable eigenvalue has moved towards the left upon increasing A (see Figure 4.1). Therefore, a value of $A = A^*$ such that \mathbf{U} becomes neutrally stable, i.e. $\lambda_r = 0$, presumably exists nearby. This value A^* is sought using the secant method. For the spatial resolution R0 this value is $A^* \approx 1.78$, as shown in Figure 4.1. This controlled SCM procedure has proven essential in catching the Hopf branch. The basin of attraction is small, hence for a given $Re > Re_c$, the amplitude A must be very close to A^* so as not to diverge.

Finding the neutrally stable field \mathbf{U} and the corresponding oscillatory field \mathbf{u}' yields one solution on the Hopf branch. Continuation in parameter space allows one to progress along the branch, which is displayed in Figure 4.2 using the time-average scalar observable a defined by (6.34).

The analysis of the Hopf branch leads to a few specific observations :

- A branch of periodic solutions is born at Re_c as expected
- at its onset the branch bifurcates towards $Re > Re_c$
- the amplitude of the oscillating solution scales like $\sqrt{Re - Re_c}$ near the bifurcation point.

The Hopf bifurcation occurring at $Re = Re_c$ is therefore supercritical, at odds with earlier expectations. While the approximation $nt = 1$ is valid close enough to Re_c , at a finite distance from it more temporal Fourier modes are needed, corresponding to $nt > 1$. A few observations can be made:

- The solutions for $nt = 1, 2$ and 3 collapse onto each other near Re_c but only in the very narrow range $0 < Re - Re_c < 10^{-4}$. This means that the strong assumption of the simple form of the limit cycle is valid only very close to Re_c for this flow.
- The $nt = 2$ and $nt = 3$ solutions collapse onto one another longer but diverge from one another when $\|\omega_{pert}\| \approx 0.5$. This means that the solutions on the Hopf branch becomes

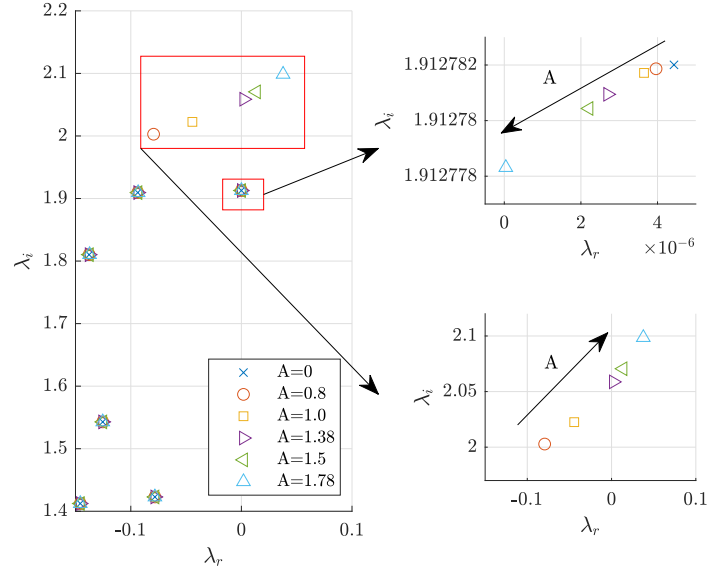


Figure 4.1: Application of self-consistent method (SCM) following Eq. 4.2. Spectrum evolution for $Re = 2925.5 \gtrsim Re_c = 2925.47$ with changing amplitude A of the forcing. When no forcing is applied ($A=0$) the base flow is unstable to a single eigenvector with the corresponding eigenvalue $\lambda = 4.4 \times 10^{-6} + 1.912782i$ (blue cross in inset). Top-right inset: eigenvalue evolution of the eigenvalue λ leading to the Hopf branch discussed in section 4.1.3. Each symbol marks the convergence of an inner loop process. The outer loop starts at $A = 0$ and converges for $A \approx 1.78$, when the resulting eigenvalue has a zero real part (only a few selected values of A are shown here). Bottom-right inset: evolution of another eigenvalue eventually leading to the discovery of a new branch as described in section 4.1.4. Spatial resolution R0.

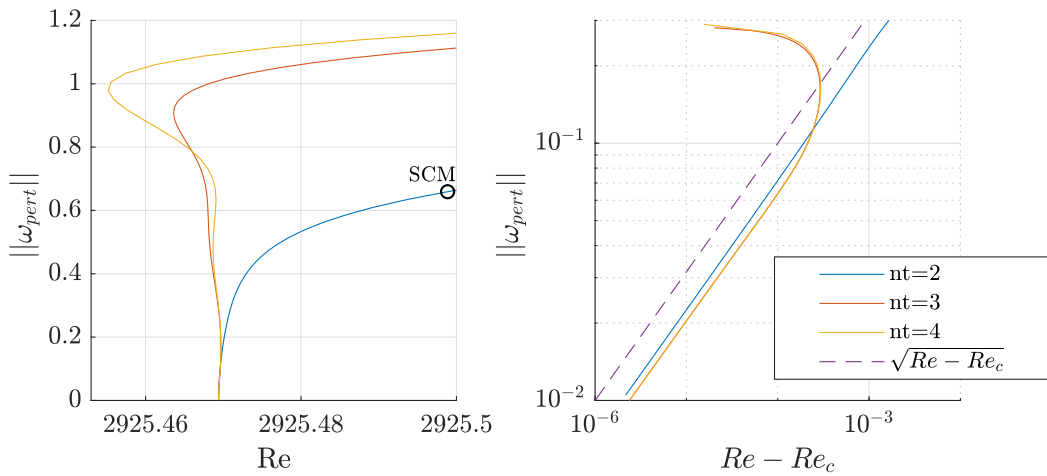


Figure 4.2: Left : onset of the Hopf branch for increasing parameter nt . The point at which the initialisation from the SCM solution to HBM solution is done is marked with a black circle. Right : zoom on the region $10^{-6} < Re - Re_c < 10^{-3}$ with $Re_c = 2925.47$, where the supercritical scaling $\alpha \propto \sqrt{Re - Re_c}$ (dashed line) holds (logarithmic scale). The color scheme is the same for both plots. Spatial resolution R0.

increasingly complicated away from Re_c . Generally, whenever the branches for subsequent nt stop overlapping they are considered temporally unresolved, and special care should be taken when interpreting the results.

- The Hopf branch shoots up vertically from the bifurcation point. On one hand any approximation error introduced by a finite difference scheme in time would move Re_c and the branch in parameter space, on the other hand the vanishing growth rates imply large integration times. This explains why they were not identified in Ref. Daube and Le Quéré (2002). Besides the strong non-normality of the linearised dynamics around the base flow (see section 3.5) carries over to the Hopf branch. The solutions on the Hopf branch are therefore believed to be virtually intractable using a time integrator. The link between strong non-normality and the steepness of the Hopf branch near criticality is discussed for instance in (Chomaz, 2005).

The whole SCM initialisation and HBM continuation procedure were repeated for the spatial resolution R2. The result appears to be qualitatively mesh-independent (not shown) and the finding of the bifurcation being supercritical is therefore robust. Recalling the expectation that a subcritical bifurcation at Re_c could explain the occurrence of concentric rolls at low enough $Re \ll Re_c$, the results can appear so far as disappointing. Not only is the Hopf branch supercritical, but the several folds that occur along the branch keep this branch limited to a relatively narrow $O(1)$ range in Re . Although further continuation past many folds could shed more light on this question, it appears safe to claim that the Hopf branch close to Re_c is probably not likely to explain the subcritical sustained states reported here and in (Daube and Le Quéré, 2002) at $Re \approx 2000$.

Interestingly, for $A = 1.38$ another eigenvalue, characterised by $\lambda_i > 2$, is close to becoming neutrally stable (see the purple triangle in the left most part of Figure 4.1). This means that, provided the eigenvector of the forcing in the equations (4.2) is changed to that eigenvector, SCM can again be used as an initial guess to uncover another new branch of periodic solutions. This process is described in the following section.

4.1.4 Periodic-subcritical branch

We describe here how a new branch of periodic solutions, different from the Hopf branch, was identified numerically as a by-product of the search for the Hopf branch. As the choice of the eigenvector \mathbf{u}' (resp. \mathbf{u}'^*) used in Eq. 4.2(a) is after all arbitrary, it can be traded for any other eigensolution $\tilde{\mathbf{u}}'$ (resp. $\tilde{\mathbf{u}}'^*$) of Eq. 4.2(b). $\tilde{\mathbf{u}}'$ is associated with an eigenvalue of imaginary part $\lambda_i \approx 2.05$ rather than the previous eigenvalue $\lambda_i \approx 1.91$. The substitution $\mathbf{u}' \leftarrow \tilde{\mathbf{u}}'$ was performed at the end of the outer iteration that resulted in $A = 1.38$. The eigenvector $\tilde{\mathbf{u}}'$ chosen, associated with an amplitude denoted \tilde{A} , was indeed close to neutral during the resolution of Eq. 4.2(a) with $A = 1.38$ (see Figure 4.1), which makes it an alternative interesting guess for SCM. After the substitution, the mean flow is no longer neutrally stable, but the SCM inner and outer iterations can resume. During this second process we observe a substantial increase in λ_i from ≈ 2.05 to ≈ 2.3 . At convergence the new amplitude $\tilde{A} \approx 1.48$. The first and the last step of the secant method (the outer loop) are illustrated in Figure 4.3.

When SCM is sufficiently converged, the solution is used to initialise HBM. HBM is used to converge the solution, which is then continued in parameter space (see Figure 4.4).

The above methodology yields a branch very different from the Hopf branch. This branch extends down to $Re \approx 1700$, i.e. much lower than both Re_c and the Hopf branch altogether. The newly found branch is hence called the *periodic-subcritical branch*. Precise values of Re at which this saddle-node bifurcation happens, Re_{SN} , are documented in Table 4.1. Its lower part also extends towards values of $Re \gg Re_c$, at least up to 7000 for both grid resolutions (not shown). This branch was therefore *not* found to bifurcate from the steady state in the range of Re investigated. The angular frequencies of the solutions on this branch are reported in Table 4.2.

Since the periodic-subcritical branch exists over a wider range of Re values than the Hopf branch, the corresponding solutions are studied in more detail. In particular a solution from the lower branch is visualised in Figure 4.5 for $Re = 2300$. It takes the form of rolls in the Bödewadt layer visually comparable to the most unstable eigenvector for the $Re \approx Re_c$. The decomposition in Eqs. (4.3), used in the Newton method, allows for a direct analysis of the temporal harmonics of this

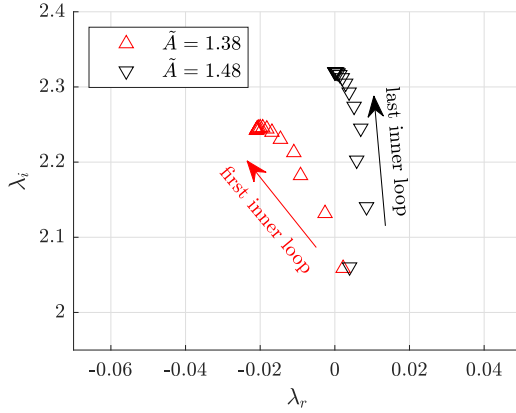


Figure 4.3: Determination of the periodic-subcritical branch using SCM. At $A = 1.38$ the eigenvector \mathbf{u}' was changed to another eigenvector $\tilde{\mathbf{u}'}$ (see text) with an amplitude denoted as \tilde{A} . \tilde{A} is set to 1.38 for the first inner loop. The red triangles show the convergence of the inner loop for $\tilde{A} = 1.38$ with the final $\lambda_r \neq 0$. After achieving convergence on \tilde{A} the last inner loop is shown using black triangles for $\tilde{A} = 1.48$ with the final $\lambda_r \approx 0$ and corresponding $\lambda_i \approx 2.33$. This convergence process on \tilde{A} takes approximately 10 iterations. For the sake of clarity only the first and the last inner loops are shown.

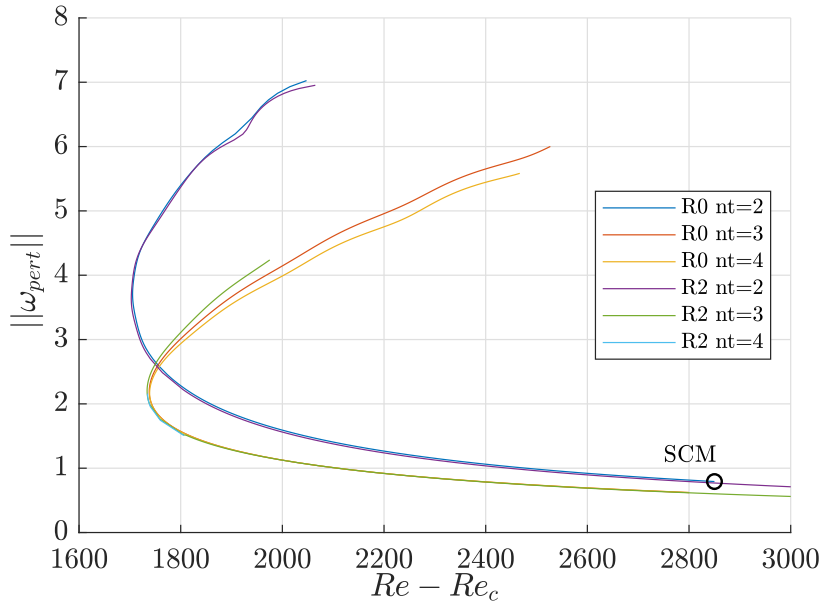


Figure 4.4: Periodic-subcritical branch for discretisations R0 and R2 and increasing nt , where nt is the number of Fourier modes in the decomposition (4.3). The point at which the initialisation from the SCM solution to HBM solution is done is marked with a black circle. Branches fold around $Re = Re_{SN} \approx 1700$. The exact saddle-node bifurcation values are listed in Table 4.1.

nt	1	2	3
R0	1705.3	1738.1	1738.9
R2	1702.8	1733.9	1734.7

Table 4.1: Saddle-node value Re_{SN} depending on the spatial and temporal discretisation.

Re	1900	1800	1734.7	2000	2300	2600	3000
$\omega_{per-sub}$	3.934	3.586	3.136		2.559	2.421	2.351
f	0.626	0.570	0.499		0.407	0.385	0.374

Table 4.2: Angular frequency of the periodic solutions on the periodic-subcritical branch shown in Figure 4.4. The point corresponding to the saddle node bifurcation is emphasised in bold. Re to the left (right) of this point correspond to the top (bottom) part of the periodic-subcritical branch in Figure 4.4. $\omega_{per-sub}$ corresponds directly to the angular frequency used in formula (4.3). Resolution R2, $nt = 3$.

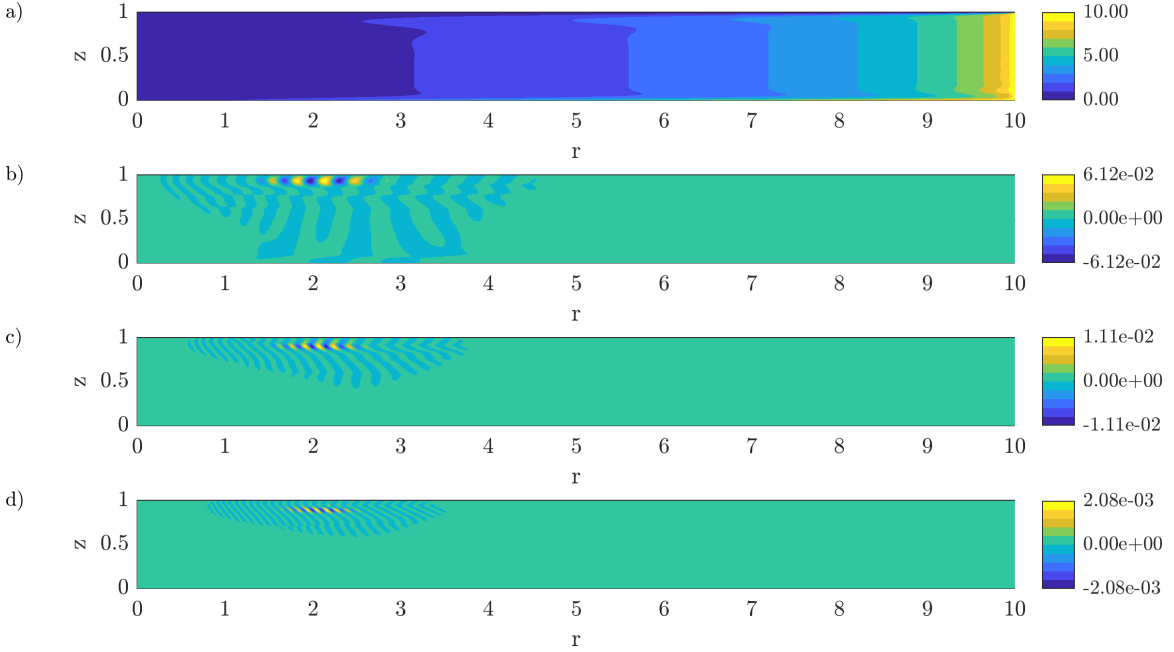


Figure 4.5: a) Contours of U_θ . b-d) u_θ for temporal harmonics $k = 1, 2, 3$ (from top to bottom) for the lower periodic-subcritical solution at $Re = 2300$. Spatial resolution R0, $nt = 3$.

solution. Subsequent oscillation modes are characterised by increasingly smaller structures. Any improvement in the temporal resolution nt must hence be accompanied by an increase in spatial resolution ($N_r \times N_z$).

4.2 Edge states

In this section, we focus on another type of finite-amplitude solution likely to contribute to the bifurcation diagram of the system. The third branch of solutions reported in the present work is a branch of *edge states*. As we shall see, their dynamics is more complex than that of the periodic states of section 4.1. They are known to play a major role as mediators between the base flow and the chaotic state (Khakpo et al., 2016), here the chaotic rolls.

4.2.1 Notion of edge state

Edge states are unstable finite-amplitude states, generally associated with low levels of perturbation energy, that are specific to the subcritical regime where the base flow is linearly stable. They have the defining property that their instability leads both to the chaotic solutions or to the base flow, depending on the perturbation considered (Skufca et al., 2006). Mathematically, in the state space associated with Eq. (2.1 – 2.4), edge states are local attractors belonging to the intersection of the respective attraction basins of attraction of the base flow and of the chaotic set. They exist as soon as the base flow has a non-trivial basin of attraction, i.e. in subcritical conditions, here for $Re < Re_c$.

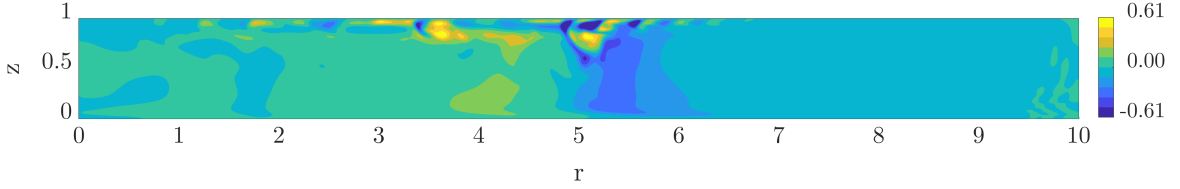


Figure 4.6: Instantaneous azimuthal velocity perturbation for chaotic rolls. $Re = 3000$. Spatial resolution R0.

The intersection of the boundaries of these basins of attraction is the stable manifold of the edge state, sometimes called simply the *edge*. The first computation of edge tracking in fluid flows is due to Itano and Toh (2001) in channel flow. Later computations have shown that edge states are generally spatially localised structures (Duguet et al., 2009; Khapko et al., 2016). Importantly, the dynamical nature of an edge state is not known in advance, it can be a steady state, a periodic orbit, or a more complicated object such as a chaotic set (Wang et al., 2007; Duguet et al., 2008b; Khapko et al., 2014). More details on the concept of edge state can be found in (Skufca et al., 2006; Schneider et al., 2007; Duguet et al., 2008b, 2009; Khapko et al., 2013). The technique is particularly useful when combined with symmetry subspace restrictions (Duguet et al., 2008b; Lopez et al., 2017). The aim of this section is to report, for the first time in the literature, calculations of edge states in rotor-stator flow for a set of Reynolds numbers.

4.2.2 Bisection algorithm

Following the above definition, the main idea behind the bisection algorithm is to find two points bracketing the stable manifold sufficiently close, such that the associated trajectories approach transiently the edge state. Starting with two flow states, one labelled *turbulent* and the other *laminar*, a new initial condition is formed using the interpolation

$$\mathbf{u}(t=0) = (1-\alpha)\mathbf{u}_{\text{laminar}} + \alpha\mathbf{u}_{\text{turbulent}}, \quad 0 < \alpha < 1. \quad (4.4)$$

This linear combination of the laminar state $\mathbf{u}_{\text{laminar}}$ and a turbulent state $\mathbf{u}_{\text{turbulent}}$ is the new initial condition for time integration. $\mathbf{u}_{\text{laminar}}$ can be the base flow solution. A representative snapshot of the $\mathbf{u}_{\text{turbulent}}$ is shown in figure 4.6. Depending on whether this new initial condition evolves towards the turbulent or laminar state, the initial condition is labelled as turbulent or laminar for the next iteration. This yields a sequence of α values $\alpha_0, \alpha_1, \dots$. The process is repeated until the sequence of α_k 's has converged. After each iteration the bracketing interval is halved, therefore the value of α for which the simulation shadows the edge the longest is determined up to machine precision (taken to be $10^{-16} \approx 2^{-53}$) after approximately $|\log(10^{-16})/\log 2| \approx 53$ iterations. This apparent limitation of the bisection algorithm by finite machine precision can be easily overcome by a *restart procedure* (Skufca et al., 2006). By restarting the bisection from a later time it can run indefinitely and the edge state is reached asymptotically.

The same observable $a(t)$ defined in Eq. (6.34) is used to monitor edge trajectories and the bracketing trajectories. If $a(t \rightarrow \infty) = 0$ the trajectory has reached the laminar base flow.

4.2.3 Edge branch

The bisection procedure is now used to identify edge states in the rotor-stator flow. The time history of the observable $a(t)$, the vorticity perturbation norm, is reported for $Re = 2300 < Re_c$ in Figure 4.7. Some guiding values of the interpolation coefficient α are provided in the legend. Bisection successfully identifies a state that is unstable and lies, by definition, at the boundary of the basins of attraction of the chaotic and the laminar regime. The same bisection procedure is repeated from $Re \approx Re_c$ down to where bisection fails due to the apparent lack of chaotic attractor. A representative portion of the corresponding time series is displayed in Figure 4.8. The signal on the edge seems chaotic for $Re = 1850$, almost periodic for $Re = 2000$ and apparently bi-periodic for $Re > 2300$. We observe that the bisection algorithm detects also the unstable solution at $Re = 3000$ which is

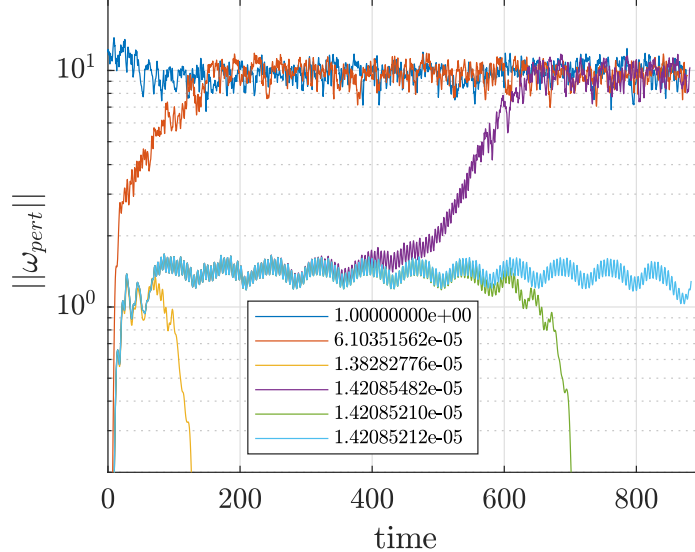


Figure 4.7: Time series of the observable $a(t)$ during the bisection procedure for $Re=2300$. Legend : coefficient α (defined in equation (4.7)) parametrizing the initial condition. Spatial resolution R_0 .

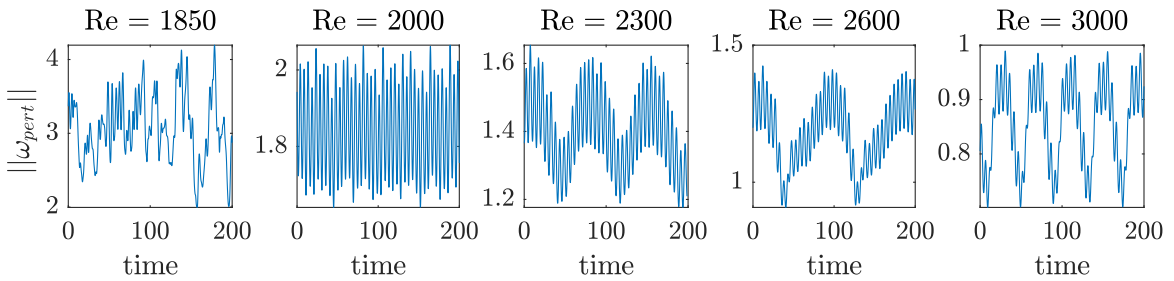


Figure 4.8: Perturbation vorticity signal $a(t)$ corresponding to the edge state, for the same values of Re . From left to right, $Re = 1850, 2000, 2300, 2600$ and $3000 > Re_c$.

only a few % above $Re_c = 2925.47$. Since $Re > Re_c$ this state is not formally an edge state because the laminar basin has collapsed to a single point. As demonstrated in Ref. Beneitez et al. (2020) using a low-order model, the edge state can still exist as finite-amplitude solution of Eq. (2.1 – 2.4) beyond Re_c although it loses its property of state space mediator. This collapse of the edge state makes it however, in principle, undetectable by standard bisection. Here the reason is simpler and due to the finite time over which the edge has been followed. Since the base state at $Re = 3000$ is only slightly unstable, it takes much more time for the unstable perturbation to the base flow to grow than it takes for the perturbation to the unstable edge state to grow. This explains why the bisection algorithm still detects an unstable solution near Re_c even for $Re \gtrsim Re_c$. The edge state found at $Re = 2300$ is chosen for further analysis because of its simple dynamics and its apparent bi-periodicity, an original property reported only lately in Refs. Lopez et al. (2017) and Bengana et al. (2019) in the context of lid-driven cavities.

4.2.4 Frequency analysis

A first glance at the observable time series for $Re = 2300$ suggests the presence of two main frequencies in the edge state: one corresponding to the long period $T \approx 75$, and one corresponding to a shorter period $T \approx 5$. For a first identification of the interesting frequencies the Fourier transformed of the *global* observable $a(t)$ is used. It is preferred to the velocity signal from a *local* probe because, as a global quantity, it gives an overview of *all* frequencies contributing to the edge state. A part of

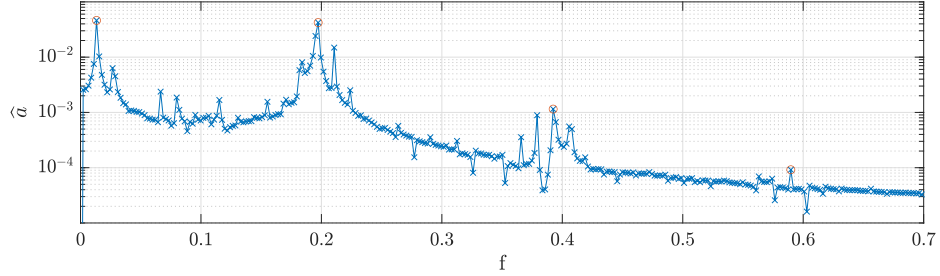


Figure 4.9: Frequency spectrum $\hat{a}(f)$ of the observable a . Spatial resolution R0. The spectrum is calculated using 2043 samples of the signal sampled uniformly in the time interval $t \in (300, 750)$. The maximum frequency computed is $f_{max} = 2.27$ with a frequency step $df = 0.0022$. The frequencies marked with red dots are listed in Table 4.3.

Frequency	0.013	0.197	0.392	0.590
Period	75.175	5.068	2.548	1.695

Table 4.3: Frequencies and periods of the main peaks from the frequency spectrum $\hat{a}(f)$ in Figure 4.9.

the signal corresponding to the final bisection iteration seen in Figure 4.7 is extracted and its frequency spectrum is computed. Care has been taken to disregard the initial and final transients of the signal. The remaining time interval available for the Fourier transform contains only approximately 6 long periods, hence finite-time effects should be expected to pollute the subsequent analysis. The frequency spectrum $\hat{a}(f)$ is plotted in Figure 4.9 as a function of the frequency f . A number of distinct discrete peaks can be observed. The frequencies marked with red circles are listed in increasing order in Table 4.3. The slow frequency ($f = 0.013$) in the spectrum corresponds to the long period seen in the observable signal ($T \approx 75$). A series of peaks corresponding to $f = 0.197, 0.392, 0.590$ correspond to the fast oscillations of a .

Further insight is gained by computing the Fourier transform of the (discrete) velocity field itself. For this purpose a series of flow fields is saved. A snapshot of the associated perturbation velocity is shown in Figure 4.10 together with a space-time diagram. The space-time diagram shows clearly the pairing and merging of the vortical structures as they propagate towards the axis inside the envelope (between $r = 1$ and $r \approx 3.5$). Interestingly, whereas we are now describing an edge state which by definition is unstable, the same pairing phenomenon has also been reported, for a smaller aspect ratio, as a feature of the propagation of the rolls observable experimentally (Schouveiler et al., 2001). A Fourier transform is computed at each point of the (discretised) domain using 2043 snapshots sampled uniformly over the time interval $t \in (0, 450)$. After bandpass filters around frequencies $f = 0.013, 0.197, 0.392$ and 0.590 are applied, the velocity field corresponding to each frequency is reconstructed in physical space. The azimuthal velocity components associated with each frequency are shown in Figure 4.11.

The velocity fields corresponding to higher frequencies ($f = 0.197, 0.392$ and 0.590 , Figure 4.11(b-d)) feature a wavetrain of counter-rotating vortices located inside the Bödewadt layer. These waves have negative radial phase velocity, i.e. they propagate in the direction of decreasing radius, as is clear from the spacetime diagram in Figure 4.12 (bottom). Interestingly, the waveform corresponding to $f = 0.392$ bears a high resemblance to the $k = 1$ mode of the periodic subcritical solution reported in section 4.1.4, particularly in Figure 4.5. For $Re = 2300$, the frequency of the periodic subcritical solution is $f_{per-sub} = 0.3854$, whereas the corresponding frequency for the edge state is $f_{FT} = 0.3924$.

The Fourier mode at the slow frequency ($f = 0.013$, Figure 4.11a) features vortical structures at the edge of the Bödewadt layer for $r \in (1, 3)$ and $z \in (0.8, 1)$. Using a space-time diagram computed for $z = 0.5$, an apparent wavepacket of nearly vanishing radial group and phase velocity is prominent for $r \in (1, 3)$ and $z \in (0, 0.8)$, see Figure 4.12 (top). Vertical structures exist also outside the Bödewadt layer. Consistently with the dispersion relation of inertial waves in flows with solid

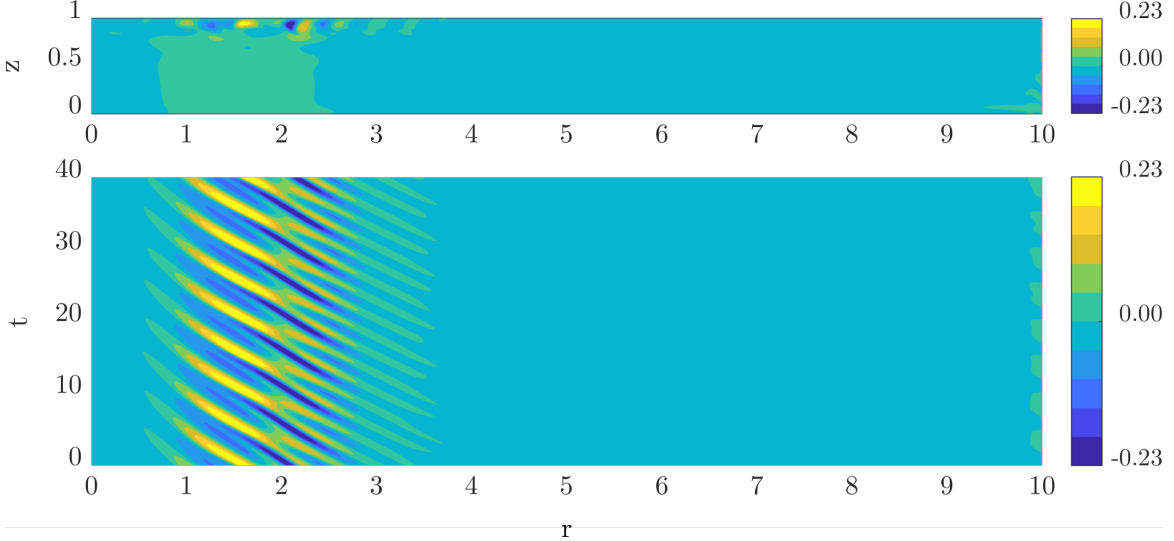


Figure 4.10: Top : Edge state snapshot of $u_\theta(r, z)$ in perturbation mode. Bottom : (r, t) space-time diagram of $u_\theta(r, z)$ at $z = 0.9375$ (bottom) for $Re = 2300$. Rolls are localised in the Bödewadt layer and travel towards the axis. Spatial resolution R0.

body rotation, such structures can be interpreted as low-frequency inertial waves. These slow waves, interpreted as spatially localised standing waves (with vanishing phase velocity), are also reminiscent of the internal waves observed inside the bulk of differentially heated cavities (Thorpe, 1968; Oteski et al., 2015).

As a yet stronger sign that the periodic and the edge solutions are connected, the Fourier mode extracted from the edge state corresponding to $f = 0.392$ is used as an initial guess for HBM with $nt = 2$. This is achieved in practice by building an initial guess for Newton's with (\mathbf{U}, P) as the mean solution, the edge mode corresponding to $f = 0.392$ as the first Fourier mode and the corresponding angular frequency. Convergence towards the formerly found periodic solution is obtained for $nt = 2$ in 15 Newton iterations. This indicates that the SCM method was *a posteriori* not the unique way to determine numerically the periodic-subcritical branch. The almost identical frequencies and waveforms suggest that the periodic-subcritical solution found in section 4.1.4 is itself an unstable solution embedded in a less unstable edge state. This situation happens to be common when edge states are chaotic (Duguet et al., 2008b), but deserves closer inspection here where the edge state is quasiperiodic in time. A simple possibility is that the edge state bifurcates, directly or indirectly, from the subcritical periodic branch. This is left for future investigation.

4.2.5 Quasiperiodicity of the edge state

In order to validate the hypothesis of a quasiperiodic edge state for $Re = 2300$, a velocity probe is considered where the rolls achieve large amplitudes in Figure 4.10. A state portrait based on the in-plane velocity components u_r and u_z is shown in Figure 4.13 (left). The plot on the right displays the Fourier transforms of $u_r(t)$ and $u_z(t)$. The Fourier transform displays clear distinct peaks over a non-zero background. It was checked, by artificially shortening the time series, that the background level is not the signature of a chaotic signal, instead it is due to the finiteness of the signal (which is an inherent limitation of the bisection technique). The main peaks correspond to the frequency $f_1 = 0.197$ and its harmonics, and to $f_2 = 0.013$ and its harmonics, consistent with the spectrum of $a(t)$ shown in Figure 4.9. The quadratic interplay of these two main frequencies explains the other frequencies $f = n f_1 \pm m f_2$ with $(n, m) \in (\mathbb{N} \times \mathbb{N})$ visible in the spectrum. Due to f_1 and f_2 being far apart in the discrete spectrum it is postulated the edge state of the studied rotor-stator flow at the $Re = 2300$ is indeed generically biperiodic with two incommensurate frequencies. In other words

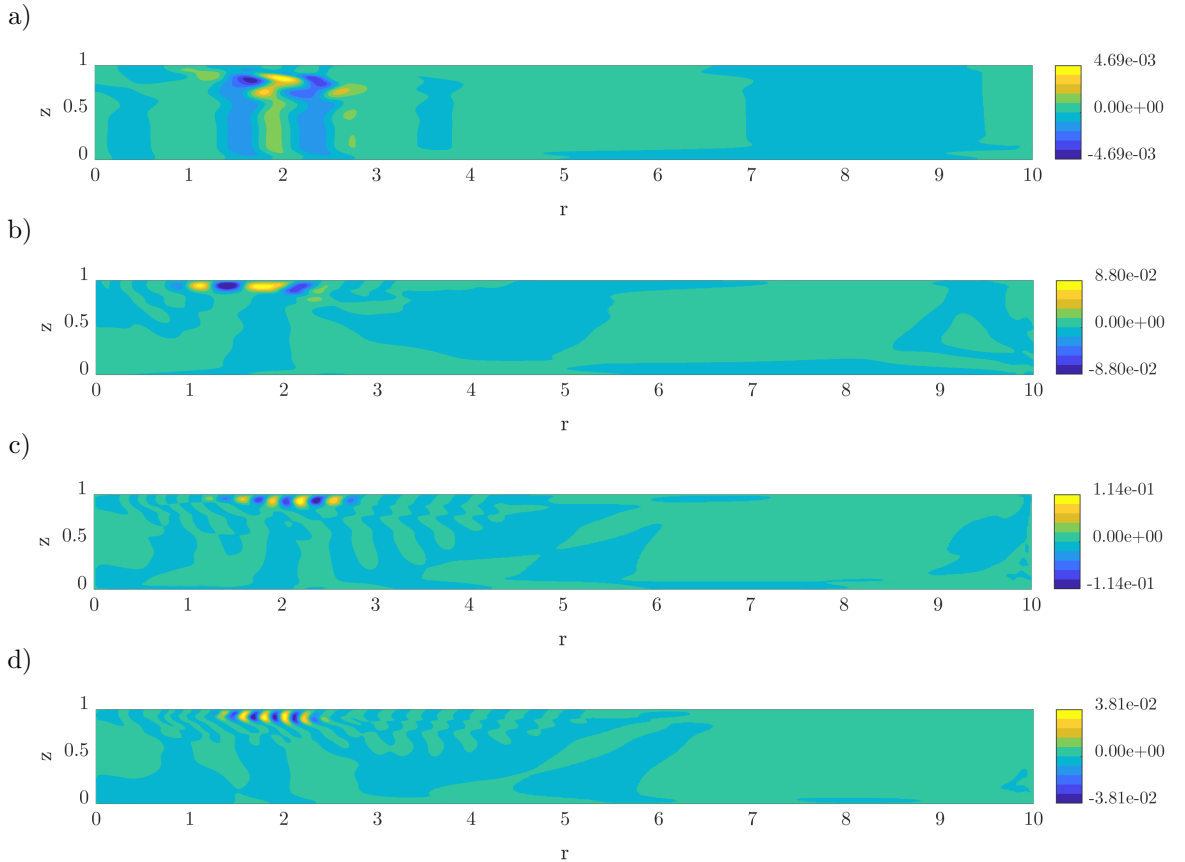


Figure 4.11: Temporal Fourier components of the edge state corresponding to frequencies a) $f = 0.013$, b) $f = 0.197$, c) $f = 0.392$ and d) $f = 0.590$, as shown in the spectrum in Figure 4.9. Note the resemblance between panel c) and the $k = 1$ harmonic in Figure 4.5.

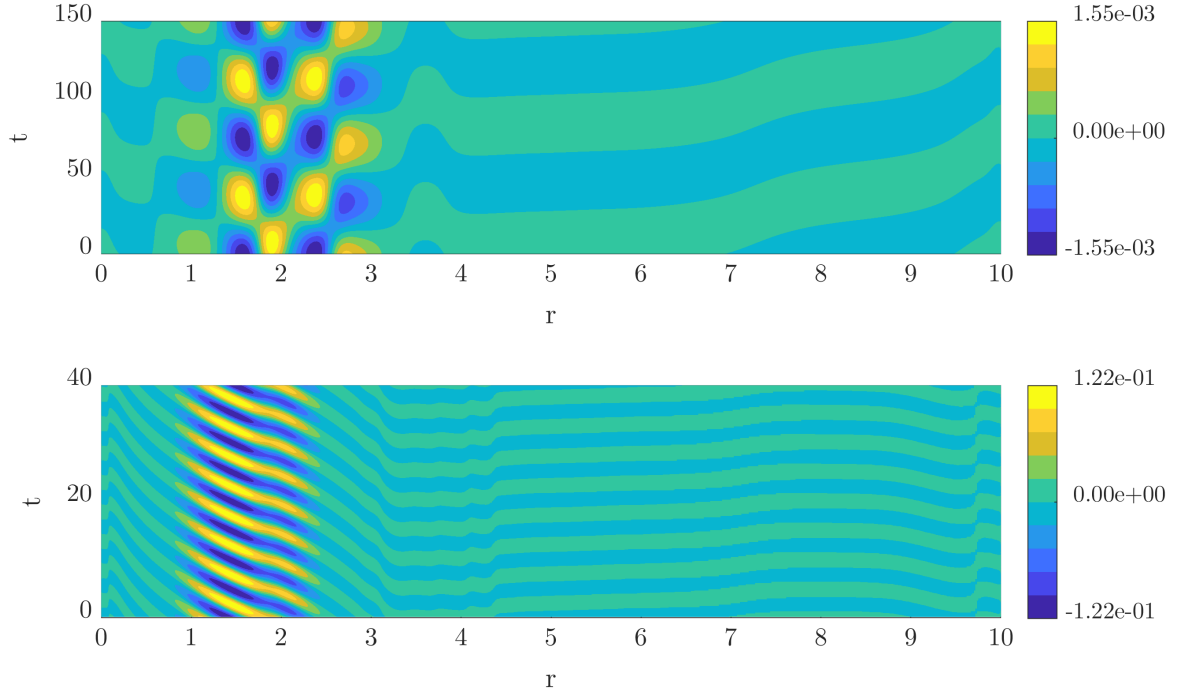


Figure 4.12: (r, t) space-time diagrams of selected temporal Fourier modes for the edge state at $Re=2300$. Spatial Resolution R0. Top: mode $f = 0.013$, $z = 0.5$ (mid-plane cut, compare with Figure 4.11 a), bottom: mode $f = 0.197$, $z = 0.9375$ (Bödewadt layer cut, as in Figure 4.11 b). The timescale and amplitude scale differ between the two figures.

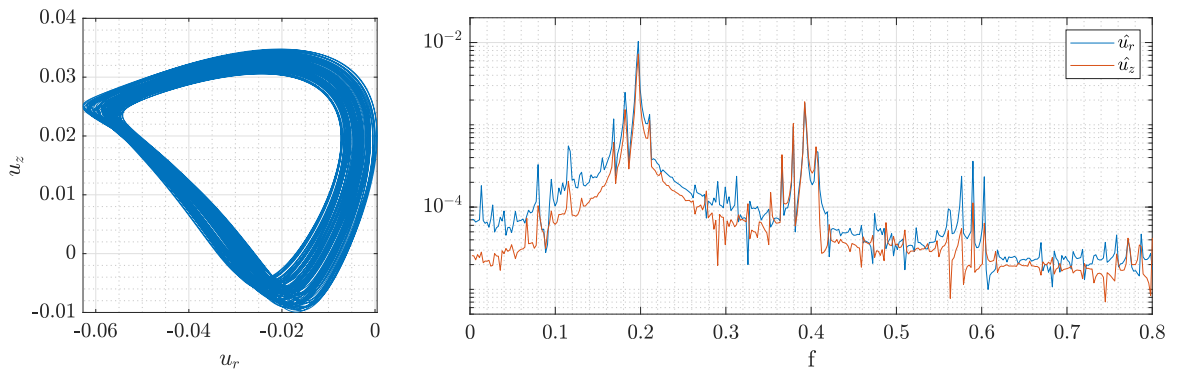


Figure 4.13: Velocity data at position $r = 1.0$, $z = 0.9375$ for the edge state at $Re = 2300$. Left : phase portrait using in-plane velocities u_r and u_z and the spectrum of probe signal. Right : Frequency spectrum computed using $\approx 100k$ samples spaced uniformly in $t \in (0, 450)$. Maximum frequency : $f_{max} = 113$ with a resolution $df = 0.0022$. Spatial resolution R0.

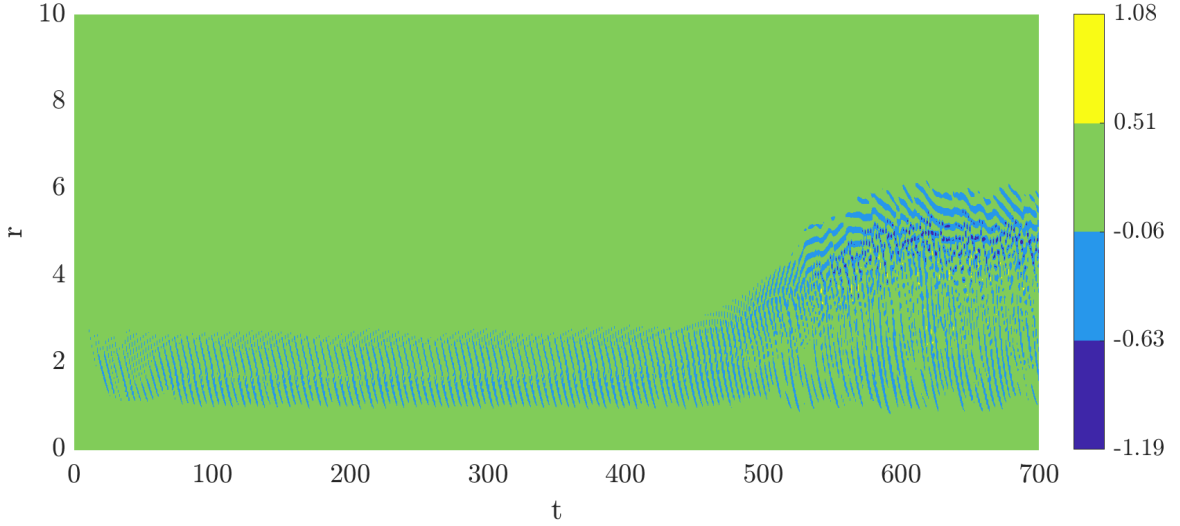


Figure 4.14: Instability of the edge state. (r, t) Space-time diagram for the perturbation $u_\theta(r, t)$ at $z = 0.9375$ for $Re = 2300$. The time series corresponds to one of the *non-converged* trajectories computed during the bisection process (corresponding to the value $\alpha = 1.42085482 \times 10^{-5}$, see Fig. 4.7). The departure of the edge state becomes evident for $t \geq 400$. The chaotic roll state is reached for $t \geq 600$.

it forms a 2-torus in the state space of Eq. (2.1 – 2.4). This property holds in the interval for most values of Re . No periodic edge state was identified for the Re studied.

4.2.6 Connection between the edge state and the chaotic rolls

By construction, the edge state is a linearly unstable solution of Eq. (2.1 – 2.4) with a specific property : typical perturbations lead, depending on their sign, either to the laminar base flow or to another chaotic state. We exploit this property and report now the dynamical path from the edge state to the attracting chaotic state Duguet et al. (2010). This is achieved simply by selecting and analysing one of the trajectories displayed in Fig. 4.7 for $Re = 2300$. A space-time diagram of the azimuthal velocity perturbation along the line $z = 0.9375$ is shown in Fig. 4.14. The dynamics follows closely the biperiodic dynamics of the edge state until $t \approx 400$. From $t \approx 400$ to $t \approx 600$, the perturbation to the base flow undergoes a rapid exponential growth in both energy and observable a (see Fig. 4.7). For $t \gtrsim 600$ the stationary chaotic state is reached, with no sign of convergence to any simpler flow state. During the exponential growth phase the radial extent of the edge state grows with time. Whereas the low- r end stays constant to ≈ 1 , the large- r of the localised structure moves upstream from $r \approx 2.5$ to $r \gtrsim 5$. This modification results both from an intensification of the perturbations convected away from the corner/shroud region, and from the advection of perturbations *against* the Bödewadt layer (the positive phase speed visible from $t \approx 500$ to $t \approx 600$). For $t \gtrsim 520$ the rolls originating upstream of the Bödewadt layer adopt a larger wavelength, a chaotic dynamics with no exact recurrence, and their radial phase speed is reduced (in absolute value) compared to the edge dynamics. Past $r \approx 4.5$ they decelerate towards the axis with a shorter wavelength and disappear for $r \leq 1.5$. The most energetic part of the stationary chaotic regime is found for $4 < r < 6$. This is the region where the bulk azimuthal profile departs most dramatically from the self-similar profile, and where ejections from the stator boundary layer occur.

4.2.7 Saddle-node bifurcation and mesh dependence

Figure 4.15 reports the time average of $a(t)$ for the solutions lying on the edge, together with the levels corresponding to the chaotic regime. The top (chaotic) branch and the edge branch approach each other for decreasing Re and visually suggest that they might connect for $Re \approx 1800$. By analogy with most subcritical shear flows (Schneider and Eckhardt, 2009), we speculate that the two branches

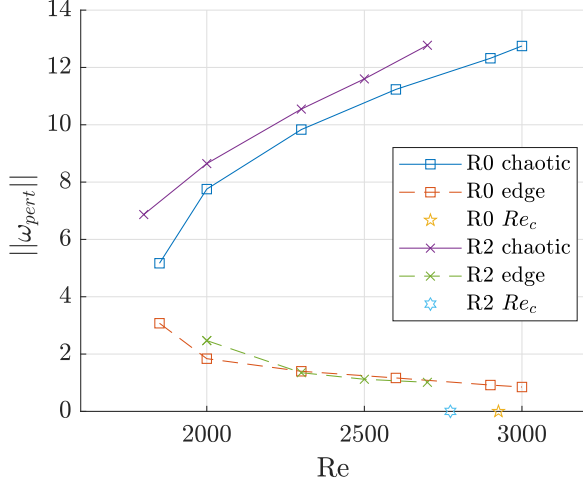


Figure 4.15: Bifurcation diagram $a(Re)$. Edge state branch and chaotic branch obtained using time integration. Spatial resolutions R0 and R2. The critical value of Re_c corresponding to each resolution is shown using stars.

merge in what could abusively be labelled as a saddle-node bifurcation at $Re = Re_{SN} \approx 1800$ (the fact that the top branch is chaotic makes the concept of saddle-node bifurcation somewhat undefined). Interestingly this value of Re_{SN} matches approximately the value reported in Table 4.1 at which the periodic subcritical branch folds back. This further highlights the connection between that branch and the edge branch.

The numerical edge tracking was conducted using the two different grid resolutions R0 and R2. By focusing again on the observable a , better spatial convergence is observed for the edge branch than for the top branch in Figure 4.15. This is a common observation in the shear flows: the edge state generally needs lower resolution than the corresponding turbulent solutions (Wang et al., 2007). Despite slight differences both branches can be claimed to be qualitatively well captured numerically.

Chapter 5

Noise sustained states and the response to the forcing

In this chapter quantitative scenarios for the circular rolls as a response of the system to external forcing are described. Two types of axisymmetric forcing are considered: bulk forcing (based on the resolvent analysis) and boundary forcing using direct numerical simulation. Using the singular value decomposition of the resolvent operator the optimal response is shown to take the form of circular rolls. The results for both types of forcing are compared with former experimental works and previous numerical studies. Additionally, the response of the flow in the nonlinear regime is characterised. For sufficiently high Reynolds number and strong enough forcing, the dynamics is attracted to the self sustained solutions present in the flow. The parameter range where supertransient dynamics are observed is also reported.

5.1 Linear response to forcing

5.1.1 Optimal response : theory

In this subsection the linear response of the flow to the forcing is analysed using optimal response theory. Following Cerqueira and Sipp (2014) we conduct the input/output analysis and show that the optimal response of the flow is for most relevant values of Re in the shape of circular rolls, and that associated with high levels of optimal gain. The nonlinear system of equations (2.1 – 2.4) can be linearised around the base flow when perturbation velocities are small enough. If a forcing field \mathbf{f} is introduced, the resulting system for the perturbation field (\mathbf{u}, p) can be rewritten

$$\frac{\partial \mathbf{u}}{\partial t} + (\mathbf{U}_b \cdot \nabla) \mathbf{u} + (\mathbf{u} \cdot \nabla) \mathbf{U}_b = -\nabla p + \frac{1}{Re} \nabla^2 \mathbf{u} + \mathbf{f}, \quad (5.1)$$

$$\nabla \cdot \mathbf{u} = 0. \quad (5.2)$$

The coupled system in (5.1)-(5.2) is linear in \mathbf{u} , p and also \mathbf{f} , which suggests to use the resolvent formalism. The theory by Trefethen and Embree (2005) forms the ideal framework except that the original linear system needs be rewritten in a form $\partial \mathbf{z} / \partial t = \mathbf{L} \mathbf{z} + \mathbf{f}_z(t)$, where the unknown field \mathbf{z} , a linear operator \mathbf{L} and a forcing $\mathbf{f}_z(t)$ need to be specified. We introduce the new variable $\mathbf{q} = (u_r, u_\theta, u_z, p)$ which contains the values of the fields u_r, u_θ, u_z and p at all the points of the discretised domain. The size of \mathbf{q} is $O(4N_r N_z)$. We also introduce the rectangular prolongation operator \mathbf{P} of size $O(4N_r N_z \times 3N_r N_z)$ which maps \mathbf{u} into \mathbf{q} , so that $\mathbf{P}^T \mathbf{q} = \mathbf{u}$ with the property $\mathbf{P}^T \mathbf{P} = \mathbf{I}$, see e.g. Jin et al. (2021). The linear system (5.1– 5.2) can then be rewritten into the new form

$$\mathbf{B} \frac{\partial \mathbf{q}}{\partial t} = \mathbf{A} \mathbf{q} + \mathbf{P} \mathbf{f}, \quad (5.3)$$

where $\mathbf{B} = \mathbf{P} \mathbf{P}^T$. After a Fourier transform in time, each Fourier component $\hat{\mathbf{q}}$ of \mathbf{q} satisfies

$$(i\omega \mathbf{B} - \mathbf{A}) \hat{\mathbf{q}} = \mathbf{P} \hat{\mathbf{f}}, \quad (5.4)$$

resulting in the Fourier components $\hat{\mathbf{u}}$ of the velocity field \mathbf{u} as the action of a matrix \mathbf{R} on the forcing $\hat{\mathbf{f}}$:

$$\mathbf{R}\hat{\mathbf{f}} = \hat{\mathbf{u}} \quad (5.5)$$

where

$$\mathbf{R} = \mathbf{P}^T (i\omega \mathbf{B} - \mathbf{A})^{-1} \mathbf{P} \quad (5.6)$$

is the resolvent operator associated with the (real) angular frequency ω .

An optimal gain can be evaluated by identifying an optimal forcing for a suitable norm of the resolvent \mathbf{R} . A positive symmetric linear operator $\mathbf{Q} \neq \mathbf{I}$, associated with the cylindrical coordinate system, can be used to define the inner product

$$\langle \mathbf{u}, \mathbf{v} \rangle_{\mathbf{Q}} = \mathbf{u}^* \mathbf{Q} \mathbf{v} = \int_0^1 \int_0^R (u_r^* v_r + u_\theta^* v_\theta + u_z^* v_z) r dr dz, \quad (5.7)$$

where the asterisk denotes complex conjugate. The associated vector norm is defined by

$$\|\mathbf{u}\|_{\mathbf{Q}} = \sqrt{\mathbf{u}^* \mathbf{Z}^T \mathbf{Z} \mathbf{u}} = \|\mathbf{Z} \mathbf{u}\|_2, \quad (5.8)$$

where $\mathbf{Q} = \mathbf{Z}^T \mathbf{Z}$. \mathbf{Q} can be also used to define the following norm for the resolvent operator

$$\|\mathbf{R}\|_{\mathbf{Q}} = \|\mathbf{Z} \mathbf{R} \mathbf{Z}^{-1}\|_2 = \sigma_1(\mathbf{Z} \mathbf{R} \mathbf{Z}^{-1}), \quad (5.9)$$

where σ_1 denotes the largest singular value in the SVD decomposition. Note that finding the largest singular value of $\mathbf{Z} \mathbf{R} \mathbf{Z}^{-1}$ is equivalent to finding the largest eigenvalue of the eigenvalue problem (Cerqueira and Sipp, 2014):

$$\mathbf{R}^* \mathbf{Q} \mathbf{R} \hat{\mathbf{f}} = \lambda \mathbf{Q} \hat{\mathbf{f}} \quad (5.10)$$

where

$$G = \lambda = \sigma_1^2 = \frac{\hat{\mathbf{u}}^* \mathbf{Q} \hat{\mathbf{u}}}{\hat{\mathbf{f}}^* \mathbf{Q} \hat{\mathbf{f}}} \quad (5.11)$$

is interpreted as the optimal energy gain.

5.1.2 Optimal response : results

For a range of angular frequencies ω the eigenvalue problem (5.10) is solved numerically in MATLAB with the *eigs()* function. The resulting eigenvalue $G = \sigma_1^2$ from Eq. 5.11 is plotted in figure 5.1 (left) as a function of the (real) angular frequency of the forcing. The optimal value σ_{max}^2 over all angular frequencies obtained for various values of Re are compared in figure 5.1(right), with the case $\omega = 0$ singled out. The optimal value of G gain over all ω 's, i.e. the optimal gain, is also listed in the table 5.1.2 together with the values obtained with different mesh resolutions.

For low $Re < 150$ the optimally amplified frequency is always $\omega = 0$. This corresponds to a steady forcing f in the equations (2.1 – 2.4). Forcing a given flow at $\omega = 0$ can be interpreted in different complementary ways. It can first be understood as the smooth $\omega \rightarrow 0$ limit of a given harmonic forcing at frequency ω . It can also be understood, in the unforced problem, as the steady streaming component associated with the nonlinear self-interaction of arbitrary oscillatory perturbations (see e.g. Mantić-Lugo et al. (2014)). In both cases the optimal response at $\omega = 0$ is interpreted as an optimal steady mean flow correction, which justifies the special focus on $\omega = 0$. As seen in figure 5.2 the most amplified steady forcing is always localised in the region near the axis. For $Re > 1800$ it inherits the characteristics of the base flow in the sense that it is composed of two boundary layers and invariant core in between.

For $Re \approx 150$ the optimally forced structures change radically as unsteady ($\omega \neq 0$) forcing takes over steady forcing. This is clearly seen in figure 5.1(right) where for $Re \gtrsim 150$ nonzero forcing frequencies ω start to dominate the optimal gain curve. The structure of the associated optimal forcing lies entirely within the Bödewadt layer, see figure 5.3 which focuses on $\omega \approx 1.7$ close to the

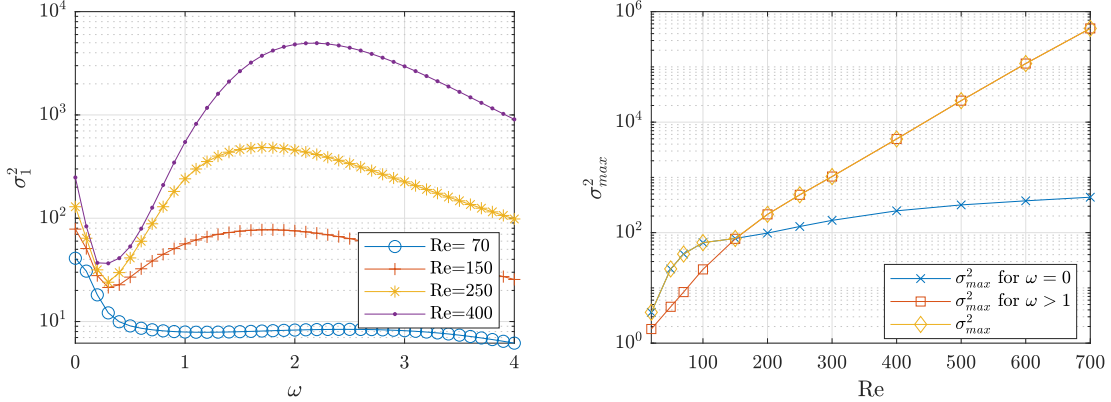


Figure 5.1: Optimal response for bulk-based forcing. Left: optimal energy gain as a function of forcing angular frequency ω , given by the largest singular value of the resolvent operator (5.6). Right: optimal gain across all ω 's as a function of Re . Numerical resolution D0.

Re	$\sigma_{max}^2(D0)$	$\sigma_{max}^2(R0)$	$\sigma_{max}^2(R2)$	$\sigma_{max}^2(R3)$	ω
20	3.61×10^0				0.0
50	2.20×10^1				0.0
70	4.10×10^1	4.10×10^1			0.0
100	6.59×10^1				0.0
150	7.85×10^1	7.86×10^1	7.87×10^1		0.0
200	2.14×10^2				1.6
250	4.84×10^2	4.94×10^2	4.90×10^2		1.7
300	1.04×10^3				1.9
400	4.95×10^3	5.50×10^3	5.47×10^3		2.2
500	2.45×10^4				2.4
600	1.15×10^5				2.6
700	4.97×10^5	7.62×10^5	7.96×10^5	8.38×10^5	2.9
1800		7.10×10^{11}	1.29×10^{12}	1.50×10^{12}	4.3
3000		2.08×10^{16}	1.28×10^{17}	1.66×10^{17}	5.4

Table 5.1: Optimal forcing gain. The last column shows the optimal angular frequency ω associated with the largest energy gain (the computations are performed with a step of 0.1 in angular frequency). Four mesh resolutions (see table 2.1) are used to find the optimal gain value. While for $Re \approx 250$ results can be considered as satisfactory for resolution R0, increased resolution is needed for larger Re . This is due to increasingly thin boundary layers required to resolve the optimal forcing mode.

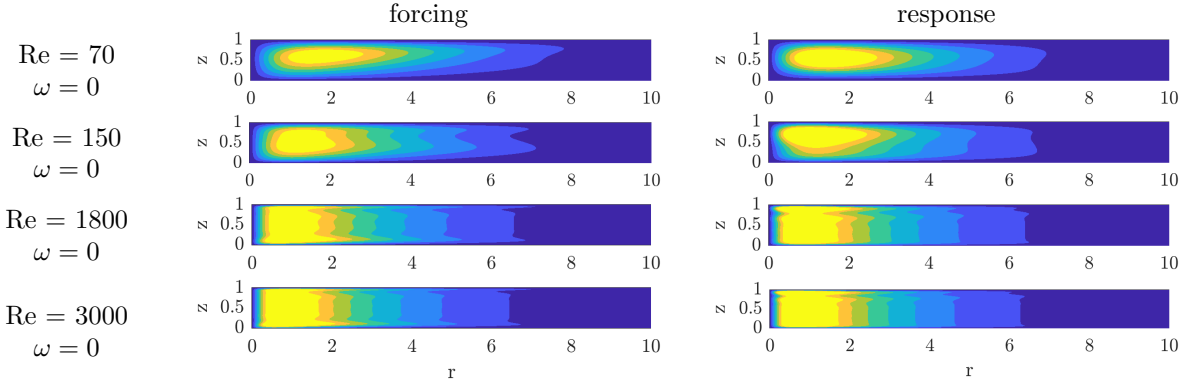


Figure 5.2: Azimuthal perturbation velocity $u_\theta(r, z)$ for optimal forcing and optimal response for vanishing forcing frequency $\omega = 0$. For $Re=70$ and 150 the optimal forcing at $\omega = 0$ is also optimal across all ω 's. The colormap spans 8 equal subintervals of $[0, 0.5]$. Both optimal forcing and response are normalised such that $\|\hat{\mathbf{f}}\|_{\mathbf{Q}} = \|\hat{\mathbf{u}}\|_{\mathbf{Q}} = 1$.

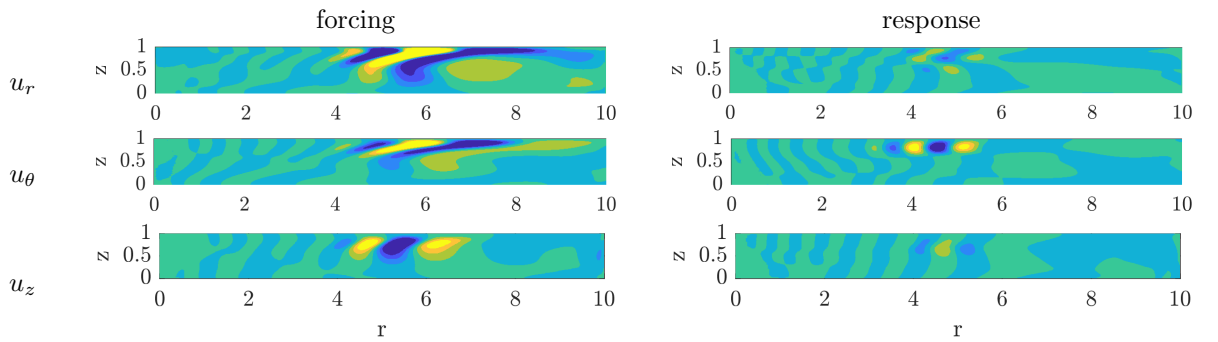


Figure 5.3: Optimal forcing and response for $Re=250$. From top to bottom : perturbation velocity components u_r , u_θ and u_z for the optimal angular frequency $\omega = 1.7$. The colormap spans 8 equal subintervals of $(-0.15, 0.15)$ for the optimal forcing, and $(-0.6, 0.6)$ for the optimal response plots. The optimal forcing and response are normalised such that $\|\hat{\mathbf{u}}\|_{\mathbf{Q}} = \|\hat{\mathbf{f}}\|_{\mathbf{Q}} = 1$.

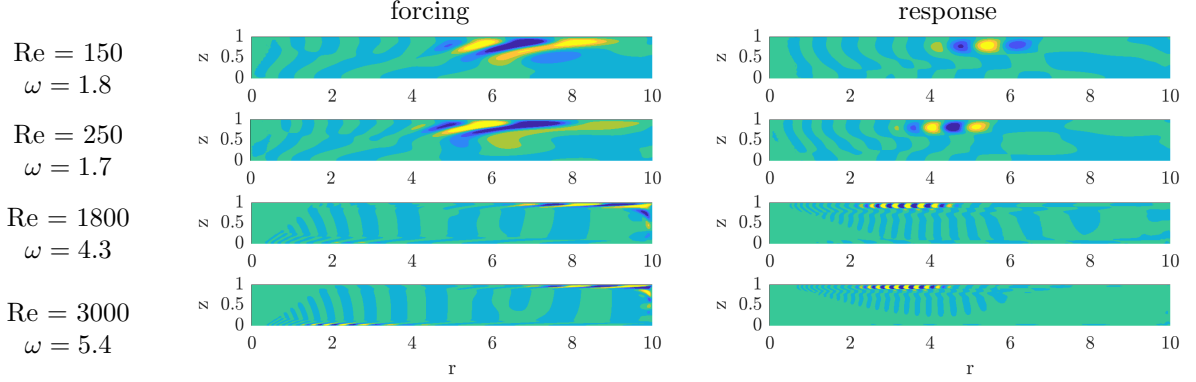


Figure 5.4: Azimuthal perturbation velocity $u_\theta(r, z)$ for the optimal forcing and response for $\omega \neq 0$. For $Re=250$, 1800 and 3000 the optimal forcing is also optimal across all ω 's. The colormap spans 8 equal subintervals of $(-0.15 \ 0.15)$ for the optimal forcing and $(-0.6 \ 0.6)$ for the optimal response.

optimal angular frequency (see Table 5.1.2). For all velocity components these structures are tilted by the mean shear into the streamwise direction. While the amplitude of optimal forcing is similar in the three spatial components the corresponding optimal response may differ from component to component (Jovanović and Bamieh, 2005), and in the present geometry it is clearly dominated by the azimuthal component. The signature of the circular rolls can be also seen in the azimuthal response although the corresponding structures should more realistically be labelled as azimuthal streaks. Their position ($r \approx 4 - 6$) and the corresponding Re are perfectly consistent with experimental observations. Most importantly, and this constitutes one of the main findings of the current work, the optimal response is in the shape of circular rolls in the Bödewadt layer.

The evolution of the optimally forced structure is now described as Re increases beyond 250. It is first noted that, as shown in figure 5.1 (right), the optimal gain $G_{opt}(Re)$ grows exponentially with Re . We note that the experimental study of Gauthier et al. (1999), performed for $\Gamma \approx 20$, has suggested a supercritical bifurcation as the origin of the observed rolls. Our observations do not corroborate this hypothesis since the angular frequency content of the response features that a continuum of frequencies can be excited externally, at odds with the dominant frequency stemming from a Hopf bifurcation. Moreover, the steep exponential increase of $G(Re)$ reported above might be responsible, in experimental conditions where external forcing stays uncontrolled, for the apparent bifurcating behaviour where the amplitude of the response increases rapidly with Re . As Re continues to increase, as shown in figure 5.4 the optimal forcing evolves with Re from a wide support within the Bödewadt layer to thinner structures in both the Bödewadt and the shrouding wall, and even for $Re = 3000$ also in the Ekman layer. For such high Re values the respective supports of the forcing and the response are almost disjoint.

The results above unambiguously point towards an unsteady response in the shape of circular rolls for all $Re \gtrsim 150$. We emphasize that the crossing of the gain curves for $\omega = 0$ and $\neq 0$ in figure 5.1(right) does *not* define a threshold value for Re because, as for any linear receptivity mechanism, the response depends linearly on the spectral content of the forcing history. Defining a threshold value for Re is demanding because it is highly dependent on the amplitude levels that an experimentalist can detect in practice. By focusing on the value of the optimal gain ($G = 4.9 \times 10^2$) at $Re = 250$ the following hand-wavy evaluation can be made. Any parasite vibration present in the experiment projected on the orthogonal basis of the optimal modes will have a nonzero component that will be optimally forced. If the amplitude of this component is, say, of order $O(10^{-2})$ it will be amplified by the linear mechanism by $\sqrt{G} \approx 20$ to yield an $O(10^{-1})$ response, which can be detected in experiments.

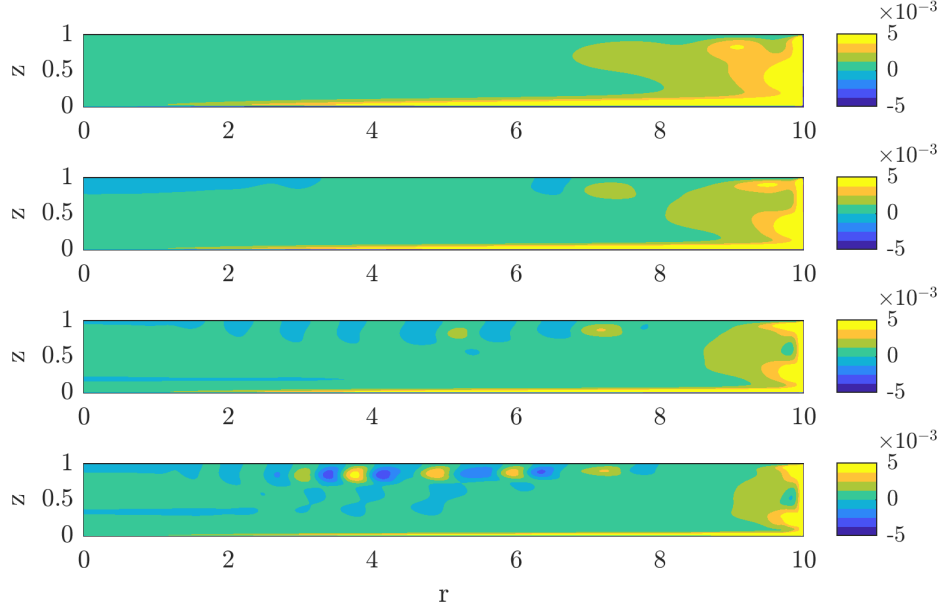


Figure 5.5: Nonlinear time integration in the presence of white noise forcing at the $z = 0$ and $r = \Gamma$ boundary with amplitude $A = 10^{-2}$. Snapshots of the azimuthal perturbation velocity $u_\theta(r, z)$. From top to bottom: $Re = 70, 150, 250, 400$. A wavetrain of circular rolls is seen for $Re > 250$.

5.1.3 Boundary forcing

While the previous section offers an elegant formal manner to explain the circular rolls from (linear) optimality arguments, we note that at the experimentally relevant values of Re , the optimal forcing protocol corresponds to a force field that needs to be applied to the flow *away* from the solid boundaries. Set-up imperfections are expected to induce forcing *at* the boundaries rather than away from them. For this reason, it is unlikely that the observed linear response corresponds to truly optimal forcing, and it might be more relevant to concentrate on sub-optimal forcing. Instead, we consider a forcing protocol which without being energetically optimal affects directly the flow through unsteady motion of the boundaries (and is hence not a suboptimal from the previous bulk-based optimisation). Modulations of the instantaneous (dimensional) angular velocity are considered in the form $\Omega(t) = \Omega_0(1 + A \varepsilon(t))$, where $\varepsilon(t)$ represents a normalised unsteady forcing and $A \geq 0$ is a measure of its amplitude. This is similar to Lopez et al. (2009), Poncet et al. (2009) and Do et al. (2010), except that $\varepsilon(t)$ is not monochromatic. The Reynolds number, now based on Ω_0 rather than Ω (which depends on time), remains by definition unaffected by the value of A .

Time integration

The time modulation is simulated in practice by updating, at the end of each timestep after the prediction-projection step, the value of v_θ imposed on the shroud and the rotor as

$$v_\theta(r, t) = r(1 + A \varepsilon(t)) \quad (5.12)$$

The modulation $\varepsilon(t)$ can be chosen in many ways. For most of this study, it is chosen as a Gaussian white noise of zero mean and standard deviation 1. A , which multiplies the white noise signal, is therefore the root mean square (rms) value of the forcing. All simulations are initiated with a zero perturbation field.

Figure 5.5 shows representative azimuthal velocity snapshots obtained from nonlinear time integration of the forced flow. As will be clear later in section 5.3, for the aspect ratio $\Gamma = 10$ and $Re < 300$ nonlinearity plays a negligible role and the observations are independent of whether the time integration is linear or nonlinear. This is why those results are discussed in the context of linearly optimal results. The response to the unsteady white noise forcing is localised, for low $Re \approx 70$, next to the rotor and the shroud. For $Re \gtrsim 150$ and beyond, wavetrains of increasingly smaller

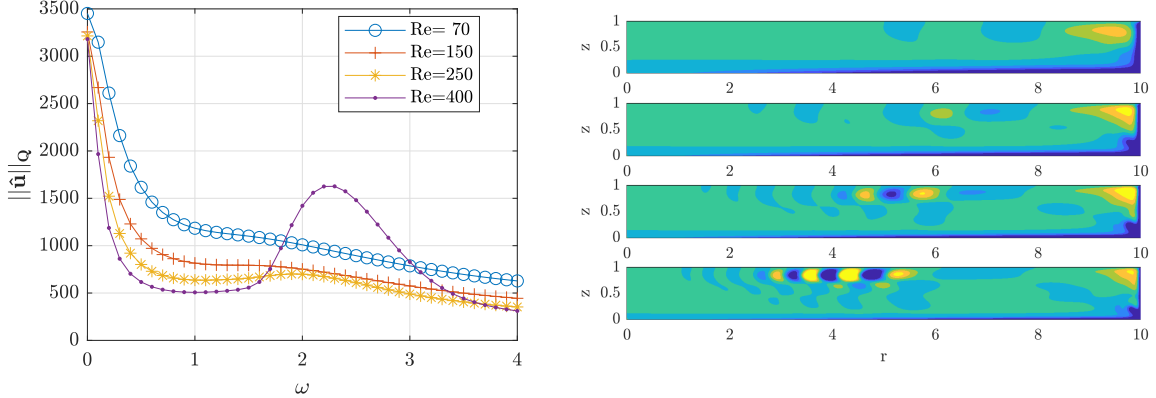


Figure 5.6: Response to the boundary forcing obtained by the resolvent approach in section 5.1.3. Left: \mathbf{Q} -norm (squared) of the velocity response. Right, from top to bottom: real part of $\hat{u}_\theta(r, z)$ for $\omega = 2$ for $Re = 70, 150, 250, 400$. The $\hat{\mathbf{u}}$ response is normalised so that $\|\hat{\mathbf{u}}\|_{\mathbf{Q}} = 1$. Colormap spans $-0.3, (0.075), 0.3$.

circular rolls form inside the Bödewadt layer, as is visible for $Re = 250$ and $Re = 400$.

Interestingly, the response to boundary forcing is similar to the response to the optimal forcing in the sense that the response consists also of wavetrains of circular rolls located inside the Bödewadt layer. Due to the wide frequency content this response is however more widespread than in the case of optimal forcing (e.g. for $Re = 250$ the wavetrain is detected for $r \in (2, 7)$). A pronounced response near the rotor and especially the shroud is also seen, as a signature of the imposed forcing.

Resolvent approach to boundary forcing

The connection between the linearised time integration and the resolvent approach from (5.4) is the Fourier transform of the linearised governing equations. Selecting the additive forcing term $\hat{\mathbf{f}}$ corresponding to the forcing protocol of (5.12), and then solving (5.5) for $\hat{\mathbf{u}}$ will therefore yield directly the Fourier transform of the response. It can be in turn compared against the Fourier transform of the probe signals extracted from linearised time integration. The same analogy has been exploited by Cerqueira and Sipp (2014) in order to validate their input/output analysis. In our case, beyond immediate validation, this comparison is useful as it draws a link between boundary forcing (although based on linear time integration rather than the nonlinear integration allowing for spectral mixing) and the inherently bulk-based resolvent approach.

We therefore select a specific, non-optimal forcing term $\mathbf{P}\hat{\mathbf{f}}$ corresponding to the Fourier transform of the boundary forcing (5.12). Solving (5.4) with prescribed $\mathbf{P}\hat{\mathbf{f}}$ yields $\mathbf{P}\hat{\mathbf{u}}$, the real part of which is plotted in figure 5.6. The (squared) \mathbf{Q} -norm of $\hat{\mathbf{u}}$ is shown in the same figure. Due to the forcing being suboptimal, its dependence on ω differs from the gain curve in figure 5.1 (left). Again, starting with $Re = 250$ a hump visible in figure 5.6(left) around $\omega = 2$ marks the preferred response of the flow in the shape of rolls.

More insight into the preferred response frequencies of the flow is possible through the analysis of the probe signals extracted from linear time integration. The raw signals, corresponding to four radial positions $r = 1, 3, 5, 7$ along the Bödewadt layer, are shown in figure 5.7(left). The forcing is again white in time with equal amplitude for each frequency. The Fourier transform of the probe signal confirms, as already visible from the fields in figure 5.5 and 5.6, that the strength of the response to boundary forcing depends on the radial position. The radially inwards flow in the Bödewadt layer suggests that the distance to the shrouding wall, and therefore the varying thickness of the boundary layer, are the physically meaningful variables to explain this dependency, as also suggested by Gauthier et al. (1999) (we will however stick to the variable r for commodity). The preferred

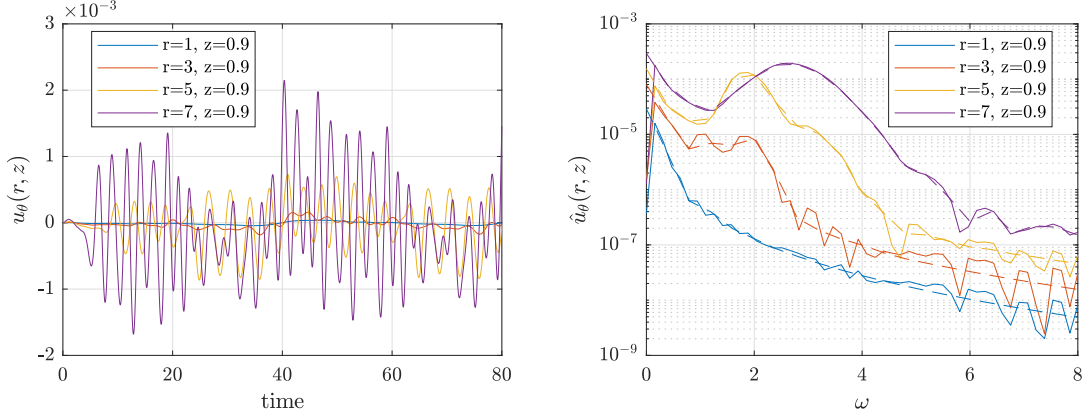


Figure 5.7: Response to boundary forcing by Gaussian white noise with $A = 10^{-2}$, $Re=200$. Left: time series of perturbation velocity u_θ obtained from time integration for different probes at varying r inside the Bödewadt layer $z=0.9$. Right: comparison between the time integration and the resolvent approach to boundary forcing in frequency space. Fourier amplitude spectrum of these time series (solid lines) versus $|\hat{u}_\theta|$ associated with boundary forcing, computed from resolvent analysis (dashed lines) and evaluated at the same spatial positions. Numerical parameters $dt = 4 \cdot 10^{-3}$, $nt = 20\,000$, $d\omega = 0.157$, $\omega_{Nyquist} = 785$ corresponding to the timestep, number of timesteps, sampling angular frequency and Nyquist angular frequency respectively. Only the later half of the signal was used for the calculation of the Fourier transform ($40 < t < 80$).

response frequency evolves also with the radial position. It is close to $\omega = 0$ for the probe at $r = 1$, but close to $\omega = 3$ for the probe $r = 7$. The Fourier amplitude can be directly compared to the pointwise amplitude of $\hat{\mathbf{u}}$, as mentioned earlier. The convincing overlap of both data (see figure 5.7(right)) demonstrates the equivalence between the linear time integration and the direct resolvent solve based on (5.5).

5.1.4 Computation of the pseudospectrum

A fundamental tool in the analysis of non-normal systems is the pseudospectrum, which is a generalisation of the concept of (eigen)spectrum. Recall that the spectrum of the linearised system $\dot{\mathbf{u}} = \mathbf{L}\mathbf{u}$ is the (complex) set of eigenvalues of the associated linear operator. If a complex number ω belongs to the spectrum σ , the resolvent $(i\omega\mathbf{I} - \mathbf{L})^{-1}$ (or expressed in the present case by (5.6)) is undefined, whereas it is continuous and smooth as a function of ω in the immediate neighbourhood of its pole at $i\omega$. Following Trefethen and Embree (2005) the ε -pseudospectrum σ_ε is defined as the complex set where the norm of the resolvent operator exceeds a given value ε^{-1} , with ε a potentially small real number :

$$\sigma_\varepsilon = \{\omega \in \mathbb{C}, \|\mathbf{R}\|_{\mathbf{Q}} > \varepsilon^{-1}\} \quad (5.13)$$

It includes the point spectrum and can be seen as its generalisation. In the current work, it is mainly used as an indicator of the strong non-normality of the underlying linearized operator. Owing to the definition 5.13, the cut of the pseudospectrum through the real axis directly yields the gain curves plotted in figure 5.1. The pseudospectrum is computed in each point, analogously to the optimal gains described in section 5.1.1, except that ω is allowed to be complex. Note that such computations rely on the shift-and-invert algorithm itself dependent on a complex shift parameter s . Contours of the pseudospectrum are reported in figure 5.8. As expected for a strongly non-normal operator, the isocontours of σ_ε do not form concentric circles around the eigenvalues yet the contours encircle more than one eigenvalue. Still, very close locally to a given eigenvalue, the isocontours found for $Re = 200$ form closed loops around specific eigenvalues, as can be seen in the top right panel in figure 5.8. Upon increasing Re , the non-normality of the linearized operator increases and the background level in the pseudospectrum grows, as shown in figure 5.8.

Another useful information from pseudospectra is the sensitivity of an eigenvalue to arbitrary perturbations of the operator \mathbf{L} (Cerqueira and Sipp, 2014; Brynjell-Rahkola et al., 2017). As shown in chapter 28 of Trefethen and Embree (2005) for a convection-diffusion operator, high levels of non-normality typically cause iterative Arnoldi methods to converge to false eigenvalues. This is easily verified by comparing the effect of different shift values σ in the shift-inverse Arnoldi iteration. Here, as in Cerqueira and Sipp (2014), very large level of pseudospectral contours, typically above 11, prevent ARPACK from accurately converging all the eigenvalues. This algorithmic sensibility is not only a numerical convergence problem, it also highlights a physically ambiguous situation. Individual eigenvalues, when they are not robust, do not yield a specific contribution to the dynamics. In particular the associated eigenfrequencies are not resonant, and a large response to forcing is obtained even for forcing frequencies far from the eigenfrequencies (Trefethen et al., 1993). This is associated with the presence of a large hump (rather than narrow peaks) in the gain curve. In such a case, frequent in shear flows such as jets or boundary layers, one speaks of *pseudo-resonance*, see e.g. Garnaud et al. (2013). Non-robust eigenvalues are easily spotted as soon as their location in the complex plane depends on the shift σ chosen by the user, see figure 5.8(bottom right). Conversely, the most unstable eigenvalue $\lambda_r = 0.011$, $\lambda_i = 1.95$ at $Re = 3000$ in figure 5.8 can be trusted, and the growth rate λ_r predicted by the computation of eigenvalues will correspond to the growth rate of instability upon time linearized integration.

Finally, the pseudospectra can also be post-processed to extract a lower bound on the maximal transient growth associated with given initial perturbations. Following Chap. 14 in Trefethen and Embree (2005), the Kreiss constant is the lower bound of the maximal growth of the initial perturbation and is defined by:

$$\mathcal{K} = \sup_{\varepsilon > 0} \frac{\alpha_\varepsilon}{\varepsilon} \quad (5.14)$$

where α_ε is the pseudospectral abscissa (the maximal real part of the ε contour in the complex plane). Computation of \mathcal{K} for pseudospectra in figure 5.8 gives $\mathcal{K}_{Re=200} = 1.4 \times 10^3$ and $\mathcal{K}_{Re=3000} = 2.2 \times 10^8$, suggesting very large growth potential, as demonstrated by Daube and Le Quéré (2002) and Gesla et al. (2023) for the same set-up.

5.2 Experimental comparison

In this section, an effort is made to reproduce the experimental conditions where axisymmetric rolls were reported. A detailed comparison with the literature results can be challenging because of the many different configurations of the rotor-stator system reported in the literature. Apart from the value of the aspect ratio Γ , special attention has to be given to whether or not the shroud is rotating and whether the cavity extends or not to the axis. The latter case corresponds to the presence of a hub. Relevant experimental studies of the rotor-stator configuration at moderate aspect ratio Γ (from around 5 to around 20) are listed below :

1. Gauthier (1998), with a rotating shroud and no hub, reports circular rolls at $Re \approx 70$ for $\Gamma = 20.9$ and at $Re \approx 180$ for $\Gamma = 10$
2. Schouveiler et al. (2001) with a fixed shroud and no hub, reports circular rolls for a range of Γ , in particular at $Re \approx 160$ (deduced from figure 3 (Schouveiler et al., 2001) for $\Gamma = 10$)
3. Poncet et al. (2009) with a fixed shroud and a rotating hub, reports circular rolls at $Re = 160$ for $\Gamma = 8.8$

Numerical studies do not report sustained circular rolls in the absence of external forcing, at the exception of Daube and Le Quéré (2002) who considered larger Re values.

We focus specifically on the article by Schouveiler et al. (2001) and the corresponding parameters. The aspect ratio is hence temporary set to $\Gamma = 8.75$, the shroud is fixed and the range of values of Re (0 : 300) is selected. Unsteady nonlinear simulations with boundary forcing are performed with three different forcing protocols. The main difficulties in comparing numerics to experiments are the fact that i) the amplitude of the forcing is unknown ii) the temporal frequency spectrum of the forcing

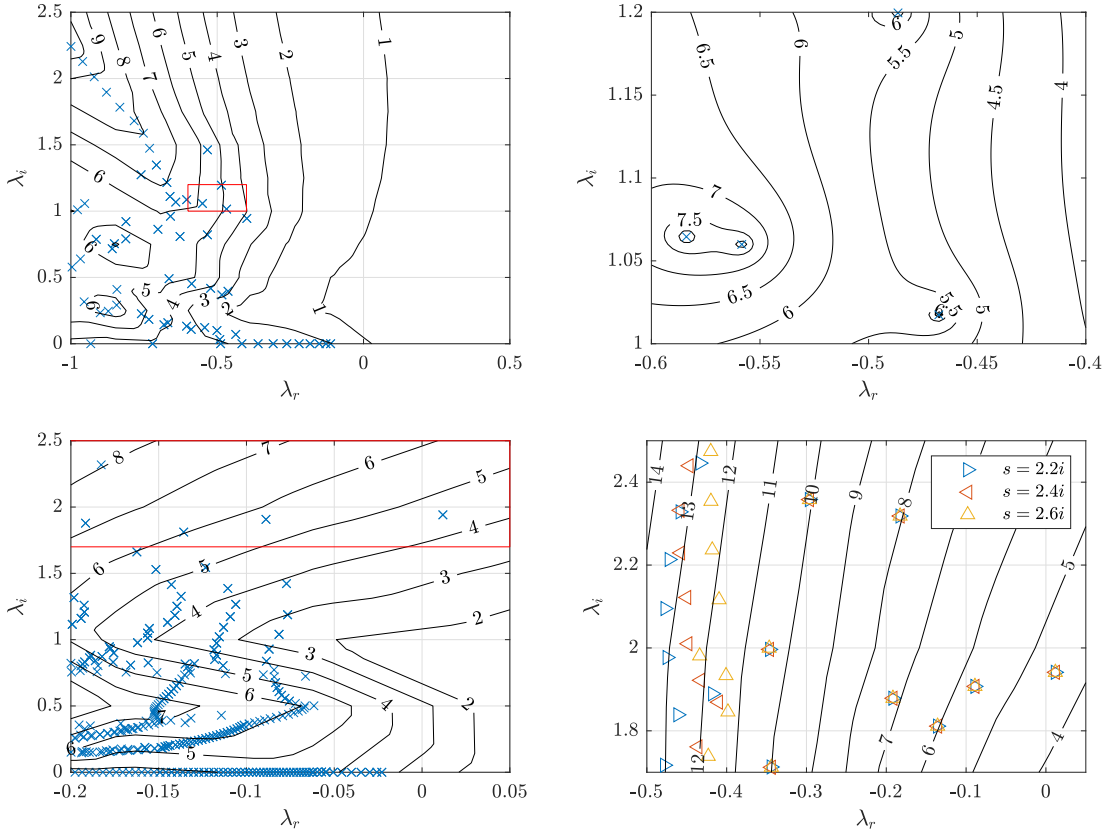


Figure 5.8: Pseudospectrum levels $\log_{10}||\mathbf{R}||_{\mathbf{Q}}$ in the complex plane where λ_r and λ_i are the real and imaginary part of the complex number $i\omega$. Top: $Re = 200$, bottom: $Re = 3000$. The right plot corresponds to the red inset in the left plot, where three different values of the shift s in the shift-and-invert algorithm have been used.

is often unknown. Three qualitatively different types of forcing have hence been considered here : monochromatic forcing, analogously to Do et al. (2010), with specific forcing frequency $\omega = 1$, harmonic forcing where only harmonics of $\omega = 1$ are considered, and eventually white noise forcing. In the case of harmonic forcing all the temporally resolvable harmonics of the disc angular frequency are forced with equal amplitude. This type of forcing is especially relevant to the experimental comparison : as shown in both Gauthier et al. (1999) and Faugaret (2020), the main spurious perturbations present in the experimental set-up are the disc harmonics. The studies of the forced regimes focused mostly on monochromatic forcing (Gauthier et al., 1999; Lopez et al., 2009; Do et al., 2010).

For these three forcing protocols an r -dependent observable needs to be monitored for all times. We select the observable $E(r, t)$ defined as

$$E(r, t) = \int_{\delta}^1 ((u_r)^2 + (u_{\theta})^2 + (u_z)^2) dz, \quad (5.15)$$

where $\delta = 0.2$ (in units of H) corresponds to integrating over 4/5 of the interdisc spacing (thereby excluding the parallel boundary layer along the rotor). This parameter $\delta = 0.2$ is preferred over $\delta = 0$ for the clarity of the resulting space-time diagrams. The results for the three type of forcing are presented in figure 5.9. All figures are accompanied by a snapshot of the same energy $E(r, t)$ at arbitrary time, seen from above in order to emphasize the visual comparison with experimental photographs. The three types of forcing all lead to wavetrains of circular rolls with E locally stronger in the interval $0.34 \leq r \leq 0.6$. The rolls reaching closest to the axis correspond to monochromatic forcing, while the front seems to remain further from the axis when the spectral content of the forcing is richer. The radial velocity of the rolls is always negative (oriented towards the axis) and can be estimated directly from the space-time diagrams. Even in the monochromatic case, their velocity is not constant and it depends on r : since the Bödewadt layer thickens as the perturbations migrate towards the axis where the radial velocity vanishes, the phase velocity of the rolls has to decrease, until the rolls can no longer sustain. The space-time diagram for the monochromatic case, qualitatively similar to Fig. 11 in Do et al. (2010), illustrates this point particularly well. In the harmonic case, the coexistence of different frequencies leads to different radial velocities being possible at a given radius. The dynamics becomes more complex since rolls can now travel at different velocities, leading to consecutive rolls merging or splitting. The pattern shown in Fig. 5.9 (middle), which shows periodic pairing and merging near $r \approx 0.75$ resembles in particular the experimental pattern shown in Figure 6 in Ref. Schouveiler et al. (2001) at the same value of Re . As for the white noise forcing protocol, pairing and merging events appears more intermittently admits otherwise periodic roll propagation.

The perfect agreement of the localisation of the rolls and the corresponding spacetime diagram with the experimental results of Schouveiler et al. (2001) both reinforce the interpretation of circular rolls as the preferred response of the system to external forcing.

5.3 Nonlinear receptivity

Receptivity to external disturbances in fluid flows is traditionally investigated using the linear toolbox of resolvent analysis, which is usually justified by the small perturbation velocities at play. This has the huge advantage that the responses to individual frequencies can be used as a basis to describe the global response to arbitrary forcing. Extensions of this formalism to finite-amplitude perturbations lead to new mathematical difficulties. Early efforts have focused on generalising the parabolised suitability equations (Bertolotti et al., 1992; Herbert, 1997), which unfortunately is not an option for recirculating flows. A recent attempt to add nonlinear triadic interactions to the resolvent formalism was recently proposed by Rigas et al. (2021) for boundary layer flow. For the rotor-stator flow the importance of nonlinear interactions in the dynamics of the circular rolls was already pointed out by Do et al. (2010), who measured a non-zero mean flow correction due to self-interaction of the unsteady rolls. Moreover strictly nonlinear structures (i.e. without any linear counterpart) have been determined numerically for the unforced problem by Gesla et al. (2023). It is legitimate to

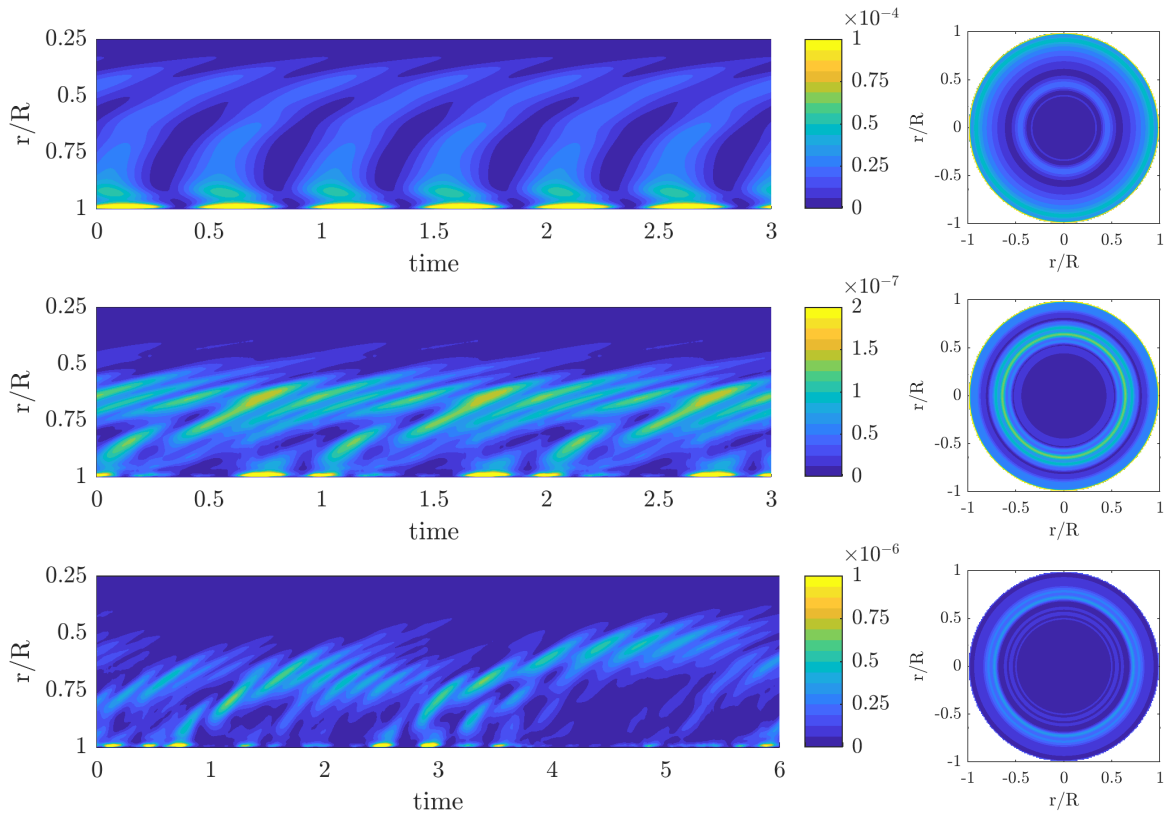


Figure 5.9: Energy integral $E(r,t)$ at $\text{Re}=225$, $\Gamma = 8.75$. Time is non-dimensionalised by the disc rotation period. An initial transient was neglected. Excited rolls travel inwards with a radial phase speed depending on the radius. Top: mono-frequency forcing at angular frequency $\omega = 1$. No merging and pairing of the rolls is observed. Middle: harmonic frequency $\omega = 1, 2, 3, \dots$ forcing. Pairing and merging of the rolls are observed here. Rolls merge because the phase speed depends on the radial position and the roll frequency ω . Bottom: white noise forcing. Complex roll dynamics is observed due to all frequencies being excited by the forcing.

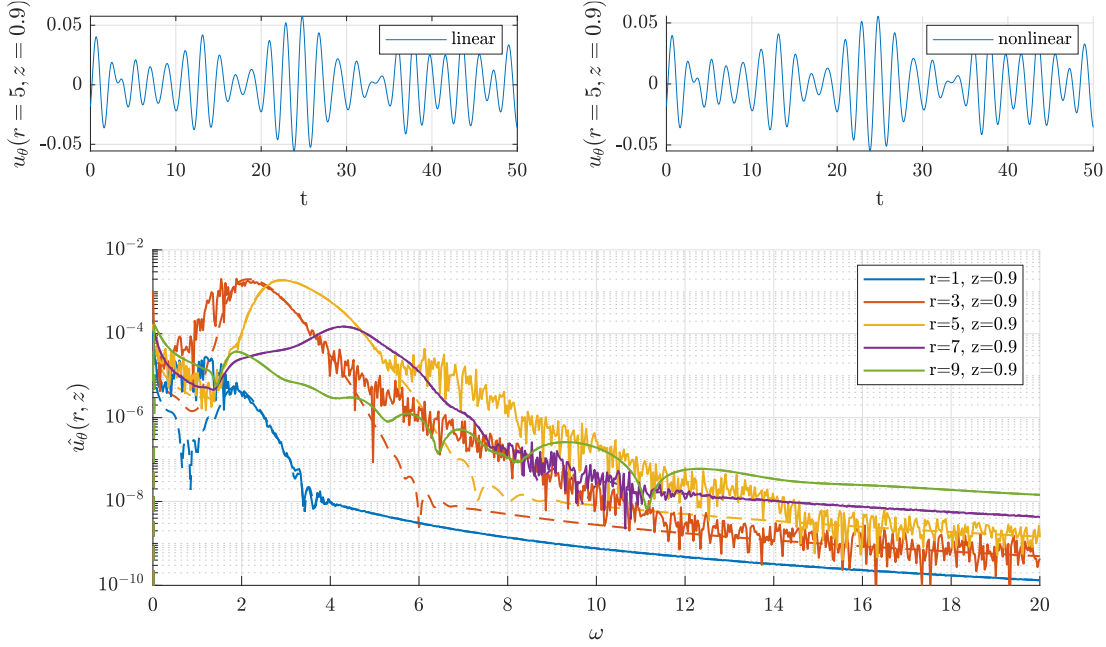


Figure 5.10: Comparison of linear and nonlinear time integration for $Re = 600$, numerical resolution R1. Top: perturbation azimuthal velocity u_θ at location ($r=5, z=0.9$) from linear (left) and nonlinear time integration (right). Bottom: Corresponding spectrum of non-linear (solid lines) and linear (dashed lines) at $z = 0.9$ for various r .

enquire whether they can also be detected in the forced problem, at least in the presence of large enough forcing amplitudes. In the present section, we revisit the nonlinear time integrations from Section 4 for a larger range of the parameters A (forcing amplitude) and Re .

5.3.1 Effect of the nonlinearity

We begin by describing the effect of increasing the forcing amplitude on the gain curves such as fig. 5.7. Since nonlinear effects are expected to become more important with increasing Re , we first illustrate its effect by choosing two representative values of $Re = 600$ and 2100. Rather than choosing two different values of the forcing amplitude in Eq. 5.12, we choose only one such value $A = 10^{-2}$ and compare respectively linear and nonlinear temporal simulations started from the same initial condition $\mathbf{u}(t = 0) = 0$. The case of $Re = 600$ is investigated in figure 5.10 while $Re = 2100$ is analysed in figure 5.11. For $Re = 600$, time series taken from probes located in the Bödewadt layer reveal visually no difference between linear and nonlinear simulations. The Fourier transforms of these signals, interpretable as local gain curves, reveal however that the fastest scales (large $\omega \gtrsim 4$) are affected by nonlinearity at least for the radii $r = 3$ and 5. At other radii neither the fast nor the slow scales are affected by nonlinearity. For $Re = 2100$, the situation is clearer : the velocity time series look very different and their Fourier transforms, unsurprisingly, differ at all radial locations. In all cases nonlinearity manifests itself by a slower, exponential-like decrease of the Fourier amplitudes with increasing ω , interpretable as a cascade in frequency space. It is also nonlinear interactions between the frequencies that are responsible for the irregular shape of the spectrum. This is because the timestep in the simulation cannot be commensurate with all frequencies present in the forcing.

Our goal is now to map in a (A, Re) diagram the different behaviours encountered in the simulations, whether linear or nonlinear. The followed strategy is illustrated in figure 5.12 by focusing on $Re = 2100$. The time series corresponding to the observable $\|\omega_{pert}\|$ defined by

$$\|\omega_{pert}\| = \sqrt{\iint |\omega - \omega_b|^2 r dr dz}, \quad (5.16)$$

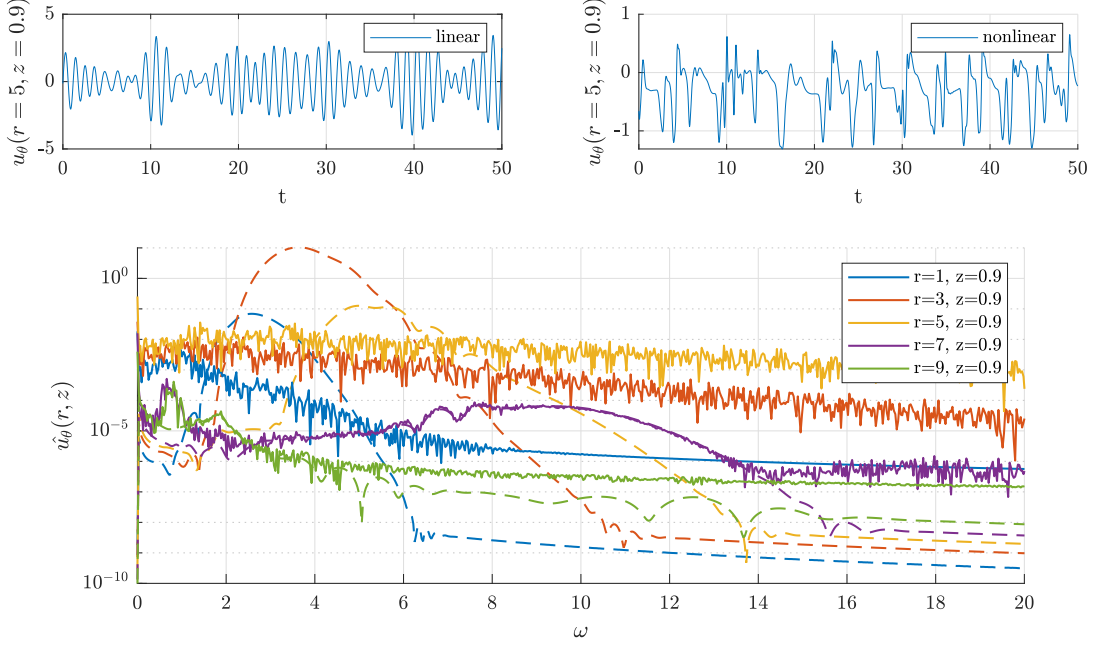


Figure 5.11: Comparison of linear and nonlinear time integration for $Re = 2100$, numerical resolution R1. Top: perturbation azimuthal velocity u_θ at location ($r=5, z=0.9$) from linear (left) and nonlinear time integration (right). Bottom: Corresponding spectrum of non-linear (solid lines) and linear (dashed lines) at $z = 0.9$ for various r .

where ω is the azimuthal vorticity and ω_b that of the base flow, are shown in figure 5.12 (left) in logarithmic scale, and in figure 5.12 (right) in linear scale, for an amplitude A spanning 6 decades from $A = 10^{-12}$ to $A = 10^{-6}$ (left) and 6 decades from $A = 10^{-7}$ to $A = 10^{-1}$ (right). For A from $A = 10^{-12}$ to $A = 10^{-8}$, the time series in figure 5.12 (left) differ only by their amplitude which turns out to be proportional to the value of A . For larger $A = 10^{-7}$ and especially 10^{-6} , the time series change aspect and their amplitude no longer follows A linearly. Note that the logarithmic scale is essential for this assessment, by comparison in figure 5.12(right) is much less easy to interpret along these lines.

This analysis can be repeated for different values of Re . In figure 5.13 (left), the time-averaged $\|\omega_{pert}\|$ is plotted directly versus the forcing amplitude A . This representation allows for a direct assessment of the parameter values for which $\|\omega_{pert}\|$ scales linearly with A , which suggests linear receptivity. All the points lying away from the related straight lines are labelled as nonlinear in the (A, Re) map of figure 5.13 (right). Beyond the simple linear/nonlinear labelling, we note that for the three largest values of $Re = 2100, 2400$ and 2700 in figure 5.13 (left), the observable $\|\omega_{pert}\|$ saturates with increasing A to an almost constant level. This suggests that the final state of the simulation is the same whatever A , in other words that the forced system is attracted towards a different region of the state space for at least $Re \gtrsim 2100$. A non-trivial chaotic attractor was reported, for the same parameters, for the unforced problem, by Daube and Le Quéré (2002) and Gesla et al. (2023), for $Re \gtrsim 1800$. This attractor is different from the laminar one and it has a different attraction basin in terms of initial condition. There is little doubt that the same attracting chaotic state is identified here in the presence of strong amplitude forcing (the initial condition being fixed). A closer zoom on the figure, especially in linear scale, would show that the saturated value of the observable depends weakly on A , which suggests that the associated attractor is gently sensitive to the unsteady forcing. When such an attractor is reached, the corresponding point (A, Re) in the map of figure 5.13 (right) changes from red to blue. The points that are red correspond to the values of (A, Re) where nonlinear effects do bend the gain curves (left figure), but no finite amplitude state is present and thus no saturation to any non-trivial state can occur. This leads to a 3-colour cartography of the parameter space (A, Re) for the chosen forcing protocol parameterised by the amplitude parameter A .

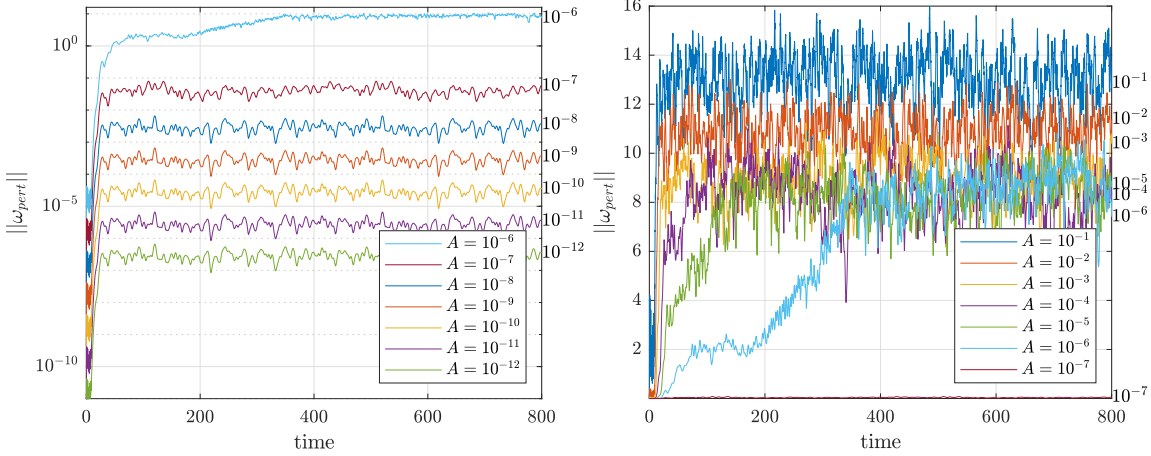


Figure 5.12: Global observable $\|\omega_{pert}\|$ in nonlinear time integration at $Re = 2100$ for varying forcing amplitude A . The values of A are indicated both in the legend and in the plot for simplicity. Starting from $A = 10^{-7}$ nonlinear effects are observed. For $A \geq 10^{-6}$ the observable jumps to a different level corresponding to the presence of a non-trivial *top branch* solution.

The notion of double threshold, popular in the shear flow transition community (Grossmann, 2000), appears here in both A and Re (rather than in initial perturbation amplitude and Re), for a forced rather than unforced problem. The boundary between linear and nonlinear behaviour in 5.13 (right) is consistent with an approximate fit of the form $A = O(Re^{-\alpha})$, with $\alpha \approx 10$. This large value of α is the signature of a very steep boundary. As for the boundary between red (nonlinear) and blue (non-trivial saturation), the present data does not suggest any simple fit. Besides the dataset is known to end at $Re \approx 3000$, beyond which all points are blue because the base flow is linearly unstable and the turbulent state is the only attractor left (Gesla et al., 2023). Rather than a cartography in the (A, Re) plane, where A is specific to a given forcing protocol, we plot in Figure 5.14 the time-averaged observable $\|\omega_{pert}\|$ versus Re , the value of A being treated implicitly. The data is represented using the same colour coding as the preceding figure, both in linear (left figure) and in logarithmic scales (right figure). In both plots the data corresponding to the non-trivial top and lower branches (i.e. edge states) obtained in Gesla et al. (2023) are also superimposed for clarity (the same observable was used, see their figure 19). The two upper and lower branches from the unforced problem were reported to merge in a saddle-node bifurcation at $Re = Re_{SN} \approx 1800$. Interestingly, none of the red or blue data points, which correspond to the unforced problem, fall in the gap between the lower and upper branch. To our knowledge it is the first time that deterministic data from an unforced problem compares so favourably with data from the forced problem. The right panel of the figure shows the same data in logarithmic scale. There, for the choice of this observable, the boundary between linear and nonlinear behaviour obeys an approximate power-law scaling $\|\omega_{pert}\| = O(Re^{-\beta})$, with $\beta \approx 3.88$.

5.3.2 Leaky chaotic attractors and finite lifetime dynamics

From the previous subsection, we know that forcing the nonlinear problem with a sufficiently large amplitude leads, for Re above $Re_{SN} \approx 1800$, to a response different from the response triggered at lower forcing amplitudes. The difference is attested for global observables such as in figure 5.12 and it is also clear from local velocity probes, as shown in Figure 5.15 for $Re = 2100 > Re_{SN}$. In the left panel, low amplitude values $A \leq 10^{-7}$ (corresponding to green points in Figure 5.13) lead to a disordered response whose diameter increases (linearly) with the value of A . In the right panel, only values of $A \geq 10^{-6}$ are displayed and it is apparent again, especially from the numbers along the axes, that the response depends weakly on A . This last point suggests the existence of an attracting state independent of A , in other words a deterministic attractor, solution of the forced problem, identical to the top-branch solutions identified by Gesla et al. (2023). Similar conclusions can be drawn for all Re larger than 2100, including the supercritical values larger than $Re_c \approx 3000$ when

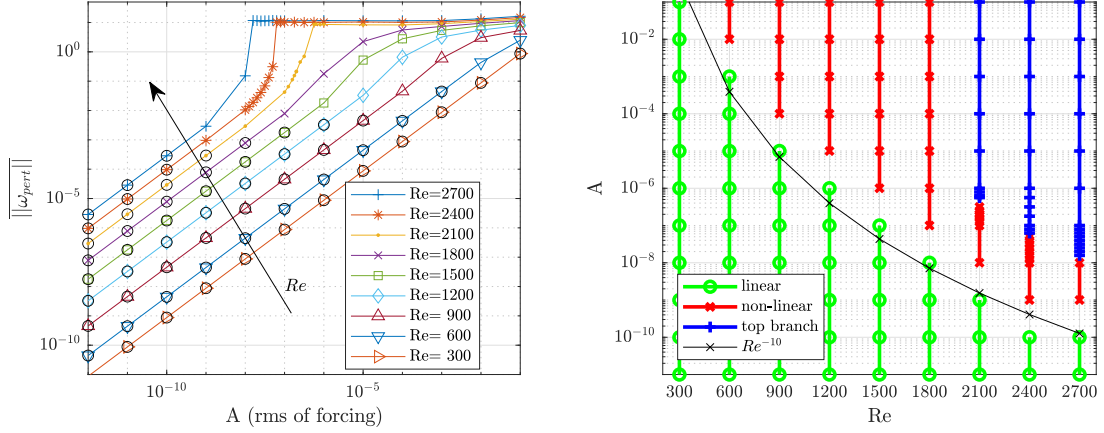


Figure 5.13: Left: mean observable value $\|\omega_{pert}\|$ as a function of forcing amplitude A . The linear regime is indicated using open symbols whenever the slope of the line is at most 1% different from 1. For $Re \geq 2100$ the mean observable value level jumps to the top branch level for strong enough forcing amplitudes. Right: amplitudes corresponding to linear and nonlinear regime indicated respectively with green and red symbols. The top branch is reached for $Re > 1800$ whenever $\|\omega_{pert}\| > 5$.

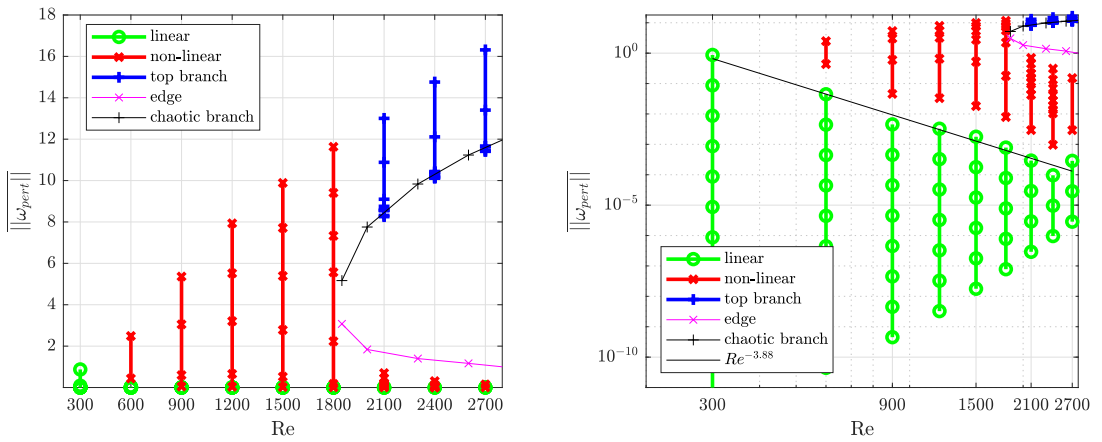


Figure 5.14: Left: mean observable value $\|\omega_{pert}\|$ as a function of Re . The data corresponding to the chaotic solutions from Gesla et al. (2023) are superimposed in respectively blue (top branch) and pink (for the edge branch). Same colour coding as in the previous figure. Right : same data plotted in logarithmic scales.

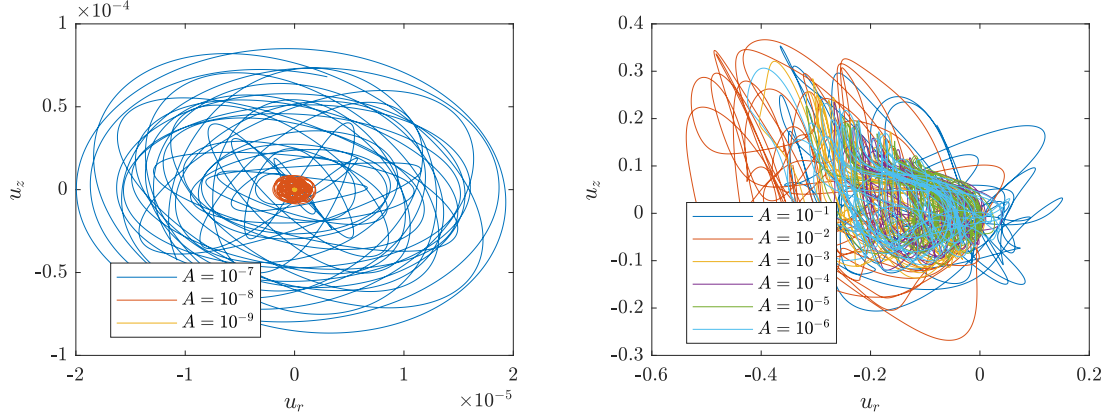


Figure 5.15: Two-dimensional state portrait (u_r, u_z) from a velocity probe located ($r = 5$, $z = 0.9$) at $Re = 2100$. The width of the state portraits increases linearly with the forcing amplitude for $A \leq 10^{-7}$. For $A \geq 10^{-6}$ state portraits lose their elliptic shape. The center of mass of the state portrait also shifts away from 0, indicating strong nonlinear interaction.

only the non-trivial attractor is stable.

Departures from this picture can however be noted at lower Re close (but above) Re_{SN} . Figure 5.16 shows the outcome several temporal simulations of the unforced problem for $Re = 1840$, focusing on the time series of $\|\omega_{pert}\|(t)$. These time series demonstrate that the chaotic behaviour lasts for a finite time only, after which the observable rapidly reaches zero, indicating a return to the base flow. Some of the measured lifetimes are much longer than the duration of the return to the base flow, which justifies the label *supertransient* (Lai and Tél, 2011). The statistics of the lifetimes have been gathered over many such realisations of the deterministic problem, all initialised by different velocity fields drawn randomly. The cumulative distribution of the lifetimes $P(T > t)$, where T is the lifetime, are shown in figure 5.17(left) for several values of Re between 1800 and 1840. The distributions all look exponential for up to two decades, which suggests a memoryless process (Bottin and Chaté, 1998). The average value \bar{T} of the lifetime is then plotted versus Re in figure 5.17(right), where the y -axis is represented in logarithmic scale. The mean lifetime \bar{T} increases fast with Re . Although no functional fit emerges from the data, the growth of $\bar{T}(Re)$ appears faster than exponential. The whole situation is reminiscent from the finite probabilities to relaminarise in three-dimensional turbulence in wall-bounded shear flows, notably the case pipe flow, where lifetimes were reported to increase super-exponentially with Re (Hof et al., 2008). For the case of pipe flow, the academical issue of whether lifetime truly diverge at a finite value of Re or stay finite was solving by remarking that another competing phenomenon, namely turbulence proliferation, would outweigh turbulence decay above some threshold in Re (Avila et al., 2011) and keep turbulence alive for all times. There is no such equivalent here in axisymmetric rotor-stator flow, for which a scenario where lifetimes are always finite is a possibility. Nevertheless, we stress that this debate is essentially academical, the values of T found *in practice* being so large that they usually exceed the observation times allowed for. In other words, the hypothesis that the invariant set underlying the existence of non-trivial dynamics in the forced problem is a deterministic attractor is only here for commodity : mathematically speaking it could possibly be a leaky attractor i.e. a chaotic saddle (Lai and Tél, 2011).

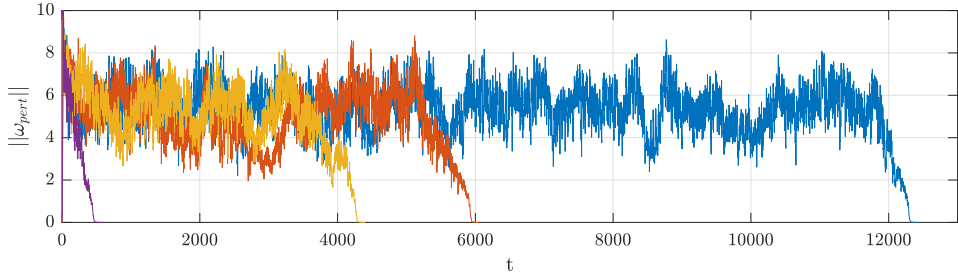


Figure 5.16: Time series of $\|\omega_{pert}\|(t)$ for $Re = 1840$, unforced problem. Random initial perturbations of amplitude 8×10^{-3} added to the u_θ component. Four different initial conditions lead to four different lifetime values.

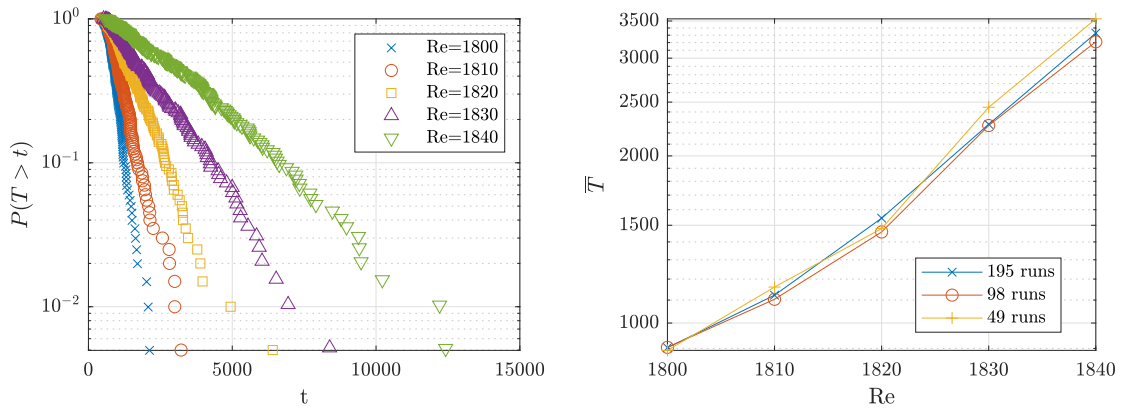


Figure 5.17: Left: Cumulative distribution function $P(T > t)$ for the lifetime T . P is estimated as the fraction of runs that did not relaminarise in the time interval $(0 : t)$. Relaminarisation is decided whenever $\|\omega_{pert}\| < 10^{-3}$. For each value of Re around 200 simulations with different random initial perturbation were conducted. Right: Dependence of the mean lifetime \bar{T} on Re . The different data illustrate the sensitivity of the mean lifetime w.r.t. the total number of runs. For a memoryless process the distributions in the left plot would be exactly exponential and the mean lifetime would be the reciprocal of their slope.

Chapter 6

Stability analysis using Chebyshev polynomial expansion

In this chapter a new method to compute a periodic orbit of a dynamical system is described. One of the most popular approaches is the Harmonic Balance Method (HBM), which expresses the cycle as a sum of Fourier modes and analyses its stability using the Hill's method. A drawback of Hill's method is that the relevant Floquet exponents have to be chosen from all the computed exponents. To overcome this problem the current work discusses the application of Chebyshev polynomials to the description of the time dependence of the periodic dynamics.

The method is applied to low dimensional dynamical systems and to natural convection in a differentially heated cavity which demonstrates its potential for large scale problems arising from the discretisation of the incompressible Navier-Stokes equations.

6.1 Introduction

The numerical identification of periodic orbits (POs) of a nonlinear dynamical system, and the computation of their stability is crucial in many domains of physics and engineering. Periodic solutions are often the simplest sustained unsteady solutions. They can be/are often associated with the destabilisation of a fixed point solution of the system. In dissipative dynamical systems featuring attractors, periodic orbits can be stable or unstable. Deterministic chaotic attractors are known to be organised around an infinity of unstable periodic orbits ranked by their stability (Cvitanovic et al., 2005), which makes periodic orbits and their stability characteristics crucial even in chaotic settings.

Many numerical approaches to the determination of periodic orbits in ordinary differential equations (ODEs) exist. Popular choices include shooting methods and their variants (see section 6.2), delayed feedback methods inspired by control theory (Pyragas, 1992) or adjoint-based methods (Farazmand, 2016). Another class of methods express the periodic orbit (PO) in a "global" manner (Lan and Cvitanović, 2004; Parker and Schneider, 2022). Among them, one of the most widely used methods is a Fourier based Galerkin method, also known as Harmonic Balance Method (HBM)(e.g. Cochelin and Vergez (2009)). HBM assumes the periodic orbit as a truncated Fourier series. Because of the spectral expression of the cycle, high accuracy or equivalently fast convergence can be achieved. The HBM was historically mainly used for low-dimensional ODE systems in mechanical and electrical engineering. Recent studies have begun to consider such methods for higher-dimensional systems stemming from the spatial discretisation of partial differential equations (PDEs), in particular in fluid mechanics (Bengana et al., 2019; Rigas et al., 2021; Sierra-Ausin et al., 2022). The linear stability of an HBM solution is usually analysed by forming the so-called Hill's matrix, analysing its eigenvalues in the search for unstable Floquet exponents. As pointed out by some authors (see e.g. Lazarus and Thomas (2010)), a substantial drawback of using Hill's matrix is that only a subset of the computed eigenvalues are relevant. As a consequence, various methods need to be used to filter out the relevant exponents from the spurious ones in case of low-dimensional (Lazarus and Thomas, 2010; Peletan et al., 2013; Wu et al., 2022; Bayer and Leine, 2023) and high-dimensional (Pier and

Schmid, 2017; Kern et al., 2024) systems.

As the key idea behind this work, it is possible to use another functional basis than the Fourier basis in the HBM equations. The present work introduces a description where the whole orbit is expressed as a weighted sum of the Chebyshev polynomials. The stability of the orbit emerges naturally as a generalised eigenvalue problem involving the jacobian matrix computed in the Newton Raphson method to converge the orbit itself and yielding the most unstable Floquet multipliers.

Several studies have reported the use of Chebyshev polynomials. The earliest applications of applications of Chebyshev polynomials for the computation of periodic motion concern orbital motion (Kolenkiewicz and Carpenter, 1967). Zhou et al. (2001) also used a Chebyshev expansion of the PO in forced and an unforced problems. Zhou et al. (2013) uses the Chebyshev expansion to approximate the periodic orbit but the stability properties of the orbit are analysed by forming a monodromy matrix. The authors claim higher accuracy when using a Chebyshev basis instead of a Fourier basis. This claim will be contested in the current work. An interesting study employing a Chebyshev basis for the linear stability analysis (LSA) is the article by Woiwode and Krack (2023), which differs from the method presented here. Authors used the Chebyshev polynomials to construct the monodromy matrix built on top of the orbit expressed with Fourier modes. Interestingly, the authors claim to be the first ones to use the Chebyshev basis for the purpose of investigating the stability of the periodic solution. They also claim that the HBM is usually superior to the shooting methods when a smooth periodic solution is considered, yet it suffers from an excessive number of modes in the decomposition in the presence of sharp gradients.

The chapter is structured as follows. Section 6.2 introduces the concept of periodic orbits as well as different numerical techniques to compute them, including finite differences method and the Harmonic Balance Method. The method of expressing the time dependence using the Chebyshev expansion is explained in detail. Section 6.3 shows numerical examples from the Lorenz and Langford systems, together with the linear stability analysis of these orbits. An example of a periodic orbit solution in a differentially heated cavity flow is shown in section 6.4. Finally, section 6.5 summarises the presented work and gives an outlook future studies.

6.2 Description of a periodic orbit

6.2.1 General concepts

Given a nonlinear system governed by the following equation :

$$\frac{d\mathbf{x}}{dt^*} = \mathbf{f}(\mathbf{x}), \quad (6.1)$$

where $\mathbf{x} \in \mathbb{R}^d$ is the state vector of the system and ($d \in \mathbb{N}^*$) is the number degree of freedom, $t^* \in \mathbb{R}^+$ and $\mathbf{f} : \mathbb{R}^d \rightarrow \mathbb{R}^d$ is a smooth enough function of \mathbf{x} . A periodic orbit of the system with period $T \in \mathbb{R}^+$ satisfies the relation:

$$\mathbf{x}(t^* + T) = \mathbf{x}(t^*) \quad (6.2)$$

for a given value of $T > 0$ and for all t^* . The smallest value of T defines the period of the PO. Eq. (6.2) does not define the solution in a unique way as any solution shifted in time is also a solution. A phase condition has to be introduced. In the current work the time derivative of one of the components of \mathbf{x} will be fixed to zero to form a phase condition.

Often there is no general way to find all periodic orbits of a nonlinear dynamical system (Kuznetsov et al., 1998). The simplest method, if a stable PO exists, is to use a numerical time integrator and solve an initial value problem (IVP). Provided the initial point belongs to the basin of attraction of the requested PO, numerical simulation will by definition converge towards this specific PO. However for weakly stable orbits convergence may be slow and unstable POs will not be found.

If time is rescaled such that the PO is defined over a time interval of length unity, the period T becomes a parameter of the system and finding a PO can be recast as a boundary value problem. Equations (6.1) and (6.2) become

$$\frac{d\mathbf{x}}{dt} = T\mathbf{f}(\mathbf{x}) \text{ and } \mathbf{x}(1) = \mathbf{x}(0) \text{ for } t \in [0, 1]. \quad (6.3)$$

More specifically, it is a two-point BVP where periodic boundary conditions are imposed. This observation paves the way for alternate strategies to find PO thanks to the numerous numerical techniques dedicated to two-point BVP.

One of the most popular techniques for solving two-point BVP is the shooting method and its variants (e.g. Atkinson (1991)). It is based on sequences of a repeated IVP solver, iteratively refining the initial values and the period to the point where periodicity is satisfied over the unity interval. The iterative process converges when the initial value lies on a stable or unstable periodic orbit and matches the end value within some prescribed accuracy. An overview of shooting algorithms applied to large multidimensional systems can be found in Sánchez et al. (2004); Viswanath (2007); Frantz et al. (2023). To analyse the stability of the solutions found, a transfer matrix, known as a monodromy matrix, is formed. It corresponds to a linear mapping of the perturbation to the orbit over one period. By computing the eigenvalues of the monodromy matrix, the stability of the orbit is determined (Seydel, 1987). However, shooting methods may fail if the PO is unstable. Even if the initial values are close to a PO point, the numerical integration can deviate from the desired PO and especially if the perturbation undergoes a quantitatively large amplification after a period (see e.g. Duguet et al. (2008a)), numerical convergence can be hampered.

More robust alternate techniques to solve two-point BVPs can be used. The entire PO can be discretised as a finite set of points lying on the orbit. The governing equations are satisfied at each of these points. As an alternative, the PO can also be expanded as a series on a well-chosen functional basis. The simplest option, given the temporal periodicity of the underlying PO solution, is to consider a Fourier expansion, yet this is not the only possible choice as will be made clear later. Instead of iterating only on the initial conditions and the period as in the shooting method, each iteration to reach the PO involves computing all the points of the orbit or all coefficients of the expansion simultaneously. The size of the linear system solved at each iteration scales linearly with the number of variables times the number of points on the orbit / retained coefficients. Variants of these approaches combine highly accurate polynomial expansions between discrete points of the orbit. This technique is implemented for example in the software package AUTO (Doedel et al., 2001).

We now present the three different techniques used in this work in order to compare them.

6.2.2 Finite differences

In the simplest form the time derivative in the equations (6.3) could be approximate using second order accurate Crank Nicolson finite difference scheme :

$$\dot{x}_i^{n+1/2} = \frac{x_i^{n+1} - x_i^n}{dt} \text{ for } n = 1, 2, \dots, N_P \text{ and } i = 1, 2, \dots, d \quad (6.4)$$

where i is the index of the degree of freedom, n is the index of the temporal position on the orbit discretized over N_P points and dt is the time interval between two discrete states \mathbf{x}^n and \mathbf{x}^{n+1} . For simplicity, dt is assumed constant. This leads to a discrete set of equations :

$$\begin{cases} \frac{T}{2} (f(x_i^{n+1}) + f(x_i^n)) - \frac{x_i^{n+1} - x_i^n}{dt} = 0, \\ x_i^{N_P+1} - x_i^1 = 0, \\ \frac{x_1^2 - x_1^1}{dt} = 0. \end{cases} \quad (6.5)$$

The first equation is written for all n positions on the orbit and all i degrees of freedom. The second equation expresses periodicity for all degrees of freedom. The last equation closes the system for the extra unknown T by expressing a phase condition. Various choices of phase condition are possible (see chapter 7 in Seydel (2009)). Here, the time derivative of the first degree of freedom ($i = 1$) is imposed to be zero on the orbit to second order accuracy at mid-point between $n = 1$ and $n = 2$. The resulting algebraic nonlinear system (6.5) can be solved by Newton-Raphson's method.

The Jacobian computed in each Newton-Raphson iteration is a square bordered block matrix of dimension $(N_P + 1)d + 1$ in the following form :

$$\left[\begin{array}{cccccc|c} A_{1,1} & A_{1,2} & 0_d & \cdots & \cdots & 0_d & \boldsymbol{\alpha}_1 \\ 0_d & A_{2,2} & A_{2,3} & \ddots & & \vdots & \boldsymbol{\alpha}_2 \\ \vdots & \ddots & \ddots & \ddots & \ddots & \vdots & \vdots \\ \vdots & & \ddots & \ddots & \ddots & 0_d & \vdots \\ 0_d & \cdots & \cdots & 0_d & A_{N_P,N_P} & A_{N_P,N_P+1} & \boldsymbol{\alpha}_{N_P} \\ -I_d & 0_d & \cdots & \cdots & 0_d & I_d & 0_{d1} \\ \hline -\boldsymbol{\beta} & \boldsymbol{\beta} & 0 & \cdots & \cdots & 0 & 0 \end{array} \right] \quad (6.6)$$

where I_d and 0_d are identity and null $d \times d$ submatrices. The $d \times d$ submatrices $A_{n,n}$ and $A_{n,n+1}$ are derived from the jacobian of the function defined by the left hand side of the first equation in the system (6.5). These matrices are obtained as the first-order partial derivative with respect to x_i^n for all i, n being fixed. Similarly $A_{n,n+1}$ are obtained by deriving with respect to x_i^{n+1} . The row vector $\boldsymbol{\beta} \in \mathbb{R}^d$ is given by $[1/dt, 0, \dots, 0]$ and 0_{d1} is the null column vector in \mathbb{R}^d . Finally, the $\boldsymbol{\alpha}_n = 1/2(f(\mathbf{x}^n) + f(\mathbf{x}^{n+1}))$ are column vectors of size d .

This specific structure of the Jacobian is obtained assuming the following ordering of the unknowns $[\mathbf{x}^1, \mathbf{x}^2, \dots, \mathbf{x}^{N_P+1}, T]$. As the Jacobian is sparse and bordered, efficient techniques to solve the linear system can be used.

Computation of the stability of the periodic orbit solution

The stability of the periodic solution is found by introducing explicitly the Floquet multipliers σ in an eigenvalue problem which can be directly derived from the computation of the periodic orbit. This approach was suggested by Fairgrieve and Jepson (1991) to avoid forming the monodromy matrix. The solution vector $\mathbf{u} = [\mathbf{x}^1, \mathbf{x}^2, \dots, \mathbf{x}^{N_P+1}]$ is perturbed by a small $\mathbf{v} = [\mathbf{x}'^1, \mathbf{x}'^2, \dots, \mathbf{x}'^{N_P+1}]$. The d Floquet multipliers $\sigma \in \mathbb{C}$ are defined by:

$$\mathbf{x}'^{N_P+1} = \sigma \mathbf{x}'^1 \quad (6.7)$$

The orbit is stable if $|\sigma| < 1$, neutrally stable if $|\sigma| = 1$ and unstable if $|\sigma| > 1$. In order to use the jacobian matrix (6.6) in the eigenvalue problem with no extra-computations, the equation (6.7) is rewritten as :

$$\mathbf{x}'^{N_P+1} - \mathbf{x}'^1 = \gamma \mathbf{x}'^{N_P+1} \quad \text{where } \gamma = 1 - \frac{1}{\sigma}. \quad (6.8)$$

The linearisation of the governing equations around the solution \mathbf{u} and T leads to :

$$\mathbf{J}\mathbf{v} = \gamma \mathbf{B}\mathbf{v}. \quad (6.9)$$

The matrix \mathbf{J} of dimension $(N_P + 1)d$ is extracted straightforwardly from the matrix (6.6) by removing the last line and the last column. The matrix \mathbf{B} of dimension $(N_P + 1)d$ is defined by

$$\left[\begin{array}{ccccc|c} 0_d & \cdots & \cdots & \cdots & 0_d & 0_d \\ \vdots & \ddots & & & \vdots & \vdots \\ \vdots & & 0_d & & \vdots & \vdots \\ \vdots & & & \ddots & \vdots & \vdots \\ 0_d & \cdots & \cdots & \cdots & 0_d & 0_d \\ \hline 0_d & \cdots & \cdots & \cdots & 0_d & I_d \end{array} \right]. \quad (6.10)$$

The eigenvalue problem has $(N_P + 1) d$ eigenvalues. $(N_P d)$ eigenvalues are infinite and the Floquet multipliers σ can be computed from the d finite eigenvalues γ . The eigenvalue problem is solved using the routine *eig()* of Matlab.

6.2.3 Harmonic balance method

Whenever a high temporal accuracy is needed the description of the orbit could be modified from an ensemble of points lying on the orbit to a series expansion with an appropriate basis. A natural choice to cope with periodicity is the use of trigonometric functions as a basis. In HBM, the periodic orbit is expressed as a standard Fourier series:

$$\mathbf{x}(t) = \sum_{k=-N_F}^{N_F} \mathbf{u}_k e^{i2\pi k t}, \quad t \in [0, 1] \quad (6.11)$$

where N_F is the number of modes retained in the expansion and the \mathbf{u}_k 's are complex coefficients. Since $x(t)$ is real the \mathbf{u}_k is the complex conjugate of the \mathbf{u}_{-k} , a property that can be used to reduce the number of unknowns. Naturally the higher N_F , the more accurate the description of the periodic orbit. Due to the spectral description, HBM is very accurate and a small number of modes is enough to describe simple orbits provided the solution is smooth enough. The complex coefficients \mathbf{u}_k can be found by introducing the decomposition (6.11) to the system of governing equations (6.3). The orthogonality of the Fourier modes is used to generate a system of nonlinear algebraic equations. As for the finite differences method, those equations can then be solved with a standard Newton-Raphson method. However, the Jacobian is no longer sparse.

Computation of the stability of the periodic orbit solution

To retrieve the stability of the orbit a Hill's method can be used. The details of such derivation are described in (Guillot et al., 2020) and we only summarize the main steps here. It suffices to say that the each coefficient of the solution \mathbf{u}_k is perturbed by a \mathbf{v}_k assumed to be smaller in amplitude than \mathbf{u}_k :

$$\mathbf{x}'(t) = \sum_{k=-N'_F}^{N'_F} \mathbf{v}_k e^{\mu t} e^{i2\pi k t} \quad (6.12)$$

In the most general case N_F and N'_F do not have to be equal. In practice it is however often assumed that $N_F = N'_F$. The form (6.12) is then introduced into the governing equation which, upon linearisation, yields an eigenvalue problem. The temporal growth or decay of the perturbation x' is governed by an exponential term $e^{\mu t}$. Fourier coefficients v_k correspond only to the form of the perturbation and the factor $e^{\mu t}$ is responsible for the exponential growth/decay. One well known problem of Hill's method is that it yields the Floquet exponents μ which are, by definition, not unique. When $N_F \rightarrow \infty$ all the $\mu \pm i\omega$ ($n \in \mathbb{N}$) are Floquet exponents. In the case of finite truncation the above relation will only be approximately satisfied and it is challenging to choose a subset of μ corresponding to unique Floquet multiplier σ .

An effort could be made therefore to express the periodic orbit as a weighted sum of functions from another functional basis, one that is not by construction periodic. A good candidate seems to be the orthogonal basis of Chebyshev polynomials. Expanding a smooth enough function on a Chebyshev basis is known to minimise the pointwise error of the approximation of analytic function so this basis could be preferred over any other polynomial basis. A close relation between the Chebyshev basis and Fourier basis (discussed in Boyd (2001)) makes the usage of the former a natural choice in the present study.

6.2.4 Chebyshev polynomial expansion

To express the temporal dependence a weighted sum of Chebyshev polynomials is used:

$$\mathbf{x}(\tilde{t}) = \sum_{k=0}^{N_C} \mathbf{a}_k T_k(\tilde{t}) = \sum_{k=0}^{N_C} \mathbf{a}_k \cos(k \arccos \tilde{t}), \quad \tilde{t} \in [-1, 1] \quad (6.13)$$

where $N_C + 1$ is the number of polynomials retained in the truncation of an infinite sum. Since the polynomials $T_k(\tilde{t})$ are defined for $\tilde{t} \in [-1, 1]$ a proper rescaling of the governing equations will have to be done. As with Fourier basis we denote by \mathbf{x}' the perturbation to the periodic orbit solution $\mathbf{x}(t)$.

The Chebyshev polynomials are not periodic by construction, hence the condition $\mathbf{x}(1) = \mathbf{x}(-1)$ has to be enforced. The decomposition (6.13) is introduced into the governing equation (6.3) leading to :

$$\mathbf{f} \left(\sum_{k=0}^{N_C} \mathbf{a}_k T_k(\tilde{t}) \right) - \frac{2}{T} \sum_{k=1}^{N_C} k \mathbf{a}_k U_{k-1}(\tilde{t}) = 0, \quad (6.14)$$

where the Chebyshev polynomials of second kind $U_k(\tilde{t})$ are used to express the derivative of $T_k(\tilde{t})$. The time derivative has to be transformed as $\frac{d\mathbf{x}}{dt} = 2 \frac{d\mathbf{x}}{d\tilde{t}}$, where the original time $t \in [0, 1]$ is transformed into $\tilde{t} \in [-1, 1]$.

In order to generate a set on nonlinear algebraic equations the governing equation (6.14) is evaluated at the N_C first Gauss-Lobatto points. Gauss-Lobatto points are defined by:

$$\tilde{t}_l = -\cos \left(\frac{k\pi}{N_C} \right), \quad l = 0, 1, 2, \dots, N_C \quad (6.15)$$

and span the whole interval $[-1, 1]$ in a non-uniform manner. Writing equation (6.14) at the points $\tilde{t}_0 \dots \tilde{t}_{N_C-1}$ yields to $N_C \times d$ equations. Enforcing the periodicity condition

$$\mathbf{x}(1) - \mathbf{x}(-1) = \sum_{k=0}^{N_C} \mathbf{a}_k (1 - (-1)^k) = 0 \quad (6.16)$$

using $T_k(1) = 1$ and $T_k(-1) = (-1)^k$ yields to d additional equations. The last equation comes from the phase condition. Enforcing a zero derivative with respect to time at $\tilde{t} = -1$ to an arbitrary degree of freedom (here x_1 , the first component of \mathbf{x}) leads to :

$$\frac{dx_1}{dt} \Big|_{\tilde{t}=-1} \equiv \sum_{k=1}^{N_C} k a_{1k} U_{k-1}(-1) = 0, \quad (6.17)$$

where a_{1k} are the weights for x_1 . The set of $(N_C + 1)d + 1$ nonlinear algebraic equations is solved with the Newton-Raphson method.

The Jacobian computed in each Newton-Raphson iteration is a square bordered block matrix of dimension $(N_C + 1)d + 1$ in the following form, assuming the following ordering of the unknowns $[\mathbf{a}_0, \mathbf{a}_1, \dots, \mathbf{a}_{N_C}, 1/T]$:

$$\left[\begin{array}{cccccc|c} A_{0,0} & A_{0,1} & \cdots & \cdots & \cdots & A_{0,N_C} & \boldsymbol{\delta}_0 \\ A_{1,0} & A_{1,1} & \cdots & \cdots & \cdots & \vdots & \boldsymbol{\delta}_1 \\ \vdots & \ddots & \ddots & \ddots & \ddots & \vdots & \vdots \\ \vdots & \ddots & \ddots & A_{l,k} & \ddots & \vdots & \boldsymbol{\delta}_l \\ \vdots & \ddots & \ddots & \ddots & \ddots & \vdots & \vdots \\ A_{N_C-1,0} & \cdots & \cdots & A_{N_C-1,k} & \cdots & A_{N_C-1,N_C} & \boldsymbol{\delta}_{N_C-1} \\ 2 C_d^0 & \cdots & \cdots & 2 C_d^k & \cdots & 2 C_d^{N_C} & 0_{d1} \\ \hline \epsilon_0 & \epsilon_1 & \cdots & \epsilon_k & \cdots & \epsilon_{N_C} & 0 \end{array} \right] \quad (6.18)$$

$A_{l,k}$ and C_d^k are $d \times d$ submatrices defined by :

$$A_{l,k} = \frac{\partial \mathbf{f} \left(\sum_{k'=0}^{N_C} \mathbf{a}_{k'} T_{k'}(\tilde{t}_l) \right)}{\partial \mathbf{a}_k} \text{ and } C_d^k = \begin{cases} I_d & \text{if } k \text{ is even} \\ 0_d & \text{if } k \text{ is odd.} \end{cases}$$

I_d , 0_d and 0_{d1} are defined in section 6.2.2. $\boldsymbol{\delta}_l$ and $\boldsymbol{\epsilon}_k$ are respectively column and row vectors in \mathbb{R}^d defined by :

$$\boldsymbol{\delta}_l = -2 \sum_{k=1}^{N_C} k \mathbf{a}_k U_{k-1}(\tilde{t}_l) \text{ and } \boldsymbol{\epsilon}_k = [(-1)^{k+1} k^2, 0, \dots, 0].$$

Computation of the stability of the periodic orbit solution

Once the spectral coefficients \mathbf{a}_k of the orbit and the period T are known, the linear stability of the orbit can be assessed. The procedure is closely related to that used for finite differences. We introduce a small perturbation to the solution :

$$\mathbf{x}'(\tilde{t}) = \sum_{k=0}^{N'_C} \mathbf{a}'_k T_k(\tilde{t}) \quad (6.19)$$

where it is assumed in practice that $N'_C = N_C$. For the perturbation we do not assume periodicity but rather:

$$\mathbf{x}'(1) = \sigma \mathbf{x}'(-1) \quad (6.20)$$

which translates into:

$$\sum_{k=0}^{N_C} \mathbf{a}'_k T_k(1) = \sigma \sum_{k=0}^{N_C} \mathbf{a}'_k T_k(-1) \quad (6.21)$$

which allows for the growth of the perturbation on the orbit with $\sigma \in \mathbb{C}$. The equation (6.20) is rewritten as :

$$\mathbf{x}'(1) - \mathbf{x}'(-1) = \gamma \mathbf{x}'(1) \quad \text{where } \gamma = 1 - \frac{1}{\sigma}. \quad (6.22)$$

The decomposition (6.19) is introduced into the governing equations linearised around the base solution, assuming that \mathbf{a}'_k are small. Evaluation of the resulting equation at the Gauss-Lobatto points yields a generalised eigenvalue problem:

$$\mathbf{J}\mathbf{a}' = \gamma \mathbf{B}\mathbf{a}', \quad (6.23)$$

Thanks to equation (6.22), the matrix \mathbf{J} is directly defined from the jacobian matrix (6.18) computed at the last iteration in Newton-Raphson solver by removing the last row and the last column. The eigenvector is ordered in the following way $\mathbf{a}' = [\mathbf{a}'_0, \mathbf{a}'_1, \dots, \mathbf{a}'_{N_C}]$. The matrix \mathbf{B} of dimension $(N_C + 1)d$ is defined by :

$$\mathbf{B} = \left[\begin{array}{cccc|cc} 0_d & \dots & \dots & \dots & 0_d & 0_d \\ \vdots & \ddots & & & \vdots & \vdots \\ \vdots & & 0_d & & \vdots & \vdots \\ \vdots & & & \ddots & \vdots & \vdots \\ 0_d & \dots & \dots & \dots & 0_d & 0_d \\ \hline I_d & \dots & \dots & \dots & I_d & I_d \end{array} \right]. \quad (6.24)$$

The eigenvalue problem (6.23) has $(N_C + 1) d$ eigenvalues. $(N_C d)$ eigenvalues are infinite and the Floquet multipliers σ can be computed from the d finite eigenvalues γ . The Floquet exponents μ are directly deduced from the Floquet multipliers σ via :

$$\mu = \frac{\log \sigma}{T}. \quad (6.25)$$

The periodic orbit is unstable if $|\sigma| > 1$ ($\text{real}(\mu) > 0$). The main property to exploit is that the eigenvalue problem (6.23) yields *only* d finite Floquet multipliers. This is in contrast to Hill's method that yields $(2N_F + 1) \times d$ finite exponents.

6.3 Examples

In this section several examples of orbits in dynamical systems are presented. The stability of the orbits resulting in real or complex Floquet multipliers is computed using either finite differences approximation, Fourier and Chebyshev spectral expression in time.

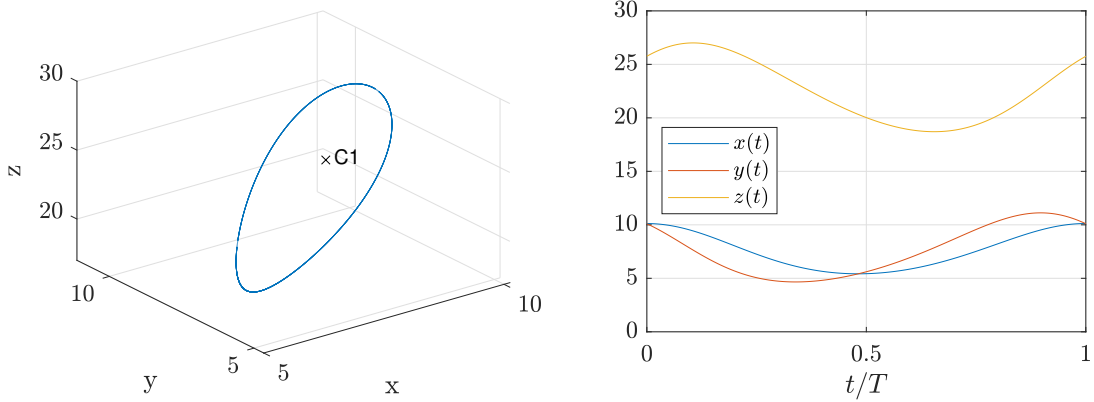


Figure 6.1: The unstable periodic orbit ($T = 0.6793$) for the Lorenz system $\rho = 24$, $s = 10$, $\beta = 8/3$ as a state portrait on the left and in a component-wise representation over one period on the right. A stable fixed point is marked with $C_1 = [\sqrt{\beta(\rho-1)}, \sqrt{\beta(\rho-1)}, \rho-1] = [8.76, 8.76, 23]$. Representation obtained with HBM using $N_F = 20$ modes. $\mathbf{x}(t=0) = (10.12, 10.1, 25.76)$.

6.3.1 Lorenz system

The Lorenz system is a system of three ordinary differential equations:

$$\frac{dx}{dt^*} = s(y - x), \quad (6.26a)$$

$$\frac{dy}{dt^*} = x(\rho - z) - y, \quad (6.26b)$$

$$\frac{dz}{dt^*} = xy - \beta z \quad (6.26c)$$

For $\rho = 24$, $s = 10$, $\beta = 8/3$ the system admits an unstable periodic orbit born in a subcritical Hopf bifurcation at $\rho = 24.74$ of a fixed point C_1 (Lorenz, 1963), shown in figure 6.1.

The stability of the orbit is found using each of the three methods. The resulting spectrum and the convergence of the unstable Floquet exponent are shown in figure 6.2. For the evaluation of the error on the exponents μ_3 and μ_1 it was assumed that the reference exponents are the ones extracted from Hill's matrix for $N_F = 20$:

$$\text{absolute error} = |\mu_\infty - \mu| \quad (6.27)$$

The values of the three Floquet exponents are $(-13.713, 0, 0.0465)$ for a stable, neutral and unstable perturbations, respectively. The value of the reference neutral exponent in equation (6.27) is taken to be exactly 0.

First, as can be seen in figure 6.2, the spectrum associated with Hill's matrix is populated by a large number of spurious eigenvalues, whereas for a three-dimensional ODE system such as the Lorenz system, only three eigenvalues are needed (one of them being necessarily neutral). The three Floquet exponents were correctly identified by the finite differences method and the Chebyshev method. In the absence of any strategy to filter the eigenvalues of Hill's matrix it can be challenging to draw conclusions concerning the orbit's stability.

Moreover, as shown in figure 6.3, the finite differences method is only second order accurate in determining the unstable Floquet exponent, because the approximation of the time derivative and the phase condition are based on a second order accurate scheme. Both HBM and Chebyshev expression are marked with spectral convergence, although a slower one for the case of Chebyshev method for the same number of degrees of freedom.

The advantage of Chebyshev expansion to identify the correct Floquet exponents is balanced by its slower convergence compared to the HBM.

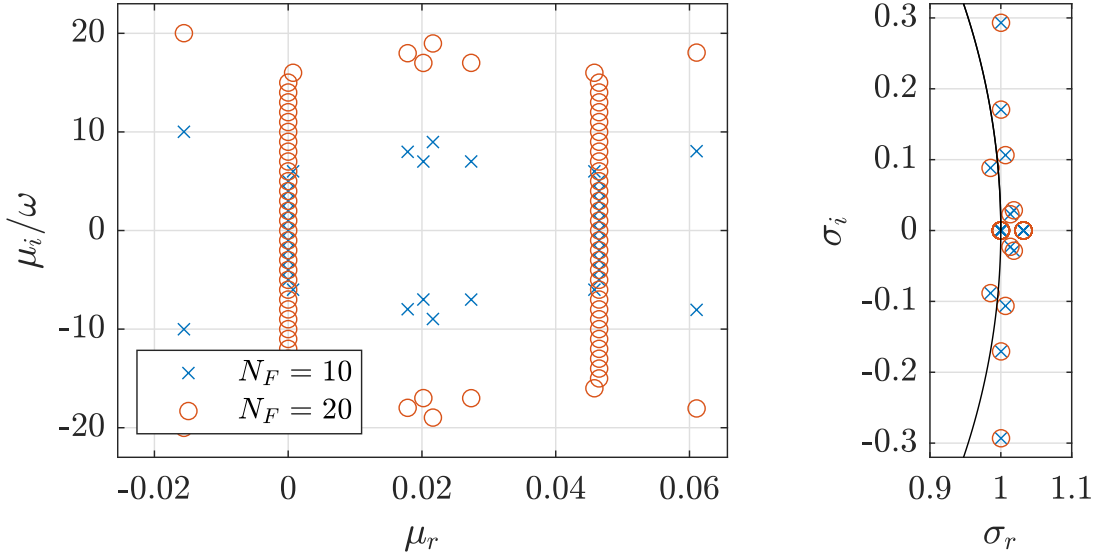


Figure 6.2: Left: Subset of Floquet exponents of the orbit of Lorenz system for ($\rho = 24$, $\mu = 10$, $b = 8/3$) found by Hill's method for $N_F = 10$ and $N_F = 20$. Only the Floquet exponents around $\mu_r = 0.0$ and $\mu_r = 0.0465$ are displayed. The region of the complex plane around $\mu_r = -13.713$ is omitted for clarity. Right: Corresponding Floquet multipliers $\exp(\mu T)$. Hill's method yields a set of exponents that have to be filtered to discard the spurious values.

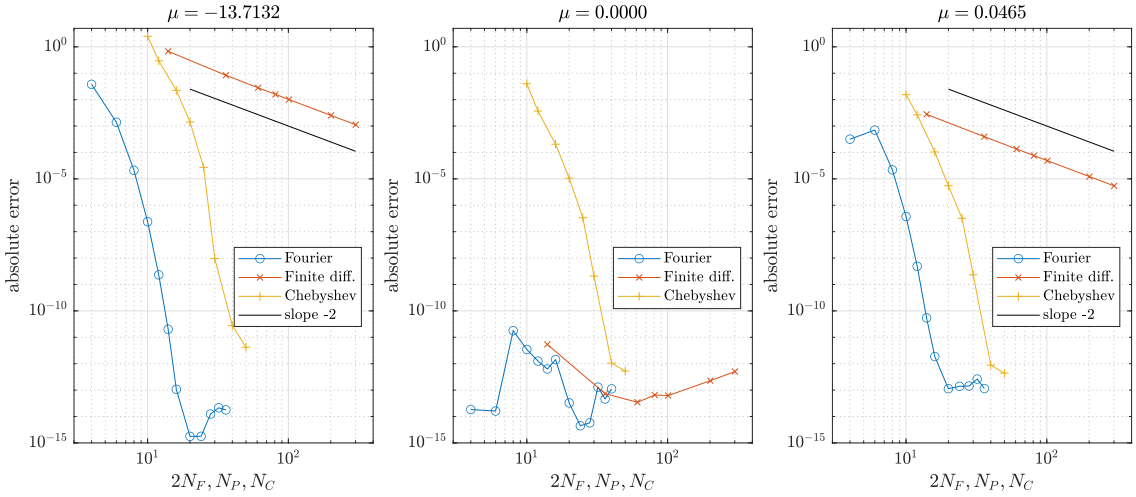


Figure 6.3: Error of three Floquet exponents of an unstable orbit of Lorenz system for $\rho = 24$, $\mu = 10$, $b = 8/3$ computed with Finite Differences, Hill's method (Fourier) and Chebyshev method. Hill's and Chebyshev methods show spectral convergence while Finite Differences show only second order convergence for the non-zero exponents. Results are reported as a function of $2N_F$, N_P and N_C to compare between the same number of degrees of freedom.

N_P	μ_3	μ_2	μ_1	T
13	-1.43895880×10^1	$-3.82750361 \times 10^{-12}$	$4.37157935 \times 10^{-2}$	$6.92268000 \times 10^{-1}$
35	-1.37967351×10^1	$-2.90158308 \times 10^{-14}$	$4.60974317 \times 10^{-2}$	$6.81075444 \times 10^{-1}$
60	-1.37412922×10^1	$1.73082817 \times 10^{-14}$	$4.63577558 \times 10^{-2}$	$6.79926770 \times 10^{-1}$
100	-1.37232514×10^1	$-1.51940104 \times 10^{-13}$	$4.64440859 \times 10^{-2}$	$6.79548972 \times 10^{-1}$
300	-1.37142788×10^1	$-9.08625324 \times 10^{-14}$	$4.64873253 \times 10^{-2}$	$6.79360332 \times 10^{-1}$
N_F	μ_3	μ_2	μ_1	T
2	-1.36751635×10^1	$1.84076530 \times 10^{-14}$	$4.68109907 \times 10^{-2}$	$6.77821008 \times 10^{-1}$
5	-1.37131592×10^1	$-3.46572972 \times 10^{-12}$	$4.64931094 \times 10^{-2}$	$6.79336744 \times 10^{-1}$
10	-1.37131594×10^1	$-3.27490584 \times 10^{-14}$	$4.64927338 \times 10^{-2}$	$6.79336764 \times 10^{-1}$
20	-1.37131594×10^1	$-1.11527694 \times 10^{-13}$	$4.64927338 \times 10^{-2}$	$6.79336764 \times 10^{-1}$
N_C	μ_3	μ_2	μ_1	T
10	-1.62294036×10^1	$-4.00374681 \times 10^{-2}$	$6.19998609 \times 10^{-2}$	$6.80057324 \times 10^{-1}$
12	-1.40070361×10^1	$3.69629048 \times 10^{-3}$	$4.38326708 \times 10^{-2}$	$6.78438981 \times 10^{-1}$
20	-1.37145817×10^1	$1.05768135 \times 10^{-5}$	$4.64872317 \times 10^{-2}$	$6.79336187 \times 10^{-1}$
30	-1.37131594×10^1	$2.07567425 \times 10^{-9}$	$4.64927314 \times 10^{-2}$	$6.79336764 \times 10^{-1}$
50	-1.37131594×10^1	$-5.29505069 \times 10^{-13}$	$4.64927338 \times 10^{-2}$	$6.79336764 \times 10^{-1}$

Table 6.1: Three Floquet exponents and the period of an unstable periodic orbit of Lorenz system for $\rho = 24$, $\mu = 10$, $b = 8/3$. N_P , N_F and N_C correspond respectively to Finite Differences, Hill's method and Chebyshev method. HBM reaches machine precision with only $N_F = 10$ modes, Chebyshev method reaches three significant digits with $N_C = 20$.

The temporal convergence of the unstable Floquet exponent is also listed in Table 6.1. The label N_P corresponds to the number of points used in the orbit in the finite differences method, N_F corresponds to the number of modes used in Hill's method and N_C to the number of modes used in the Chebyshev method.

We test now the convergence of the methods for more demanding parameter values. For $\rho = 28$, $\sigma = 10$, $\beta = 8/3$ the Lorenz system (6.26) admits a chaotic attractor and hence an infinity of unstable periodic orbits (Cvitanovic et al., 2005). The periodic orbit with the smallest period among those identified, labeled AB by Viswanath (2003), is shown in figure 6.4. For this specific orbit, the period found in this reference paper is $T = 1.558652210716$ and the largest Lyapunov exponent is 0.9946. The three Floquet exponents of the orbit are listed in table 6.2 for a range temporal accuracy found both by Hill's method or the Chebyshev method. The results for the finite differences method are not shown in the table 6.2 but the relative error drops below 1% for the period and both nonzero Floquet exponents when N_P is larger than 80.

For a more complex orbit more Chebyshev modes are needed to match the $N_F = 20$ HBM result up to three digits in μ_3 and up to five digits in μ_1 . Here for instance, the required number of Chebyshev modes is $N_C \approx 100$.

The last example of periodic orbit of the Lorenz system is a stable orbit. For $\rho \in (145, 166)$ there is a periodic window (Strogatz, 2018). A stable orbit for $\rho = 160$ is shown in figure 6.4. Its stability properties are listed in table 6.3. The convergence of the Floquet exponents is slow, illustrating the rich tangent dynamics. As expected, for this stable orbit all nonzero exponents are negative. Hill's method with $N_F = 24$ modes achieves four digits of accuracy for all Floquet exponents. Comparable accuracy on μ_2 using the Chebyshev method requests, in comparison, as many as $N_C = 130$ modes.

6.3.2 Langford system

The periodic orbits of the Lorenz system presented so far were either stable or unstable, but always with *real* Floquet multipliers. The question arises whether the Chebyshev expansion can also handle the analysis of orbits, stable or unstable, characterised by *complex* Floquet multipliers. Whenever stability is lost due to a pair of non real Floquet multipliers crossing the unit circle in the complex plane, a Neimark-Sacker bifurcation occurs, leading to additional oscillations on top of the PO. A

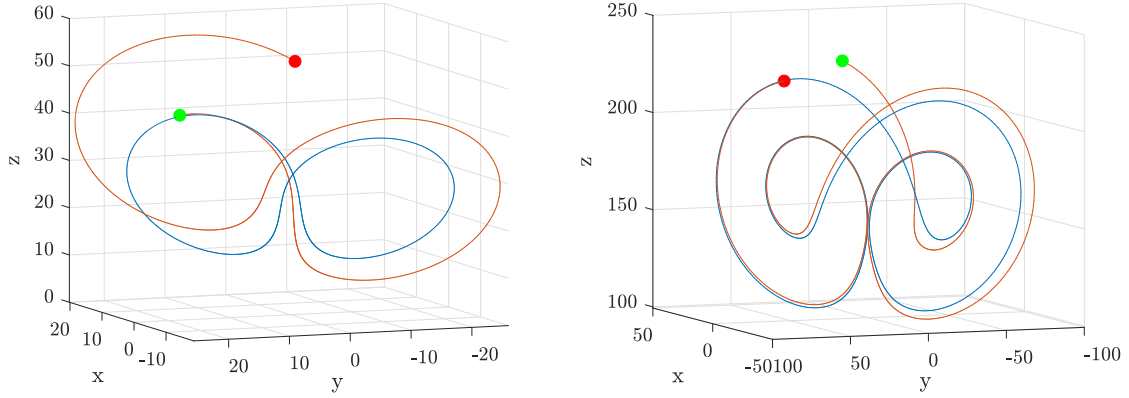


Figure 6.4: Periodic orbit solution of the Lorenz system for $\rho = 28$ ($T = 1.559$) (left) and $\rho = 160$ ($T = 1.153$) (right) in blue, together with an unstable (left panel) or stable (right panel) eigenvector (solid red line) computed with Chebyshev method. Green dot : initial time, red dot : final time after one period.

N_F	μ_3	μ_2	μ_1	T
12	-1.4661×10^1	6.8400×10^{-15}	9.9542×10^{-1}	1.55867856
16	-1.4661×10^1	4.5433×10^{-15}	9.9466×10^{-1}	1.55865243
20	-1.4661×10^1	-1.5859×10^{-14}	9.9465×10^{-1}	1.55865221
N_C	μ_3	μ_2	μ_1	
30	-5.8174	2.7928×10^{-2}	9.8702×10^{-1}	1.55742897
50	-9.4778	2.4579×10^{-3}	9.9497×10^{-1}	1.55867591
70	-1.2319×10^1	5.6688×10^{-5}	9.9466×10^{-1}	1.55865263
90	-1.4419×10^1	1.1593×10^{-6}	9.9465×10^{-1}	1.55865222
110	-1.4694×10^1	-1.5825×10^{-7}	9.9465×10^{-1}	1.55865221

Table 6.2: Three Floquet exponents and period of an unstable periodic orbit of Lorenz system for $\rho = 28$, $\mu = 10$, $b = 8/3$ for HBM/Hill's (N_F) and Chebyshev (N_C) method.

N_F	μ_3	μ_2	μ_1	T
20	-1.2469×10^1	-1.1952	-7.7734×10^{-14}	1.15297839
22	-1.2461×10^1	-1.2055	2.6118×10^{-15}	1.15295801
24	-1.2460×10^1	-1.2060	1.8593×10^{-14}	1.15295091
26	-1.2460×10^1	-1.2067	4.8119×10^{-14}	1.15294951
28	-1.2460×10^1	-1.2068	1.6459×10^{-15}	1.15294907
N_C	μ_3	μ_2	μ_1	
50	-4.1469	-2.5882	-5.3971×10^{-2}	1.15208020
70	-8.9477	-1.1366	2.0596×10^{-3}	1.15282663
90	-1.1745×10^1	-1.1925	9.4145×10^{-4}	1.15293728
110	-1.4232×10^1	-1.2049	1.4470×10^{-4}	1.15294773
130	-1.2577×10^1	-1.2067	1.8836×10^{-5}	1.15294882
150	-1.2474×10^1	-1.2069	2.2549×10^{-6}	1.15294892

Table 6.3: Three Floquet exponents and the period of a stable periodic orbit of Lorenz system for $\rho = 160$, $\mu = 10$, $b = 8/3$ for HBM/Hill's (N_F) and Chebyshev (N_C) method.

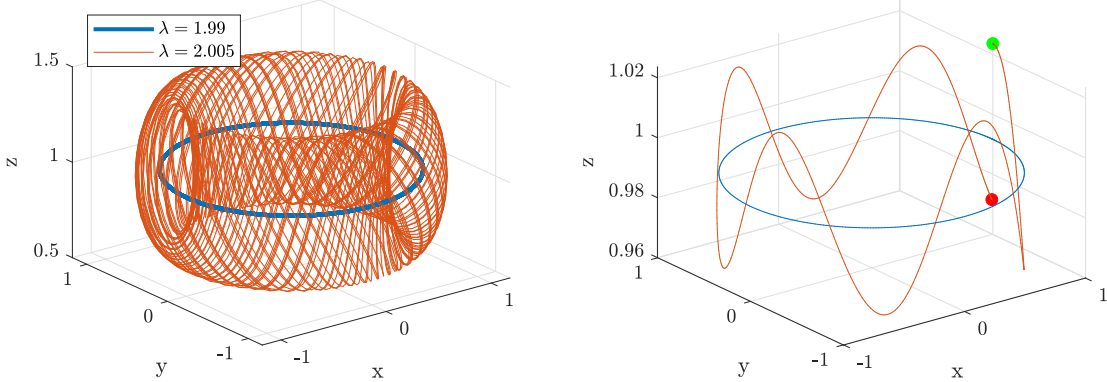


Figure 6.5: Left: trajectory of the Langford system obtained using a time integrator for values of λ below (blue) and above $\lambda_c = 2$ (red). For $\lambda = 1.99$ the trajectory converges asymptotically to the stable perfectly circular periodic orbit. For $\lambda = 2.005$ the trajectory diverges towards a stable torus. Right: the unstable periodic orbit and its eigenvector for $\lambda = 2.005$, obtained using the Chebyshev method. $\mathbf{x}'(t = 0)$ is marked with a green and $\mathbf{x}'(t = 1)$ with a red arrow.

low-dimensional example of such dynamics is the three-dimensional Langford ODE system (Seydel, 2009) given by

$$\dot{x} = (\lambda - 3)x - 0.25y + x(z + 0.2(1 - z^2)) \quad (6.28a)$$

$$\dot{y} = (\lambda - 3)y + 0.25x + y(z + 0.2(1 - z^2)) \quad (6.28b)$$

$$\dot{z} = \lambda z - (x^2 + y^2 + z^2) \quad (6.28c)$$

The system is parametrised by the real parameter λ . For $\lambda > 1.683$, it possesses an exactly circular periodic orbit whose analytical expression is given by

$$x = r \cos(0.25t) \quad (6.29a)$$

$$y = r \sin(0.25t) \quad (6.29b)$$

$$z = 2.5 \left(1 - \sqrt{0.8\lambda - 1.24}\right) \quad (6.29c)$$

with $r = \sqrt{z(\lambda - z)}$. This PO loses stability above $\lambda = 2$. Due to simple analytical expression of the PO it is possible to express analytically its stability exponents as:

$$\mu = \frac{\lambda - 2z + \sqrt{(\lambda - 2z)^2 - 8r(r - 0.4rz)}}{2} \quad (6.30)$$

where z corresponds to the plane in which the circular orbit resides, r to its radius and μ to the complex Floquet exponent of the orbit. At $\lambda = 2$ ($z = 1$, $r = 1$) the orbit loses stability to a complex pair of Floquet exponents $\mu = \pm i\frac{\sqrt{30}}{5}$ and leads to a torus. Both the periodic orbit, the torus and the instability mode computed using the Chebyshev method are shown in figure 6.5. A pair of unstable Floquet exponents depending on the number of temporal modes used is listed in table 6.4. With $N_C = 30$ modes six digits of the real part of the unstable Floquet exponent can be computed accurately. The Chebyshev expansion is hence able to capture the oscillatory bifurcation.

6.4 Differentially Heated Cavity

In order to check the applicability of the Chebyshev expansion in time to a system with a much larger number of degrees of freedom, we consider the case of the flow in an air-filled differentially heated cavity with perfectly conducting horizontal top and bottom boundaries. This configuration was shown experimentally to undergo a transition to unsteadiness for values of the Rayleigh number

N_C	$\mu_{2,3} (\lambda = 2.005)$
18	$2.7143 \times 10^{-2} \pm 1.0810i$
22	$1.1387 \times 10^{-2} \pm 1.1014i$
26	$1.0815 \times 10^{-2} \pm 1.1011i$
30	$1.0810355 \times 10^{-2} \pm 1.1011046i$
exact	$1.0810312 \times 10^{-2} \pm 1.1011045i$

Table 6.4: Unstable Floquet exponent for the Langford system for $\lambda = 2.005$. The row labelled *exact* corresponds to the analytical value of the exponent calculated using (6.30).

$Ra = \frac{\rho\beta\Delta TH^3}{\nu\alpha}$ around $\approx 3 \times 10^6$ (Briggs and Jones (1985)). It was much used in the late eighties as a test case to predict numerically the transition to unsteadiness. Numerical algorithms of different nature have converged to provide an accurate critical value corresponding to the loss of stability of the steady solution at $Ra_c \approx 2.108 \times 10^6$ (Winters (1987); Gelfgat and Tanasawa (1994); Xin and Le Quéré (2001)). Numerical simulations of the unsteady equations, reported in Le Quéré (1994), showed that the nonlinear unsteady solutions above Ra_c belong to different branches of solutions according to their oscillation period (see figure 5 therein) and that the first branch of time-periodic solutions born at Ra_c loses its stability at a value of Ra around 7×10^6 . This flow configuration thus constitutes a good candidate to test the applicability of algorithms aimed at computing the instability of periodic solutions of the Navier-Stokes equations.

6.4.1 Governing equations and numerical methods

The system is governed by the Navier-Stokes equations under the Boussinesq approximation:

$$\frac{\partial \mathbf{u}}{\partial t} + (\mathbf{u} \cdot \nabla) \mathbf{u} = -\nabla p + \frac{Pr}{\sqrt{Ra}} \nabla^2 \mathbf{u} + Pr\theta \mathbf{e}_y \quad (6.31a)$$

$$\frac{\partial \theta}{\partial t} + (\mathbf{u} \cdot \nabla) \theta = \frac{1}{\sqrt{Ra}} \nabla^2 \theta \quad (6.31b)$$

$$\nabla \cdot \mathbf{u} = 0 \quad (6.31c)$$

with $Pr = 0.71$. The square cavity is shown in figure 6.6 together with the boundary conditions. For the sake of brevity we refer to Xin and Le Quéré (2001) for a more detailed presentation of the physical and dimensionless parameters.

The cavity is discretised with a Finite Volume method using $N_x \times N_y = 128 \times 128$ cells resulting in $O(4N_x N_y) \approx 65\,000$ degrees of freedom. The details on the Finite Volume discretisation of the governing equations can be found in Faugaret et al. (2022). To account for the existence of thin boundary layers along the walls, non-uniform grids in x and y are used, the cell boundaries being distributed as :

$$x_i = 0.5 (1 - \cos(i\pi/N_x)) \quad i = 0, 1, \dots, N_x \quad (6.32)$$

$$y_j = 0.5 (1 - \cos(j\pi/N_y)) \quad j = 0, 1, \dots, N_y \quad (6.33)$$

The steady base flow is found using a Newton-Raphson method. Its linear stability is computed by forming an eigenvalue problem and solving it numerically using ARPACK. More details can be found in Gesla et al. (2023).

6.4.2 Stability of the supercritical Hopf branch

The base state for $Ra = 2.2 \times 10^6$ is shown in figure 6.6. At $Ra = Ra_c$ the base flow loses its stability due to a pair of complex conjugate eigenvalues. The Hopf bifurcation is supercritical and gives rise to a stable periodic orbit. To trace out the amplitude of the cycle born at Ra_c , an observable linked to vorticity is monitored. We use the L_2 -norm of the z -component of the vorticity perturbation

$$\|\omega_{pert}\| = \sqrt{\int |\omega - \omega_b|^2 dx dy}, \quad (6.34)$$

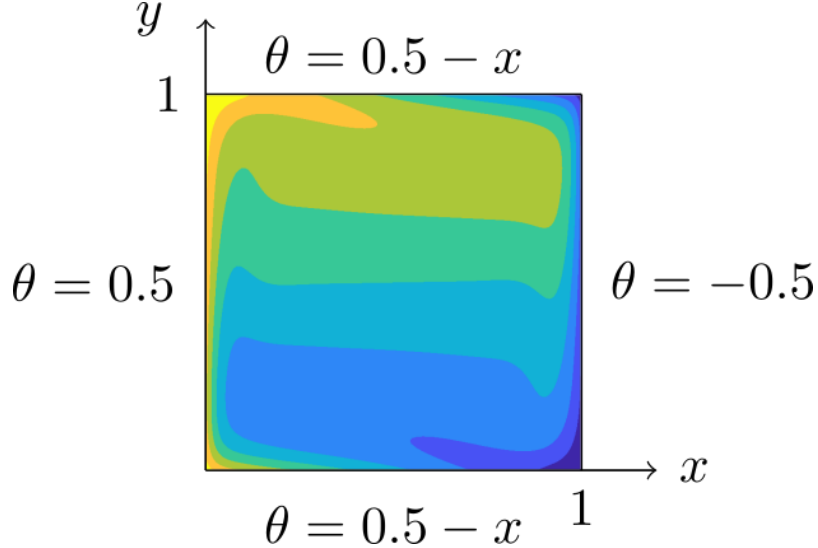


Figure 6.6: Square differentially heated cavity with perfectly conducting top and bottom walls. Temperature θ field of the base flow at $Ra = 2.2 \times 10^6$ together with the boundary conditions. No slip conditions is assumed at the walls. The colormap spans the interval (-0.5,0.5) uniformly with 8 distinct colors.

Ra	μ	$ e^{\mu T} $
5.0×10^6	$-3.17 \times 10^{-3} \pm 2.33 \times 10^{-1}i$	9.855×10^{-1}
5.5×10^6	$-1.39 \times 10^{-3} \pm 2.32 \times 10^{-1}i$	9.936×10^{-1}
6.0×10^6	$-1.84 \times 10^{-4} \pm 2.32 \times 10^{-1}i$	9.991×10^{-1}
6.5×10^6	$5.64 \times 10^{-4} \pm 2.32 \times 10^{-1}i$	1.003
7.0×10^6	$9.52 \times 10^{-4} \pm 2.32 \times 10^{-1}i$	1.004

Table 6.5: Evolution of the leading Floquet exponent and multiplier of the periodic branch in the differentially heated cavity computed with Chebyshev method ($N_C = 26$). The loss of stability occurs for Ra in between 6×10^6 and 6.5×10^6 . Interpolated value : $Ra_{NS} = 6.12 \times 10^6$.

where $\omega = \partial_x u_y - \partial_y u_x$ is the z -component of the vorticity, ω_b is the equivalent quantity for the base flow and $\omega_{pert} = \omega - \omega_b$. The temporal root-mean-square value of $\|\omega_{pert}\|$ is denoted A .

A bifurcation diagram is shown in figure 6.7 reporting A as a function of Ra . The stability of the supercritical branch is investigated using the Chebyshev expansion in time with $N_C = 26$ Chebyshev polynomials. The evolution of the most unstable Floquet exponents pair with increasing Ra is listed in table 6.5. It shows that the periodic orbit loses its stability to a pair of complex conjugate Floquet exponents in a Neimark-Sacker bifurcation slightly above $Ra = 6 \times 10^6$, thereby confirming the result by Le Quéré (1994).

Table 6.6 provides a comparison of the convergence of the Floquet exponent as a function of the number of degrees of freedom retained either for HBM or Chebyshev expansion for two values of Ra . Two correct digits of the real part of a Floquet exponent and five correct digits of the period can be computed with $N_C = 30$ Chebyshev modes at $Ra = 5 \times 10^6$.

6.5 Summary

The present work suggests a new numerical method to compute periodic solutions of multi-dimensional systems of ordinary differential equations together with their stability characteristics. The method is inspired by the classical Harmonic Balance method (HBM) where the sought periodic orbit is expanded on a basis of Chebyshev polynomials in time rather than Fourier harmonics. Whereas Hill's method coupled with HBM method is known to yield many spurious Floquet exponents, the method based on Chebyshev polynomials outputs a spectrum devoid of spurious modes. No sorting of the

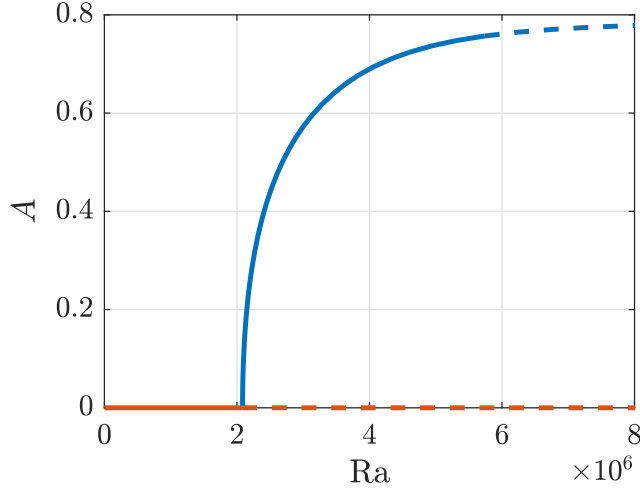


Figure 6.7: Bifurcation diagram for a square differentially heated cavity. Branch of the base flow solution is stable for $Ra_c < 2.108 \times 10^6$ (red solid line) and unstable above Ra_c (red dashed line). Supercritical Hopf branch emanating from Ra_c is stable for $Ra_{NS} < 6.1 \times 10^6$ (blue solid line) and unstable above Ra_{NC} (blue dashed line).

	μ	T
$N_F = 5$	$-2.2585 \times 10^{-3} \pm 2.3229 \times 10^{-1}i$	4.60294436
$N_F = 8$	$-3.1232 \times 10^{-3} \pm 2.3275 \times 10^{-1}i$	4.60715822
$N_F = 10$	$-3.1425 \times 10^{-3} \pm 2.3279 \times 10^{-1}i$	4.60701887
$N_C = 20$	$-2.990 \times 10^{-3} \pm 2.3257 \times 10^{-1}i$	4.60714417
$N_C = 30$	$-3.156 \times 10^{-3} \pm 2.3280 \times 10^{-1}i$	4.60701275
$N_C = 40$	$-3.14436 \times 10^{-3} \pm 2.3278422 \times 10^{-1}i$	4.60700519
$N_C = 50$	$-3.14469 \times 10^{-3} \pm 2.3278436 \times 10^{-1}i$	4.60700485

Table 6.6: Convergence study for the least stable Floquet exponent and the period of the stable orbit of the differentially heated cavity obtained with HBM/Hill's method (N_F) and Chebyshev method (N_C). $Ra = 5 \times 10^6$.

correct exponents is therefore required. Drawbacks include slower spectral convergence, since faster convergence of the orbit expressed with Fourier series is in connection to its intrinsic periodicity. However, there are orbits for which the Chebyshev expansion can become an advantage. In the case of a periodic orbit with a long plateau the Chebyshev expansion would benefit from the non-uniform distribution of the Gauss-Lobatto points along the orbit. Still, the phase condition should be adapted so that abrupt changes, for instance close to a saddle-loop bifurcation (Gaspard, 1990), match the clustering of collocation points. The method was tested on several stable or unstable periodic orbits of the Lorenz system, on a Neimark-Sacker bifurcation in the Langford system, as well as on a two-dimensional cavity flow governed by the incompressible Navier-Stokes equations. This demonstrates the potential of the method for the Floquet analysis of time-periodic solutions of large-scale systems such as those coming from the discretisation of PDEs. The implementation of the Chebyshev expansion in time using collocation method on an existing PDE steady-state solver to find periodic orbits and their stability is straightforward. The continuous variable time is handled exactly as any variable varying in space. When dealing with stability, only a matrix (denoted \mathbf{B}) has to be additionally set-up for the generalised eigenvalue problem. A suggested usage of the method on smooth periodic orbits is coupling with HBM. Chebyshev modes could be used as a complement to Hill's method, by allowing to select the meaningful exponents, while retaining high spectral accuracy of the description of the orbit. A more rigorous theoretical justification of these advantageous properties would now be welcome. It is also possible to envision other alternative spectral expansions using other polynomial bases or piecewise polynomials.

Chapter 7

Summary

In this work the axisymmetric rotor-stator flow has been revisited, with the aim to explain the dynamical origin of the chaotic rolls reported in experiments and numerics. Former works by other authors suggested that the rolls could be a direct response of the rotor-stator system to imperfections inherent to the experiments, such as noise or permanent disturbances. A second possible scenario explaining the circular rolls could involve a self-sustained solution independent of the external forcing. Both alternatives were studied in this work.

In the first part of the thesis, we adopted the point of view of bifurcation theory and looked for nonlinear branches of *self-sustained* solutions. The various branches of nonlinear solutions found contribute to a better global picture of the axisymmetric dynamics. It was shown using standard linear stability analysis that the axisymmetric base flow loses stability at a finite Reynolds number $Re_c \approx 2900$. At Re_c a Hopf branch of supercritical solutions emerges. This branch, difficult to continue numerically, was successfully captured using a Harmonic Balance Method initialised by Self-Consistent Method, a method free from the use of timesteppers. The associated branch and its folds appear in all cases restricted to a very narrow $O(1)$ interval of values of Re , and does not explain the subcriticality of the chaotic rolls.

Even though the bifurcation from the base flow appears supercritical, subcritical branches of axisymmetric finite-amplitude solutions have been identified. One of them is a branch of exactly periodic solutions, the other one is a branch of edge states separating the laminar and turbulent regimes. These two branches appear connected through a bifurcation scenario to be determined. They are unstable and exist down to $Re = Re_{SN} \approx 1800$. On one hand, this value of Re_{SN} is about 40% lower than the critical Reynolds number Re_c , which justifies the existence of subcritical rolls at least within this Re -interval. On the other hand, this value of Re_{SN} is not low enough to explain the experimental observations.

The branches of axisymmetric solutions found in the present work are summarised in the bifurcation diagram of Figure 7.1. The solutions from the Hopf branch, initially believed to be important for the subcritical dynamics, are restricted to a very narrow interval. They do not appear clearly connected to the other solutions and were not found to contribute to the origin of the chaotic rolls. The dynamical connections between the other different states found in this work are conjectured as relatively simple. The periodic subcritical states appear, upon increasing Re , in a saddle-node bifurcation. They do not bifurcate from the base flow, at least not in the range of Re investigated. The edge state branch results from one (or several) bifurcation(s) of the lower-branch of periodic subcritical states. The edge state is finally connected directly to the chaotic rolls via its linear instability. The fact that the whole subcritical dynamics appears fully disconnected dynamically from the base flow is common in open shear flows, it was also reported in rotor-stator flow for $\Gamma = 5$ (Lopez et al., 2009), for which no axisymmetric instability of the base flow was identified. The presence for $\Gamma = 10$ of a critical point with a linear stability apparently leaves this picture unchanged. A radical difference between $\Gamma = 5$ and 10 is the more complex dynamics observed for higher Γ . This is consistent with the qualitative sketch that wave-like perturbations, once born in the corner/shroud

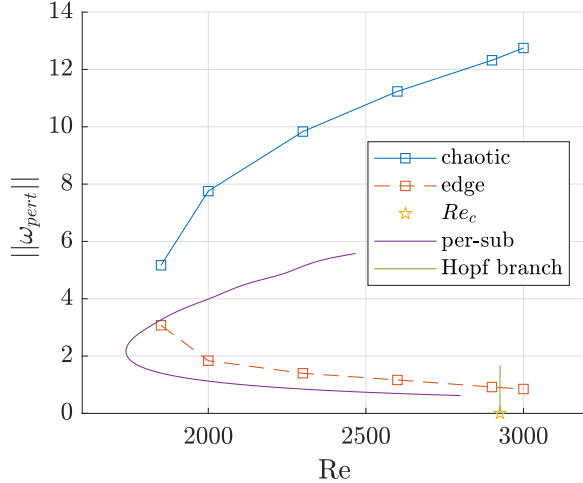


Figure 7.1: Summary bifurcation diagram $a(Re)$. Three different branches are shown : edge state branch together with the chaotic branch (red/blue squares), periodic-subcritical branch (purple solid line), and the Hopf branch arising at Re_c (green solid line). Spatial resolution R0.

region, are advected radially inwards along the stator, and that the further they can travel from their origin, the more they get amplified and the more chaotic they become.

The second part of the thesis focused more on the noise-sustained response of the flow. Both linear and nonlinear receptivity theories were invoked to investigate how the flow responds to an additive forcing of external origin. Several types of forcing were considered, each with its pros and cons. Forcing applied to the bulk of the fluid lends itself well to linear optimal response theory (Schmid and Brandt, 2014). If a wide frequency spectrum is forced, pseudo-resonance linked with non-normal effects (Trefethen and Embree, 2005) will amplify more the frequencies contained in the large hump in the gain curve in fig. 5.7. Such frequencies invariably lead to circular rolls inside the Bödewadt layer developing along the stator. Forcing applied through motion of the boundaries is by design not optimal, however it is more realistic in the case of closed flows, and can easily be extended to a nonlinear framework. Increasing the amplitude of the forcing at high enough Re unambiguously leads to a different, more complex nonlinear state which coexists with the simpler forced base flow. Although both states are characterised by circular rolls on the stator, we argue that the rolls reported in the experiments of Schouveiler et al. (2001) are a linear response to external forcing and not a self-sustained state. This is consistent with the observation that these rolls disappear rapidly should the forcing be suddenly turned off (Lopez et al., 2009; Do et al., 2010). Moreover a particularly striking match with the experiment of Schouveiler et al. (2001) was found when the forcing features only harmonics of the rotor's main angular frequency, with complex features such as the pairing and merging of vortices well reproduced numerically. The circular rolls observed experimentally can hence be described as noise-sustained, with the subtlety that they are not the response to incoherent noise but rather to a forcing with well-organised frequency content typical of rotating machinery.

The current results clarify the global picture for the transition to chaos in axisymmetric rotor-stator flow. Branches of nonlinear invariant solutions exist in the range $Re = 1800 - 3000$ and were identified numerically using various techniques. Whether stable or unstable, they have little connection to experimentally observed rolls observed experimentally for $Re = 200$. The exact numerical values for the thresholds of each interval are indicative but were found to depend moderately on the numerical resolution. The general picture is independent of the mesh resolution. The Re -range can hence be conceptually divided into four separate regions as in Figure 7.2 :

- I - ($0 \leq Re \lesssim 200$) The base flow is stable and no asymmetric sustained instability mode can occur neither in the experiments nor in the numerics.
- II - ($Re = 200 - 1800$) The flow is stable both linearly and nonlinearly to axisymmetric

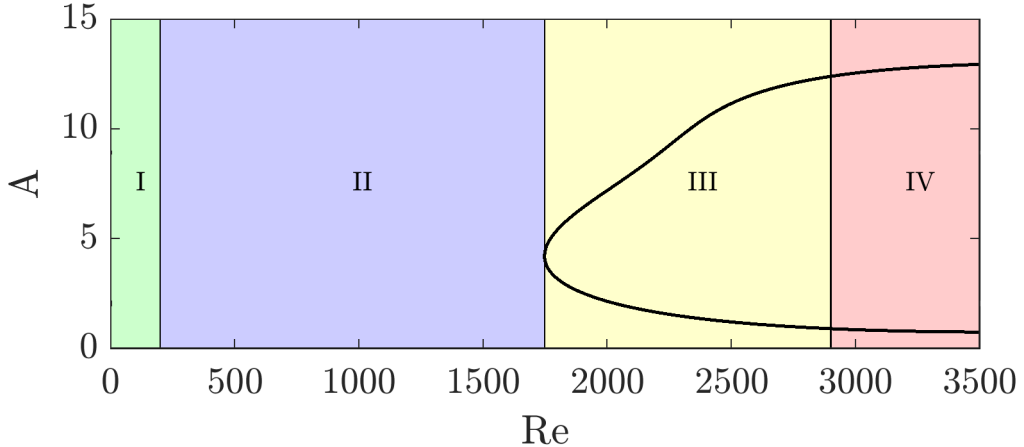


Figure 7.2: Conclusion sketch from this study. Four different dynamical regions for axisymmetric rolls have been identified : I) unconditionally stable base flow, II) the base flow is stable but rolls appear as response to external forcing, III) the base flow is only linearly stable but unstable to some finite-amplitude perturbations, chaotic rolls can be sustained without forcing and IV) chaotic rolls are sustained by the linear instability of the base flow. The solid black lines denotes finite-amplitude solutions described in this paper.

perturbations. Sustained axisymmetric rolls can be observed in the experiments, but only as the result of continuous forcing by external perturbations. If such a forcing disappears, the flow relaminarises. Some unstable or stable solutions with small attraction basin may exist but have not been found and, if any, are believed to play limited role in the dynamics.

- III - ($1800 \lesssim Re \lesssim Re_c \approx 3000$) High-amplitude branches of self-sustained solutions exist and contribute to the formation of a chaotic set, possibly a chaotic attractor. Although the base flow is still linearly stable, strong enough perturbation can trigger chaotic rolls in the flow, linked to the existence of high-amplitude solutions. For infinitesimally small disturbance levels the system still responds to external excitations as if there were no finite-amplitude solutions.
- IV - ($Re > Re_c \approx 3000$) The base flow is linearly unstable to axisymmetric perturbations. Infinitesimal perturbations to that base flow lead to unsteady rolls.

Outlooks

The current work presented many concepts and scenarios of developing unsteadiness in a rotor-stator flow. Even though the question of the origin of the circular rolls in a rotor-stator flow is now believed to be clarified, many of the observed phenomena were only briefly reported and not studied in depth. This opens up many possibilities of continuing the present work. Since the amount of possible extensions of this project is vast, they will be presented in the order corresponding to the increasing Re .

At the lowest Re , corresponding to the region I in figure 7.2, the response to the external forcing and the optimally forced structures in the flow were studied. A question of fundamental interest would concern the highest values of Re at which there is no amplification of the forcing. Such Re would correspond to no amplification of the forcing and would be an interesting lower threshold, even though it would be probably too low to correspond to any value reported in the other studies.

The response of the flow to the external forcing presented in the current work concerns the continuous external forcing. New insights into the flow dynamics could be gained by conducting a similar study but with the perturbation of only the initial condition. this could help investigate the connection between the continuous forcing and the initial perturbation. Are the $O(10^2)$ gains reported in this work for optimal continuous forcing at $Re \approx 200$ also found when the optimal perturbation is

introduced in the flow only in the initial condition? Even though the continuous forcing as presented in the work is probably more applicable when a comparison with an experiment is concerned, an optimal seed study as suggested above could be interesting from a fundamental point of view.

Concerning the continuous time forcing more should be understood about the $\omega = 0$ forcing. Is it directly connected to an impulsive discontinuous time forcing? Can the steady forcing be understood as an ensemble effect of the nonlinear interactions influencing the mean flow? It could be then understood as the ingredient of the shift mode of the flow, so the mean flow with the base flow subtracted. Such analysis will involve a nonlinear receptivity theory as in (Rigas et al., 2021).

As for now, only forced simulations concerned forcing the flow using either forcing vector \mathbf{f} in the bulk or by temporally modifying the boundary condition at the rotor and the shroud. A question arises whether the temporal alteration of the boundary condition is directly corresponding to a temporal modulation of the Re , and in consequence the viscosity of the fluid. In short, whether the modulation of rotating speed of the disc is, after proper rescaling, directly corresponding to some modulation of fluid viscosity while keeping the rotation rate constant. If so, is the modulation of fluid viscosity of the same character (e.g. harmonic)? A separate study possibly concerning a simpler set-up (e.g. lid driven cavity) could answer this question.

A big challenge in studying the rotor-stator geometry is the large number of parameters that characterise it. Many studies, including this one, fix the aspect ratio, the boundary condition on the shroud and the presence of the hub throughout the analysis to avoid the necessity of analysing a large parameter space. This naturally raises a question of generalisability of results. Here only the most important issues concerning the different parameters' influence will be discussed.

Firstly, most results of the response to the external forcing were presented for the set-up with rotating shroud, except for the comparison with the experimental results of Schouveiler et al. (2001), where the shroud was fixed. The exact role of the boundary condition of the shroud should be studied in more detail. Concerning the results of this work it is believed that the shroud boundary condition has limited influence on the optimal forced structure and response to the forcing at $Re \approx 200$ but could have much more influence of the linear instability threshold ($Re \approx 3000$ for $\Gamma = 10$). Concerning the experimental comparison it was stated that the harmonic forcing is responsible for the pairing and merging of the rolls. A quite idealistic scenario of forcing with all harmonics of equal amplitude was considered. The effect of changing the forcing amplitude depending on the frequency could also be investigated. Input data for the amplitudes could come from a careful experimental measurement. It is noted here that even if Schouveiler et al. (2001) observed pairing or rolls in the set-up with fixed shroud, Gauthier et al. (1999) did not observe the same for a set-up with rotating shroud and $\Gamma \approx 20$.

Secondly, the effect of the aspect ratio Γ of the cavity on the linear instability threshold remains largely uninvestigated. A few computations, undocumented in this manuscript, were conducted in the scope of this project and they showed that: i) the critical Reynolds number base of the disc radius $Re_R = Re\Gamma^2 \approx 3 \times 10^5$ is approximately constant for the aspect ratios $\Gamma \approx 5 - 20$ and ii) the imaginary part of the eigenvalue responsible for the loss of stability is always approximately $\lambda_i = 2$. The first point would mean that for the $\Gamma = 5$ the threshold for the linear stability was missed by Lopez et al. (2009), who reports no linear stability threshold for the $Re_R < 10^5$.

The study of the effect of the presence of a hub, as for example in Poncet et al. (2009), is beyond the scope of this work.

Concerning the base flow, chapter 3 emphasized the importance of a stability analysis of the 2D flow field instead of 1D self-similar profile. Still the connections between the absolute/convective instability results of a self-similar profile and the temporal stability of a 2D field could be investigated. A study in the spirit of (Lingwood, 1997) and (Serre et al., 2004) could be proposed. The flow can be assumed locally parallel and the Bers-Briggs method (Briggs et al., 1964; Bers, 1983) could be used to identify locally convective or absolute instability. Instead of using the self-similar profile for the calculation of dispersion relations the velocity profiles extracted from 2D computation would be used. In this way the local analysis would not assume incorrectly the validity of the self-similar profile in the whole cavity. A possible outcome could be that the stator and possibly rotor layers

are convectively unstable to the axisymmetric modes but region of an absolute instability exists only at high $Re \approx 3000$ in agreement with global stability analysis, as performed in current work and in (Daube and Le Quéré, 2002).

The flow in a cavity of $\Gamma = 5$ is interesting in itself and requires a separate study. Computations conducted in the scope of the project, but undocumented in this work, have shown that in the $\Gamma = 5$ cavity, similarly to the $\Gamma = 10$ cavity, there exists a branch of subcritical solutions not originating from the point of linear instability. Those solutions were continued using the time integration and edge tracking technique to discover a saddle node bifurcation. The dynamics of the system was shown to be periodic on the top branch just past the saddle node bifurcation. Can the periodic solution from the top branch be continued using the Harmonic Balance Method and be shown to bifurcate from the base flow? Is the supertransient dynamics also present in cavities of different aspect ratio than $\Gamma = 10$? How does a periodic solution on the top branch evolve into the chaotic dynamics at higher Re ? All of those question require more investigation.

A renewed interest in the $\Gamma = 10$ cavity was sparked by an analysis of the paper by Daube and Le Quéré (2002), which has shown the existence of the top branch chaotic solutions in the flow. The internship of Sleimi (2018) uncovered the existence of the supertransients in the vicinity of the saddle node bifurcation. Those supertransients are reported in this work, although very briefly. More effort should be made to understand how the mean lifetime of the chaotic rolls depends on the Re . Is this dependence superexponential, like in pipe flow (Avila et al., 2010)? The memoryless process underlying supertransients in the rotor-stator flow was also not studied in depth. Closer investigation of lifetime statistics, as in figure 5.17, would reveal that the CDF of lifetimes is exponential only at high enough Re . At $Re = 1800$ the process does not seem to be fully memoryless but this direction was not pursued further.

One of the motivations behind studying the rotor-stator flow is that the supertransient dynamics could be observed in an axisymmetric system (smaller in terms of discretised degrees of freedom than other shear flows) and in the closed set-up (closed flow does not require imposing a periodic boundary condition). Not much is however understood about the how leaky attractor is formed in this particular flow and what structures tend to be characterised by long or short lifetime. Its formation includes probably a boundary crisis (Avila et al., 2013), since the lifetimes have to become infinite for $Re > Re_c$. It could be possible that perturbations, whose spatial support intersects with this of the chaotic attractor at higher Re lead to significantly higher lifetimes than perturbations located at the axis or at the shroud. It is not guaranteed that such claims could be proven considering the fractal structure of the set of initial conditions characterised by a certain lifetime (Skufca et al., 2006). It is true however that any investigation will be simplified by the fact that the flow is axisymmetric, as this is guaranteed to lead to discretised system of smaller number of degrees of freedom than in fully 3D flows.

The biperiodic edge state characterised in this work also motivates new research directions. Its connection to the exactly periodic solutions found for the same Re is not clear. It is possible that one of the building blocks of the edge state is a solution lying on the periodic subcritical branch? The exact match of the frequencies, as reported in the chapter 4 suggest so. Could more periodic solutions be found in the flow? Maybe some of them could be also shown to be related, by a series of bifurcations, to the edge state.

The stability of the exactly periodic solutions characterised in this work was also not investigated in detail. It was only found, using a initialisation of the initial conditions exactly on the branch, that the solutions on the periodic-subcritical branch are unstable. Solutions on the supercritical Hopf branch have to be stable at the onset but the stability properties can change following many folds of the branch and corresponding bifurcations. The algorithms, like introduced in chapter 6, could be used to try to investigate the stability properties of those periodic solutions.

A very interesting insight could be gained by analysing the number of instability directions of the periodic solutions in the flow. If there is only one instability direction, then this is a property shared with the edge state, which has one instability direction by definition. If there is more than one, especially if there is a even number of instability directions, a method of feedback control, like Pyragas method (Pyragas, 1992), could be used to stabilise the periodic solution. The requirement

of the even number of instability directions was initially believed to be necessary condition for a successful stabilisation, but was later proven to only facilitate the control greatly by Fiedler et al. (2007), without being necessary. Few initial simulations, undocumented in the manuscript, were conducted using Pyragas control to stabilise the solutions lying on the periodic-subcritical branch but were not successful. No detailed parametric study was done however.

The Hopf branch emanating from the critical point could also be analysed to find its stability along the branch. Many folds reported on the branch are reminiscent of the snaking phenomenon (Burke and Knobloch, 2007) although this direction was not pursued further.

One more observation, that should be deeply investigated, is the sensitivity of the spectrum to the forcing with a Reynolds stress term based on a least stable eigenvector as used in the Self-Consistent Method and described in chapter 4. The branch of periodic-subcritical solutions was discovered because of the sensitivity of one specific eigenvalue to such a forcing. Interestingly, other eigenvalues remain largely unaffected. It proved impossible to track the origin of the eigenvalue of the most sensitivity as it emanates from a strongly damped part of the spectrum which cannot be reliably numerically resolved. Understanding the process that makes this specific eigenvalue so sensitive to the forcing could shed new light on the connection between the Hopf branch and periodic-subcritical branch.

Finally, for Re in the vicinity of the linear stability threshold value, more could be understood about the spectrum of the linearised operator. As seen with only one example in the chapter 3 but otherwise undocumented in the manuscript, the eigenvectors of the linearised operator can be characterised by the rolls in the Bödewadt layer but also by structures in the bulk of the cavity reminiscent of the inertial waves and by many other structures present either at the axis, in the Ekman layer or at the shroud.

Rotor-stator flow falls into a broader category of flows exhibiting an inflectional velocity profile. Other examples include von Kármán flow over one rotating disc and a flow over a swept wing. Current results could therefore contribute to understanding a broader class of flows. Supertransients reported in this work are also a common feature with other systems, among them: iterative maps (Waleffe, 2003), dynamical systems (Lorenz system evoked by (Strogatz, 2018)) and 3D shear flows (e.g. in pipe flow (Avila et al., 2010)). Due to the velocity gradient in the radial direction close similarities with stratified flows exist where the angular momentum stratification can be understood in terms of density stratification (Veronis, 1970). These observations continue to promote the scientific interest in the flow in a rotor-stator cavity not only as an idealised case of flows encountered in the industrial applications but also as a model flow to study more fundamental phenomena.

Bibliography

- Allgower, E. L. and Georg, K. (2012). *Numerical Continuation Methods: An Introduction*, volume 13 of *Springer Ser. Comput. Math.* Springer Science & Business Media, Cham.
- Atkinson, K. (1991). *An Introduction to Numerical Analysis*. John Wiley & Sons, New York.
- Avila, K., Moxey, D., De Lozar, A., Avila, M., Barkley, D., and Hof, B. (2011). The onset of turbulence in pipe flow. *Science*, 333(6039):192–196.
- Avila, M., Barkley, D., and Hof, B. (2023). Transition to turbulence in pipe flow. *Ann. Rev. Fluid Mech.*, 55:575–602.
- Avila, M., Mellibovsky, F., Roland, N., and Hof, B. (2013). Streamwise-localized solutions at the onset of turbulence in pipe flow. *Phys. Rev. Lett.*, 110(22):224502.
- Avila, M., Willis, A. P., and Hof, B. (2010). On the transient nature of localized pipe flow turbulence. *J. Fluid Mech.*, 646:127–136.
- Batchelor, G. K. (1951). Note on a class of solutions of the Navier-Stokes equations representing steady rotationally-symmetric flow. *Q. J. Mech. Appl. Math.*, 4:29–41.
- Bayer, F. and Leine, R. I. (2023). Sorting-free Hill-based stability analysis of periodic solutions through Koopman analysis. *Nonlinear Dyn.*, 111(9):8439–8466.
- Beneitez, M., Duguet, Y., and Henningson, D. S. (2020). Modeling the collapse of the edge when two transition routes compete. *Phys. Rev. E*, 102(5):053108.
- Bengana, Y., Loiseau, J.-C., Robinet, J.-C., and Tuckerman, L. (2019). Bifurcation analysis and frequency prediction in shear-driven cavity flow. *J. Fluid Mech.*, 875:725–757.
- Bengana, Y. and Tuckerman, L. S. (2021). Frequency prediction from exact or self-consistent mean flows. *Phys. Rev. Fluids*, 6:063901.
- Bers, A. (1983). Space-time evolution of plasma instabilities-absolute and convective. In *Basic plasma physics. 1*.
- Bertolotti, F. P., Herbert, T., and Spalart, P. R. (1992). Linear and nonlinear stability of the Blasius boundary layer. *J. Fluid Mech.*, 242:441–474.
- Bottin, S. and Chaté, H. (1998). Statistical analysis of the transition to turbulence in plane Couette flow. *Eur. Phys. J. B*, 6:143–155.
- Boyd, J. P. (2001). *Chebyshev and Fourier Spectral Methods*. Courier Corporation, Mineola, New York.
- Brady, J. F. and Durlofsky, L. (1987). On rotating disk flow. *J. Fluid Mech.*, 175:363–394.
- Briggs, D. and Jones, D. (1985). Two-dimensional periodic natural convection in a rectangular enclosure of aspect ratio one. *J. Heat Transfer*.
- Briggs, R. J. et al. (1964). *Electron-stream interaction with plasmas*, volume 187. MIT press Cambridge, MA.

- Brynjell-Rahkola, M., Shahriari, N., Schlatter, P., Hanifi, A., and Henningson, D. S. (2017). Stability and sensitivity of a cross-flow-dominated Falkner–Skan–Cooke boundary layer with discrete surface roughness. *J. Fluid Mech.*, 826:830–850.
- Burke, J. and Knobloch, E. (2007). Homoclinic snaking: structure and stability. *Chaos*, 17(3).
- Cerqueira, S. and Sipp, D. (2014). Eigenvalue sensitivity, singular values and discrete frequency selection mechanism in noise amplifiers: the case of flow induced by radial wall injection. *J. Fluid Mech.*, 757:770–799.
- Chomaz, J. M. (2005). Global instabilities in spatially developing flows : Non-normality and nonlinearity. *Ann. Rev. Fluid Mech.*, 37(1):357–392.
- Cochelin, B. and Vergez, C. (2009). A high order purely frequency-based harmonic balance formulation for continuation of periodic solutions. *J. Sound Vib.*, 324(1-2):243–262.
- Cvitanovic, P., Artuso, R., Mainieri, R., Tanner, G., Vattay, G., Whelan, N., and Wirzba, A. (2005). Chaos: classical and quantum. *ChaosBook.org (Niels Bohr Institute, Copenhagen 2005)*, 69:25.
- Daube, O. and Le Quéré, P. (2002). Numerical investigation of the first bifurcation for the flow in a rotor-stator cavity of radial aspect ratio 10. *Comput. Fluids*, 31:481–494.
- Do, Y., Lopez, J. M., and Marques, F. (2010). Optimal harmonic response in a confined Bödewadt boundary layer flow. *Phys. Rev. E*, 82(3):036301.
- Doedel, E., Paffenroth, R., Champneys, A., Fairgrieve, T., Kuznetsov, Y., Sandstede, B., and Wang, X. (2001). AUTO 2000: Continuation and bifurcation software for ordinary differential equations (with HomCont). Technical report, Caltech.
- Duguet, Y., Pringle, C. C., and Kerswell, R. R. (2008a). Relative periodic orbits in transitional pipe flow. *Phys. Fluids*, 20(11).
- Duguet, Y., Schlatter, P., and Henningson, D. S. (2009). Localized edge states in plane Couette flow. *Phys. Fluids*, 21(11).
- Duguet, Y., Willis, A., and Kerswell, R. (2010). Slug genesis in cylindrical pipe flow. *J. Fluid Mech.*, 663:180–208.
- Duguet, Y., Willis, A. P., and Kerswell, R. R. (2008b). Transition in pipe flow: The saddle structure on the boundary of turbulence. *J. Fluid Mech.*, 613:255–274.
- Eckhardt, B. (2018). Transition to turbulence in shear flows. *Phys. A: Stat.*, 504:121–129.
- Escudier, M. (1988). Vortex breakdown: observations and explanations. *Prog. Aerosp. Sci.*, 25(2):189–229.
- Fabre, D., Sipp, D., and Jacquin, L. (2006). Kelvin waves and the singular modes of the Lamb–Oseen vortex. *J. Fluid Mech.*, 551:235–274.
- Fairgrieve, T. F. and Jepson, A. D. (1991). OK Floquet multipliers. *SIAM J. Numer. Anal.*, 28(5):1446–1462.
- Farazmand, M. (2016). An adjoint-based approach for finding invariant solutions of Navier–Stokes equations. *J. Fluid Mech.*, 795:278–312.
- Faugaret, A. (2020). *Influence of air-water interface condition on rotating flow stability : experimental and numerical exploration*. PhD thesis, Sorbonne Université, Paris, France.
- Faugaret, A., Duguet, Y., Fraigneau, Y., and Martin Witkowski, L. (2022). A simple model for arbitrary pollution effects on rotating free-surface flows. *J. Fluid Mech.*, 935:A2.
- Fiedler, B., Flunkert, V., Georgi, M., Hövel, P., and Schöll, E. (2007). Refuting the odd-number limitation of time-delayed feedback control. *Phys. Rev. Lett.*, 98(11):114101.

- Frantz, R. A., Loiseau, J.-C., and Robinet, J.-C. (2023). Krylov methods for large-scale dynamical systems: Application in fluid dynamics. *Appl. Mech. Rev.*, 75(3):030802.
- Garnaud, X., Lesshafft, L., Schmid, P. J., and Huerre, P. (2013). The preferred mode of incompressible jets: linear frequency response analysis. *J. Fluid Mech.*, 716:189–202.
- Gaspard, P. (1990). Measurement of the instability rate of a far-from-equilibrium steady state at an infinite period bifurcation. *J. Phys. Chem.*, 94(1):1–3.
- Gauthier, G. (1998). *Étude expérimentale des instabilités de l'écoulement entre deux disques*. PhD thesis, Université Paris XI, France.
- Gauthier, G., Gondret, P., and Rabaud, M. (1999). Axisymmetric propagating vortices in the flow between a stationary and a rotating disk enclosed by a cylinder. *J. Fluid Mech.*, 386:105–126.
- Gelfgat, A. Y. (2015). Primary oscillatory instability in a rotating disk-cylinder system with aspect (height/radius) ratio varying from 0.1 to 1. *Fluid Dyn. Res.*, 47:035502(14).
- Gelfgat, A. Y. and Tanasawa, I. (1994). Numerical analysis of oscillatory instability of buoyancy convection with the Galerkin spectral method. *Num. Heat Transf. A*, 25:627–648.
- Gesla, A., Duguet, Y., Le Quéré, P., and Martin Witkowski, L. (2023). Subcritical axisymmetric solutions in rotor-stator flow. *arXiv preprint arXiv:2312.09874 (accepted in Phys. Rev. Fluids)*.
- Gesla, A., Duguet, Y., Le Quéré, P., and Martin Witkowski, L. (2024a). On the origin of circular rolls in rotor-stator flow. *arXiv preprint arXiv:2405.02160 (in review in J. Fluid Mech.)*.
- Gesla, A., Duguet, Y., Le Quéré, P., and Martin Witkowski, L. (2024b). Stability analysis of periodic solutions in dynamical systems using Chebyshev polynomial expansion. *arXiv preprint*.
- Grossmann, S. (2000). The onset of shear flow turbulence. *Rev. Mod. Phys.*, 72(2):603.
- Guermond, J. L., Minev, P. D., and Shen, J. (2006). An overview of projection methods for incompressible flows. *Comp. Meth. Appl. Mech. Eng.*, 195:6011–6045.
- Guillot, L., Lazarus, A., Thomas, O., Vergez, C., and Cochelin, B. (2020). A purely frequency based Floquet-hill formulation for the efficient stability computation of periodic solutions of ordinary differential systems. *J. Comput. Phys.*, 416:109477.
- Herbert, T. (1997). Parabolized stability equations. *Ann. Rev. Fluid Mech.*, 29(1):245–283.
- Hirsch, C. (2007). *Numerical Computation of Internal and External Flows: The Fundamentals of Computational Fluid Dynamics*. Elsevier, Burlington, MA.
- Hof, B., De Lozar, A., Kuik, D. J., and Westerweel, J. (2008). Repeller or attractor? selecting the dynamical model for the onset of turbulence in pipe flow. *Phys. Rev. Lett.*, 101(21):214501.
- Holodniok, M., Kubicek, M., and Hlavacek, V. (1977). Computation of the flow between two rotating coaxial disks. *J. Fluid Mech.*, 81(4):689–699.
- Itano, T. and Toh, S. (2001). The dynamics of bursting process in wall turbulence. *J. Phys. Soc. Japan*, 70(3):703–716.
- Jin, B., Symon, S., and Illingworth, S. J. (2021). Energy transfer mechanisms and resolvent analysis in the cylinder wake. *Phys. Rev. Fluids*, 6(2):024702.
- Jovanović, M. R. and Bamieh, B. (2005). Componentwise energy amplification in channel flows. *J. Fluid Mech.*, 534:145–183.
- Kern, J. S., Lupi, V., and Henningson, D. S. (2024). Floquet stability analysis of pulsatile flow in toroidal pipes. *Phys. Rev. Fluids*, 9(4):043906.
- Khapko, T., Duguet, Y., Kreilos, T., Schlatter, P., Eckhardt, B., and Henningson, D. S. (2014). Complexity of localised coherent structures in a boundary-layer flow. *Eur. Phys. J. E*, 37:1–12.

- Khapko, T., Kreilos, T., Schlatter, P., Duguet, Y., Eckhardt, B., and Henningson, D. S. (2013). Localized edge states in the asymptotic suction boundary layer. *J. Fluid Mech.*, 717:R6.
- Khapko, T., Kreilos, T., Schlatter, P., Duguet, Y., Eckhardt, B., and Henningson, D. S. (2016). Edge states as mediators of bypass transition in boundary-layer flows. *J. Fluid Mech.*, 801:R2.
- Kolenkiewicz, R. and Carpenter, L. (1967). Periodic motion around the triangular libration point in the restricted problem of four bodies. *Astron. J.*, 72:180.
- Kuhlmann, H. C. and Romanò, F. (2019). *The Lid-Driven Cavity*, pages 233–309. Springer International Publishing, Cham.
- Kuznetsov, Y. A., Kuznetsov, I. A., and Kuznetsov, Y. (1998). *Elements of Applied Bifurcation Theory*, volume 112 of *Appl. Math. Sci.* Springer, Cham, Switzerland.
- Lai, Y.-C. and Tél, T. (2011). *Transient Chaos: Complex Dynamics on Finite Time Scales*, volume 173 of *Appl. Math. Sci.* Springer Science & Business Media, Cham, Switzerland.
- Lan, Y. and Cvitanović, P. (2004). Variational method for finding periodic orbits in a general flow. *Phys. Rev. E*, 69(1):016217.
- Launder, B., Poncet, S., and Serre, E. (2010). Laminar, transitional, and turbulent flows in rotor-stator cavities. *Ann. Rev. Fluid Mech.*, 42:229–248.
- Lazarus, A. and Thomas, O. (2010). A harmonic-based method for computing the stability of periodic solutions of dynamical systems. *C. R. Mécanique*, 338(9):510–517.
- Le Quéré, P. (1994). Onset of unsteadiness, routes to chaos and simulations of chaotic flows in cavities heated from the side: a review of present status. In *International Heat Transfer Conference Digital Library*. Begel House Inc.
- Lingwood, R. J. (1997). Absolute instability of the Ekman layer and related rotating flows. *J. Fluid Mech.*, 331:405–428.
- Lopez, J. M., Marques, F., Rubio, A. M., and Avila, M. (2009). Crossflow instability of finite Bödewadt flows : Transients and spiral waves. *Phys. Fluids*, 21:114107.
- Lopez, J. M., Welfert, B. D., Wu, K., and Yalim, J. (2017). Transition to complex dynamics in the cubic lid-driven cavity. *Phys. Rev. Fluids*, 2(7):074401.
- Lorenz, E. N. (1963). Deterministic nonperiodic flow. *J. Atmos. Sci.*, 20(2):130–141.
- Manneville, P. (2016). Transition to turbulence in wall-bounded flows: Where do we stand? *Mech. Eng. Rev.*, 3(2):15–00684.
- Mantič-Lugo, V., Arratia, C., and Gallaire, F. (2014). Self-consistent mean flow description of the nonlinear saturation of the vortex shedding in the cylinder wake. *Phys. Rev. Lett.*, 113:084501.
- Mantič-Lugo, V., Arratia, C., and Gallaire, F. (2015). A self-consistent model for the saturation dynamics of the vortex shedding around the mean flow in the unstable cylinder wake. *Phys. Fluids*, 27(7).
- Moin, P. (2010). *Fundamentals of Engineering Numerical Analysis*. Cambridge University Press, New York.
- Moisy, F., Pasutto, T., Gauthier, G., Gondret, P., and Rabaud, M. (2003). Spiral patterns in swirling flows. *Europhys. News*, 34(3):104–107.
- Oteski, L., Duguet, Y., Pastur, L., and Le Quéré, P. (2015). Quasiperiodic routes to chaos in confined two-dimensional differential convection. *Phys. Rev. E*, 92(4):043020.
- Parker, J. P. and Schneider, T. M. (2022). Variational methods for finding periodic orbits in the incompressible Navier–Stokes equations. *J. Fluid Mech.*, 941:A17.

- Peletan, L., Baguet, S., Torkhani, M., and Jacquet-Richardet, G. (2013). A comparison of stability computational methods for periodic solution of nonlinear problems with application to rotordynamics. *Nonlinear Dyn.*, 72:671–682.
- Pier, B. and Schmid, P. J. (2017). Linear and nonlinear dynamics of pulsatile channel flow. *J. Fluid Mech.*, 815:435–480.
- Poncet, S., Serre, E., and Le Gal, P. (2009). Revisiting the two first instabilities of the flow in an annular rotor-stator cavity. *Phys. Fluids*, 21:064106(8).
- Pyragas, K. (1992). Continuous control of chaos by self-controlling feedback. *Phys. Lett. A*, 170(6):421–428.
- Rhie, C. M. and Chow, W.-L. (1983). Numerical study of the turbulent flow past an airfoil with trailing edge separation. *AIAA journal*, 21(11):1525–1532.
- Rigas, G., Sipp, D., and Colonius, T. (2021). Nonlinear input/output analysis: application to boundary layer transition. *J. Fluid Mech.*, 911:A15.
- Sánchez, J., Net, M., García-Archilla, B., and Simó, C. (2004). Newton–Krylov continuation of periodic orbits for Navier–Stokes flows. *J. Comput. Phys.*, 201(1):13–33.
- Savas, O. (1983). Circular waves on a stationary disk in rotating flow. *Phys. Fluids*, 26.
- Schmid, P. J. and Brandt, L. (2014). Analysis of fluid systems: stability, receptivity, sensitivity: lecture notes from the FLOW-NORDITA summer school on advanced instability methods for complex flows, Stockholm, Sweden, 2013. *Appl. Mech. Rev.*, 66(2):024803.
- Schneider, T. M. and Eckhardt, B. (2009). Edge states intermediate between laminar and turbulent dynamics in pipe flow. *Philos. Trans. Royal Soc. A*, 367(1888):577–587.
- Schneider, T. M., Eckhardt, B., and Yorke, J. A. (2007). Turbulence transition and the edge of chaos in pipe flow. *Phys. Rev. Lett.*, 99(3):034502.
- Schouveiler, L., Le Gal, P., and Chauve, M. P. (2001). Instabilities of the flow between a rotating and a stationary disk. *J. Fluid Mech.*, 443:329–350.
- Serre, E., Crespo Del Arco, E., and Bontoux, P. (2001). Annular and spiral patterns in flows between rotating and stationary discs. *J. Fluid Mech.*, 434:65–100.
- Serre, E., Tuliszka-Sznitko, E., and Bontoux, P. (2004). Coupled numerical and theoretical study of the flow transition between a rotating and a stationary disk. *Phys. Fluids*, 16:688–706.
- Seydel, R. (1987). New methods for calculating the stability of periodic solutions. *Comput. Math. Appl.*, 14(7):505–510.
- Seydel, R. (2009). *Practical Bifurcation and Stability Analysis*, volume 5 of *Interdiscip. Appl. Math.* Springer Science & Business Media, Cham.
- Sierra-Ausin, J., Citro, V., Giannetti, F., and Fabre, D. (2022). Efficient computation of time-periodic compressible flows with spectral techniques. *Comp. Meth. Appl. Mech. Eng.*, 393:114736.
- Skufca, J. D., Yorke, J. A., and Eckhardt, B. (2006). Edge of chaos in a parallel shear flow. *Phys. Rev. Lett.*, 96(17):174101.
- Sleimi, E. (2018). Étude de la stabilité d'un écoulement rotor-stator. Stage M1, Sorbonne Université, France. 7 mai – 8 août.
- Stewartson, K. (1953). On the flow between two rotating coaxial disks. *Proc. Camb. Phil. Soc.*, 49:333–341.
- Strogatz, S. H. (2018). *Nonlinear Dynamics and Chaos: With Applications to Physics, Biology, Chemistry, and Engineering*. CRC press, Boca Raton, FL.

- Thomas, L. H. (1949). Elliptic problems in linear difference equations over a network. *Watson Sci. Comput. Lab. Rept., Columbia University, New York*, 1:71.
- Thorpe, S. (1968). On standing internal gravity waves of finite amplitude. *J. Fluid Mech.*, 32(3):489–528.
- Tobias, S., Proctor, M., and Knobloch, E. (1998). Convective and absolute instabilities of fluid flows in finite geometry. *Physica D*, 113(1):43–72.
- Trefethen, L. N. and Embree, M. (2005). *Spectra and Pseudospectra: The Behavior of Nonnormal Matrices and Operators*. Princeton University Press, Princeton, New Jersey.
- Trefethen, L. N., Trefethen, A. E., Reddy, S. C., and Driscoll, T. A. (1993). Hydrodynamic stability without eigenvalues. *Science*, 261(5121):578–584.
- Veronis, G. (1970). The analogy between rotating and stratified fluids. *Ann. Rev. Fluid Mech.*, 2:37–66.
- Viswanath, D. (2003). Symbolic dynamics and periodic orbits of the Lorenz attractor. *Nonlinearity*, 16(3):1035.
- Viswanath, D. (2007). Recurrent motions within plane Couette turbulence. *J. Fluid Mech.*, 580:339–358.
- Waleffe, F. (2003). Homotopy of exact coherent structures in plane shear flows. *Phys. Fluids*, 15(6):1517–1534.
- Wang, J., Gibson, J., and Waleffe, F. (2007). Lower branch coherent states in shear flows: transition and control. *Phys. Rev. Lett.*, 98(20):204501.
- Winters, K. (1987). Hopf bifurcation in the double-glazing problem with conducting boundaries. *J. Heat Transfer*.
- Woiwode, L. and Krack, M. (2023). Are Chebyshev-based stability analysis and Urabe's error bound useful features for harmonic balance? *Mech. Syst. Signal Process.*, 194:110265.
- Wu, J., Hong, L., and Jiang, J. (2022). A robust and efficient stability analysis of periodic solutions based on harmonic balance method and Floquet-Hill formulation. *Mech. Syst. Signal Process.*, 173:109057.
- Xin, S. and Le Quéré, P. (2001). Linear stability analyses of natural convection flows in a differentially heated square cavity with conducting horizontal walls. *Phys. Fluids*, 13(9):2529–2542.
- Zandbergen, P. J. and Dijkstra, D. (1987). Von Kármán swirling flows. *Ann. Rev. Fluid Mech.*, 19(1):465–491.
- Zhou, T., Xu, J., and Chen, C. (2001). Research on the periodic orbit of non-linear dynamic systems using Chebyshev polynomials. *J. Sound Vib.*, 245(2):239–250.
- Zhou, W., Han, J., and Chen, Q. (2013). Finding Chebyshev series periodic solutions of nonlinear vibration systems via optimization method. *J. Vibroeng.*, 15(3):1081–1092.

Sujet: Etude numérique de la dynamique d'un écoulement rotor-stator axisymétrique

Resumé: Les écoulements dans la cavité rotor-stator sont connus pour présenter des structures d'écoulement instables sous la forme de rouleaux circulaires et en spirale. Si l'origine des spirales est bien comprise, celle des rouleaux circulaires ne l'est pas. Dans la présente étude, l'écoulement axisymétrique dans une cavité de rapport d'aspect $R/H = 10$ est revisité numériquement à l'aide de concepts et d'outils récents issus de la théorie de la bifurcation.

Il est confirmé qu'une instabilité linéaire a lieu à un nombre de Reynolds critique fini $Re = Re_c$ et une branche de solutions supercritiques émanant du point critique est identifiée. Diverses autres solutions auto-entretenues sont calculées, parmi lesquelles une branche de dynamique chaotique, un état de bord séparant les bassins d'attraction laminaire et turbulent et une branche sous-critique de solutions exactement périodiques. Il est démontré que toutes ces solutions existent à un Re plus grand que prévu d'après les études expérimentales et ne peuvent donc pas expliquer les rouleaux circulaires observés dans les expériences.

Dans la deuxième partie du travail, nous proposons un scénario quantitatif pour les rouleaux circulaires en réponse du système à un forçage externe. En utilisant la décomposition en valeurs singulières de l'opérateur résolvant, la réponse optimale prend la forme de rouleaux circulaires. Des simulations numériques directes du problème forcé confirment la réponse privilégiée de l'écoulement sous la forme de rouleaux circulaires. Nos résultats suggèrent que les rouleaux circulaires observés expérimentalement sont l'effet combiné du gain de forçage élevé et de la forme en forme de rouleau de la réponse principale de l'opérateur linéarisé.

Dans la dernière partie du travail, nous proposons l'application des polynômes de Chebyshev à la description de la dépendance temporelle de la dynamique périodique. Les caractéristiques de stabilité de l'orbite périodique sont facilement extraites de la linéarisation autour de l'orbite périodique. La méthode est comparée à la méthode d'équilibre harmonique (HBM) avec des exemples de systèmes de Lorenz, Langford et la cavité différemment chauffée. Le principal avantage de la méthode présente est que, contrairement à HBM, elle permet une détermination sans ambiguïté des exposants de Floquet.

Mots clés: transition, sous-critique, rotor-stator

Subject: Numerical investigation of the dynamics of an axisymmetric rotor-stator flow

Abstract: Rotor-stator cavity flows are known to exhibit unsteady flow structures in the form of circular and spiral rolls. While the origin of the spirals is well understood, that of the circular rolls is not. In the present study the axisymmetric flow in an aspect ratio $R/H = 10$ cavity is revisited numerically using recent concepts and tools from bifurcation theory.

It is confirmed that a linear instability takes place at a finite critical Reynolds number $Re = Re_c$ and a branch of supercritical solutions emanating at the critical point is identified. Various other self-sustained solutions are computed, among them a branch of chaotic dynamics, an edge state separating the laminar and turbulent basins of attraction and a subcritical branch of exactly periodic solutions. All these solutions are shown to exist at Re larger than expected from the experimental studies and therefore cannot explain the circular rolls observed in the experiments.

In the second part of the work we suggest a quantitative scenario for the circular rolls as a response of the system to external forcing. Using the singular value decomposition of the resolvent operator the optimal response is shown to take the form of circular rolls. Direct numerical simulations of the forced problem confirm the flow's preferred response in the shape of circular rolls. Our findings suggest that the circular rolls observed experimentally are the combined effect of the high forcing gain and the roll-like form of the leading response of the linearised operator.

In the final part of the work, we propose the application of Chebyshev polynomials to the description of the time dependence of the periodic dynamics. The stability characteristics of the periodic orbit are easily extracted from the linearisation around the periodic orbit. The method is compared with the Harmonic Balance Method (HBM) with examples from Lorenz, Langford and differentially heated cavity systems. The main advantage of the present method is that, unlike HBM, it allows for an unambiguous determination of the Floquet exponents.

Keywords: transition, subcritical, rotor-stator